

THE EVOLUTION OF RED SUPERGIANTS  
IN LOCAL GROUP GALAXIES

Sarah Louise Eileen McDonald

A thesis submitted in partial fulfilment of the requirements of  
Liverpool John Moores University  
for the degree of  
Doctor of Philosophy.  
January 2024

# Declaration

The work presented in this thesis was carried out at the Astrophysics Research Institute, Liverpool John Moores University. It is the original work of the author in its entirety with the exception of the following items:

While registered as a candidate for the degree of Doctor of Philosophy, for which submission is now made, the author has not been registered as a candidate for any other award. This thesis has not been submitted in whole, or in part, for any other degree.

Sarah Louise Eileen McDonald  
Astrophysics Research Institute  
Liverpool John Moores University  
IC2, Liverpool Science Park  
146 Brownlow Hill  
Liverpool  
L3 5RF  
UK

MARCH 2024

# Abstract

The luminosities and mass loss rates of Red supergiants are important factors for understanding the evolution of massive stars. The empirical upper limit to Red Supergiant (RSG) luminosity, known as the Humphreys-Davidson (HD) limit, has been commonly explained as being caused by the stripping of stellar envelopes by metallicity-dependent, line-driven winds. As such, the theoretical expectation is that the HD limit should be higher at lower metallicity, where weaker mass-loss rates mean that higher initial masses are required for an envelope to be stripped. The HD limit is investigated in this thesis using a large sample of M31 RSGs in a galaxy-wide study to measure where the HD limit sits and to observe whether it has a metallicity dependence.

Using a large homogeneous sample provides a great test bed for mass loss rates of RSGs. Recent prescriptions for RSG mass loss have seen a downward revision, showing that quiescent mass-loss during the RSG phase is not effective at removing a significant fraction of the Hydrogen envelope, prior to core-collapse. This places extra emphasis on potential short-lived high  $\dot{M}$  phases, which have been suggested to remove several solar masses of material in short periods of time. We investigate the mass-loss rates of RSGs at high metallicity, with the aim of obtaining an unbiased sample that catches RSGs in all mass loss phases, even the very brief ones, such that we can then ascertain in which phase most of the mass is lost.

The overall aim of this thesis is to address these unresolved problems in massive stellar evolution and help bridge the gap between the RSG phase and supernova explosion. Having a better understanding of RSG luminosity and mass loss rates will enhance the accuracy of predictions from stellar evolution models, strengthening our understanding of massive stellar evolution.

# Contents

<b>Declaration</b>	<b>ii</b>
<b>Abstract</b>	<b>iii</b>
<b>Contents</b>	<b>iv</b>
List of Figures . . . . .	vii
<b>List of Figures</b>	<b>vii</b>
List of Tables . . . . .	ix
<b>List of Tables</b>	<b>ix</b>
<b>Publications</b>	<b>x</b>
<b>Acknowledgements</b>	<b>xi</b>
<b>1 Introduction</b>	<b>1</b>
1.1 Massive star evolution . . . . .	1
1.1.1 Evolution of the core . . . . .	1
1.2 Evolutionary effects of mass loss . . . . .	3
1.3 Observations of red supergiants . . . . .	4
1.3.1 The Humphreys-Davidson limit . . . . .	4
1.3.2 Type IIP progenitors . . . . .	7
1.3.2.1 The red supergiant problem . . . . .	8
1.4 Red supergiant mass loss . . . . .	10
1.4.1 Red supergiant winds . . . . .	10
1.4.2 Measuring $\dot{M}$ . . . . .	11
1.4.3 $\dot{M}$ implemented in stellar models . . . . .	16
1.5 This Thesis . . . . .	19
<b>2 The Humphreys-Davidson limit of Red Supergiants in Local Group Galaxies</b>	<b>21</b>
2.1 Method . . . . .	21
2.1.1 Compiling a sample of M31 red supergiants . . . . .	21
2.1.2 Correcting for foreground extinction . . . . .	25
2.1.3 Determining bolometric luminosity . . . . .	26
2.1.4 Bolometric corrections . . . . .	27
2.2 Results . . . . .	29
2.2.1 The RSG luminosity function . . . . .	29
2.2.1.1 Most luminous M31 RSG candidates and $L_{\max}$ . . . . .	30
2.2.1.2 Stars rejected from this work . . . . .	33

2.2.1.3	Sample completeness . . . . .	34
2.2.1.4	Rejected stars from Massey & Evans (2016) and Gordon et al. (2016) . . . . .	36
2.3	Discussion . . . . .	37
2.3.1	Comparison to previous work . . . . .	37
2.3.1.1	Comparison with Massey & Evans (2016) and Neugent et al. (2020) . . . . .	37
2.3.1.2	Comparison with Gordon et al. (2016) . . . . .	38
2.3.2	Comparison to lower metallicity galaxies . . . . .	39
2.3.2.1	Observational comparisons between the LMC and SMC . . . . .	39
2.3.3	Theoretical predictions of the luminosity distribution . . . . .	42
2.3.3.1	Comparisons to theoretical predictions of $L_{\max}$ . . . . .	44
2.3.4	Possible explanations for a metallicity invariant HD limit . . . . .	46
2.4	Summary . . . . .	50
<b>3</b>	<b>A mass-loss survey of M31 Red Supergiants</b> . . . . .	<b>51</b>
3.1	Method . . . . .	53
3.2	DUSTY: Radiative transfer code . . . . .	53
3.2.1	Model parameters . . . . .	54
3.2.2	Fitting Methodology . . . . .	56
3.2.3	Calculating $\dot{M}$ . . . . .	57
3.3	Results . . . . .	57
3.3.1	Modelling results . . . . .	57
3.3.1.1	$24\mu\text{m}$ offset correction . . . . .	61
3.4	Discussion . . . . .	64
3.4.1	Super-wind analysis: Monte Carlo . . . . .	66
3.4.2	Super-wind analysis: MESA-MIST . . . . .	67
3.4.3	Comparison Wang et al (2021) . . . . .	70
3.5	Summary . . . . .	70
<b>4</b>	<b>Using machine learning techniques to estimate red supergiant mass loss rates and luminosities</b> . . . . .	<b>72</b>
4.1	Method . . . . .	73
4.1.1	Linear regression . . . . .	73
4.1.2	Varying the loss function . . . . .	74
4.1.2.1	Huber loss . . . . .	76
4.1.2.2	Epsilon-insensitive loss . . . . .	77
4.1.3	Random states . . . . .	78
4.2	Results . . . . .	79
4.2.1	Mass loss rates of red supergiants using linear regression . . . . .	79
4.2.2	Mass loss rates from reduced datasets . . . . .	82
4.2.3	Predicting M31 red supergiant luminosity using linear regression . . . . .	83
4.2.4	Luminosity from reduced datasets . . . . .	85
4.3	Deployment and evaluation of the model performance on M33 red supergiant photometry . . . . .	86
4.3.1	M33 RSG luminosity predictions . . . . .	90
4.3.1.1	The Humphreys-Davidson limit for M33 red supergiants . . . . .	90
4.3.2	Comparison to previous M33 RSG luminosities: Massey et al. (2021,2023) . . . . .	93
4.3.3	M33 RSG mass loss predictions . . . . .	93

4.4 Summary and future work . . . . .	94
<b>5 Summary &amp; Conclusions</b>	<b>97</b>
5.1 Future Work . . . . .	100
<b>Bibliography</b>	<b>102</b>

# List of Figures

1.1	A schematic showing where different stars sit in the Hertzsprung-Russell diagram . . . . .	2
1.3	A HR diagram showing the bolometric magnitudes and temperatures of galactic supergiants . . . . .	7
1.4	Evolutionary tracks from (a) Maeder & Meynet (2000), (b) Ekström et al. (2012), (c) Beasor et al. (2021) . . . . .	18
2.1	The right ascension and declination of the 415 RSG candidates used in this study of M31 . . . . .	24
2.2	A colour magnitude diagram of all M31 point sources from (Khan, 2017) . . . . .	25
2.3	A luminosity distribution of the 149 RSG candidates found in the region of M31 surveyed by HST PHAT . . . . .	28
2.4	Spectral energy distributions of the most luminous Red Supergiant candidates . . . . .	29
2.5	Bolometric corrections for M31 Red supergiants . . . . .	30
2.6	The Red Supergiant luminosity distribution for M31 . . . . .	31
2.7	Comparison of bolometric luminosities found in other studies . . . . .	40
2.8	Cumulative luminosity distribution of all the Red Supergiants with an observational luminosity $\log(L/L_{\odot}) > 5$ in M31 . . . . .	41
2.9	The expected $L_{\max}$ for a range of sample sizes as predicted by the Geneva rotating models for both solar ( $Z=0.014$ ) and SMC-like ( $Z=0.002$ ) metallicities . . . . .	46
2.10	Predictions of the luminosity function of cool supergiants from BPASS binary population synthesis for the metallicity range $Z=0.004$ to $Z=0.020$ . . . . .	49
3.1	A spectral energy distribution showing the observed photometry fitted to the best fit model spectrum . . . . .	58
3.2	SED and contour for best fit model on a $T_{inner} - \tau$ plane with the upper and lower $\dot{M}$ contours overplotted . . . . .	59
3.3	Plot showing mass-loss rate as a function of bolometric luminosity for the sample of M31 RSGs . . . . .	60
3.4	RGB images of RSGs in the sample . . . . .	62
3.5	A colour - mass-loss plot for the RSGs used in this study . . . . .	63
3.6	Same as Figure 3.3 except any objects with $\dot{M} > 10^{-5}M_{\odot}\text{yr}^{-1}$ with offset sources have had their $\dot{M}$ re-calculated using an upper $24\mu\text{m}$ limit. . . . .	65
3.7	A cumulative distribution of the Monte Carlo results showing probability as a function of maximum time spent in a super-wind phase. . . . .	66
3.8	Mass-loss rate vs luminosity for the observed M31 RSG sample, with the MIST model predictions overplotted . . . . .	69
4.1	A distribution of the rms errors for both $\log \dot{M}$ and $\log L$ . . . . .	79

4.2	A linear regression plot where the model was trained on all 10 input features	80
4.3	The coefficients for each of the independent variables used in the linear regression model	81
4.4	Same as Figure 4.2 but this time with the model trained on reduced features	84
4.5	A linear regression plot for luminosity trained on all 10 input features	85
4.6	Same as Figure 4.3 but with the coefficient showing the weighting when the target variable is $L_{\text{bol}}$	86
4.7	Same as Figure 4.5 but this time with the model trained on reduced features.	87
4.8	Comparison of bolometric luminosities of M33 RSGs from the linear regression model and those from Massey et al. (2023)	90
4.9	Luminosity distribution of the 171 M33 RSGs	91
4.10	RGB images of the highest mass loss rate M33 RSGs in the sample	92
4.11	An updated cumulative distribution of the Monte Carlo results showing probability as a function of maximum time spent in a super-wind phase using both M33 and M31 RSGs.	94
4.12	The model predicted $\dot{M}$ vs $L_{\text{bol}}$ for M33 RSGs	95

# List of Tables

2.1	The image quality details of the Spitzer Space Telescope. . . . .	22
2.2	The <i>Spitzer</i> colour and magnitude cuts that were applied to locate our target stars . . . . .	26
2.3	The name, position and bolometric luminosity of the RSG candidates with $\log(L/L_{\odot}) > 5.4$ found in this study . . . . .	34
3.1	Results for the 10 highest M RSGs in M31 . . . . .	58
3.2	Revised 10 highest M RSGs in M31 after an upper $24\mu\text{m}$ limit has been applied . . . . .	65
4.1	The rms errors for both the training and test set when varying the number of features used . . . . .	75
4.2	The results of varying the loss function of the linear regression model on the chosen evaluation metrics . . . . .	88

# Publications

In the course of completing the work presented in Chapters 2 and 3, the following papers are published in a refereed journal or are in preparation:

- *Red Supergiants in M31: The Humphreys-Davidson limit at high metallicity*  
**McDonald, S.L.E.**, Davies B., Beasor E. R., 2022, MNRAS, 510, 3132.
- *A mass loss survey of M31 red supergiants*  
**McDonald, S.L.E.**, Davies B., Beasor E. R., 2023, in prep.

# Acknowledgements

Firstly, huge thanks to my parents Alyson and John and my siblings Adam, Nathan and Marisa. Thanks for all your support, encouragement and guidance over the years, I could not have done this without you all. To my nephew and nieces, Aston, Aalayah and Thea and a special thanks to Pauline, for being the greatest aunt anyone could ask for. I miss you immensely. I would also like to thank the Sedgwicks' for their constant support these past few years.

Next, I would like to thank my PhD supervisor, Ben Davies. Thanks for the inspiring undergraduate module 'Stellar Physics', where I realised how much I enjoyed learning about massive stars. This definitely sparked my curiosity for research and urged me to pursue a PhD. Thanks for your expertise, support, patience and most importantly your 'human-ness' these last few years.

I would like to thank my friends who have been a great support system throughout. To Laura and Chloe, for your friendship, unwavering support and most importantly, for always having an Aperol Spritz waiting for me when I come home. Thanks for everything! To Katy and Sophie for all your years of friendship and for always being there. And to the rest of the 'Birmingham girls', Sarah, Chelsea, Taya and Amy, thank you. Also to Vicki and Juliette, my undergrad housemates and now lifelong friends. Thanks for all your support.

I would like to thank my school physics teacher Mr Robertson, who played a big role in helping me start my journey into Astrophysics. Thanks for being so inspiring and enthusiastic about science, and planting the seed by asking me the all important question once after a class: 'Have you ever considered studying Astrophysics at university?'.

I feel enormously grateful to have been a part of such a friendly and inclusive department here at the ARI, so I would like to thank everyone who has helped me during my time here. In particular, I would like to thank Phil James. I am extremely honoured to have been a PhD student during your time as Head of Department, enjoy your retirement, you deserve it! To the NSO, for continually inspiring the next generation, you are amazing! Thank you to Ricardo Schiavon, Marie Martig and Matt Darnley, as well as Anna Hodgkinson, Danielle Coogan and Dan Harman for continually keeping the ARI running smoothly.

To the ARI PhD students, old and new. Jon Davies, Joaquin Garcia, Meghan Hughes, Joe Fernandez, Alex Hill and Alberto Acuto, thank you for making me feel so welcome when I was just a little undergrad trying to do a bit of Astro research over summer in 2018. You all made me feel like there was no other place but the ARI to pursue a PhD. To Conor Ransome, Allister Cockram and Danny Horta thanks for all the bevs and the good memories. In particular, Conor, thanks for keeping pub Fridays alive, and pub Mondays, pub Tuesdays and pub anytime anyone has had a rubbish day in the office and just needed a pint and a rant. You're a legend.

To Bethan, Lib and Emily, I would not have got through undergrad without you. A special thanks to Bethan for navigating through both undergrad and PhD life with me. Thanks for your humour, the memes and the many many Simpsons references. Big thanks to the rest of my year group, Gemma, Andrew, Shobhit, Kyle, Adrian, and Stephen, I am grateful to have shared this journey with you all. To the rest of office 3.18, thanks for always being up for a coffee break and a chat. Special thanks to Gemma and Emma and for being my PhD siblings. Thanks for everything!

To Ziggy, who has sat by my side during every zoom meeting, whilst every code has ran and for each and every draft of my papers and thesis. Thanks for always stamping your paws and dropping your ball at my feet to ask for a walk when I've been staring at my laptop for too long. Thank god one of us understands work-life balance!! And finally, I would like to thank Tom Sedgwick. Thanks for your unwavering love and support, for always believing in me and for continually inspiring me everyday, I love you loads. Most importantly, thanks for letting me excitedly ramble on about massive stars daily for the last 5 years, you deserve a medal.

---

The funding for this PhD was provided by an STFC doctoral studentship, jointly supported by the Faculty of Engineering and Technology at LJMU.

This thesis project has made use of data from the following resources:

- The SPITZER SPACE TELESCOPE , a NASA infrared space telescope and the final element of the NASA Great Observatories program. It carries a near-infrared camera (IRAC), mid-infrared spectrograph (IRS) and a mid- to far-infrared photometer (MIPS). The M31 Spitzer data used in the present work is from [Khan \(2017\)](#).
- The TWO MICRON ALL SKY SURVEY, which is a joint project of the University of Massachusetts and the Infrared Processing and Analysis Center at the California Institute of Technology, funded by the National Aeronautics and Space Administration and the National Science Foundation ([Cutri et al., 2003](#)).
- GAIA EDR3 gives full astrometric data, broad-band photometry, radial velocities, variable star classifications for  $\sim 1$  billion sources, with as well as the VizieR catalogue access tool and the SIMBAD/Aladin Sky Atlas operated at CDS, Strasbourg, France ([Ochsenbein et al., 2000](#); [Wenger et al., 2000](#); [Boch & Fernique, 2014a,b](#)). significantly improved parallaxes and proper motions, and mean photometry compared to DR2 [Gaia Collaboration \(2020\)](#).
- The LOCAL GROUP GALAXY SURVEY provides UBRVI photometry obtained from mosaic images M31 using the Kitt Peak National Observatory 4m telescope in [Massey et al. \(2006\)](#).
- The GENEVA models from [Ekström et al. \(2012\)](#) are an extensive database of stellar evolution models for masses between 0.8 and 120 solar masses and metallicities from  $Z=0.001$  to 0.1. The database includes stellar tracks and the corresponding isochrones.
- The DUSTY code was developed at the University of Kentucky by ([Ivezic et al., 1999](#)). It solves the radiation transport equation coupled self-consistently with the equation of motion for the outflow of gas and dust grains in the circumstellar environments of cool stars.
- MODULES FOR EXPERIMENTS IN STELLAR ASTROPHYSICS (MESA) from [Paxton et al. \(2011a\)](#) is an open-source 1D stellar evolution code which combines many of the numerical and physics modules for simulations of a wide range of

stellar evolution scenarios ranging from very-low mass to massive stars, including advanced evolutionary phases.

- SIMBAD is an astronomical database of objects beyond the Solar System, by the Centre de données astronomiques de Strasbourg (CDS), France. [Wenger et al. \(2000\)](#)
- VIZIER provides the most complete library of published astronomical catalogues and tables with verified and enriched data. [Ochsenbein et al. \(2000\)](#)
- ALADIN is an interactive software sky atlas allowing the user to visualise digitised astronomical images, superimpose entries from astronomical catalogues or databases, and interactively access related data and information from the SIMBAD database, the VIZIER service and other archives for all known sources in the field. [Boch & Fernique \(2014a,b\)](#)

All plots presented in this thesis were produced by myself unless stated, aside from Figure 2.10 which was produced by Ben Davies using IDL. Plots made by myself were all done using Python, aside from Figures 3.2, 3.4 and 4.10, which were made using IDL.

Python packages most notably utilised for this work include `numpy`, `matplotlib`, `sci-kit learn`, `scipy`, and `astropy`.

*"I'm a big name in deep space. Ask your mates."*

Alex Turner, 2018

*This thesis is dedicated to Pauline Caines (1959-2022) and Paula Brodnicki (1949-2023). Rest in peace x*

# Chapter 1

## Introduction

Red Supergiants (RSGs) are an evolved type of star with masses  $> 8M_{\odot}$  (Maeder & Meynet, 2003). They are assigned the spectral class K or M based on their low effective temperatures which range from  $\sim 3500 - 4500\text{K}$  (Davies et al., 2013). For massive stars with initial masses between  $8-25M_{\odot}$ , the RSG stage is the final stage phase before ending their lives exploding as a core collapse supernova (SN), typically a Type IIP (Smartt, 2009). These powerful and luminous explosions from cool, evolved stars are the main source of chemical enrichment of the interstellar medium (ISM) (Rau et al., 2019). Therefore, to fully understand the evolution of galaxies and the wider universe, we need to cultivate a comprehensive and thorough understanding of massive stars and how they evolve. The aim of this thesis is to further our understanding of the latter stages of the lives of cool massive stars before prior to their deaths, focusing particularly on what luminosity and mass-loss distributions of large samples of RSGs can uncover about their evolution.

### 1.1 Massive star evolution

The single most important parameters dictating the evolution of massive stars is mass, which determines the lifetime of the star and its path across the Hertzsprung-Russell (HR) diagram. The location of the star in luminosity-temperature space bands objects together into clear cut groups, which shows the phases passed through during the life cycle of the star. Figure 1.1 shows a schematic of a HR diagram, which shows that RSGs reside in the cool and luminous region of the diagram.

#### 1.1.1 Evolution of the core

Mass is the main driver of stellar evolution, and so depending on its initial mass, the star undergoes specific stages of evolution governed by its internal structure and its

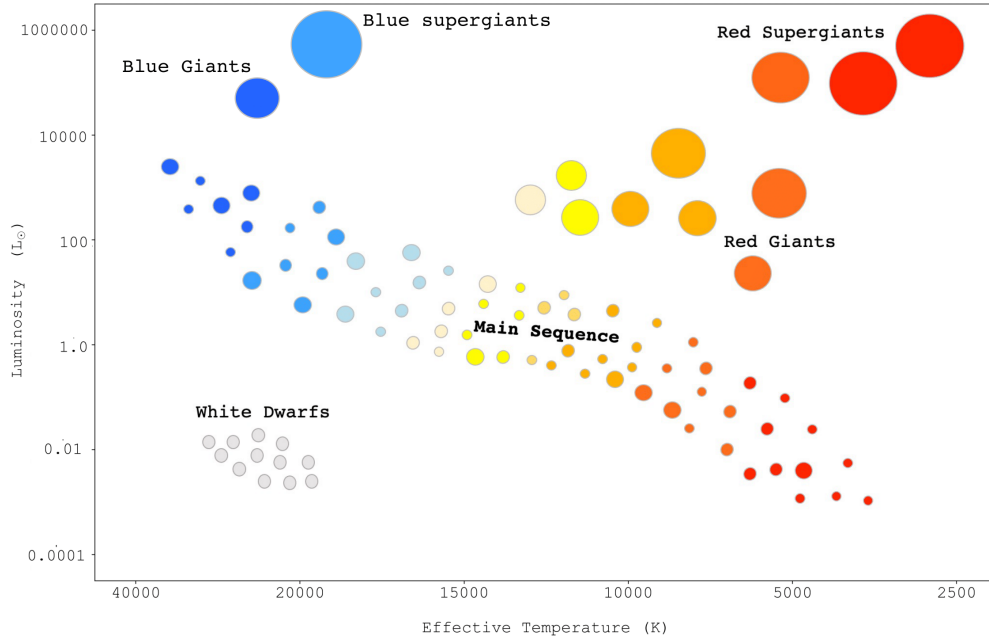


FIGURE 1.1: A schematic showing where different stars sit in the Hertzsprung-Russell diagram (not to scale).

mechanism of producing energy. Through the use of combination of observations and theoretical models, we can study how a star’s luminosity changes over time to learn about its internal processes.

Prior to the cool supergiant phase, typical RSG progenitors with mass in the range of  $8\text{-}20M_{\odot}$  spend roughly 10-60 Myrs as OB stars on the main sequence. These stars have high temperatures, O stars:  $\geq 30000K$ , B stars  $\sim 10000 - 30000K$ , and luminosities in range of  $10^{4.39-5.52}L_{\odot}$  (Davies & Beasor, 2020).

They emit vast amounts of ultra-violet (UV) radiation during their lifetimes which rapidly ionises the surrounding interstellar gas forming an HII region (Reed, 2003). On the main sequence, the core is convective, fusing hydrogen generating both helium and energy, primarily via the carbon-nitrogen-oxygen (CNO) cycle. A result of the core being convective is that when hydrogen begins to run out, it runs out everywhere in the core. When this happens, thermal support decreases and the core contracts, but does not become degenerate. Empirical observations supported by the results of numerical simulations have shown us that massive stars expand after the main sequence due to the contraction of the core heating up the hydrogen-burning shell and generating more energy than the envelope can transport in the timescale of a typical core contraction

(Farrell et al., 2022). The helium and CNO abundances in the hydrogen shell, the core mass ratio and opacity due to hydrogen and metals in the outer envelope govern whether the star ignites helium burning as a RSG or BSG. These properties all affect the rate the envelope expands per each core contraction. Also, changes the hydrostatic structure or the energy transport or any process which results in an increase in the luminosity profile produced by nuclear reactions or a decrease in the actual internal luminosity profile will favour evolution to a larger radius, and vice versa (Farrell et al., 2020, 2022). The expansion of the envelope subsequently leads to a decrease in effective temperature.

In the RSG phase, helium burning has ignited. The material in the radiative envelope in a shell surrounding this now helium-burning core now also ignites. Here the effective temperature of the star is  $\sim 3500 - 4500$  K and radius is  $100 - 1000R_{\odot}$ . The theoretical upper limit of the radius of a red supergiant at around  $1500R_{\odot}$ , known as the Hayashi limit, above which the star would be too unstable to survive (Hayashi & Hoshi, 1961). Depending on mass, eventually within  $\sim 1$  million years, helium in the core also becomes depleted, which results in a convective carbon-burning core now encompassed by both helium and hydrogen shells in the radiative zone. The core of the star will ultimately become hot and dense enough to fuse successively heavier elements in short lived phases until the core has fused to become inert iron. At this point the reaction becomes endothermic, so a vast amount of energy and force is required to fuse the iron atoms. The core collapses when the mass of the iron core reaches the Chandrasekhar mass ( $1.4M_{\odot}$ ), when gravity overcomes degeneracy pressure. This produces a core collapse type II supernova.

## 1.2 Evolutionary effects of mass loss

The amount of mass lost from a star has a profound effect on its evolution. In the extreme case, significant mass loss results in a trajectory back towards the blue hot side of the HR diagram. Mass loss from massive stars can arise from stellar winds, outbursts (e.g. LBV-type eruptions) or binary mass transfer effects. In the hot star regime on the MS, O and B stars lose significant mass through winds which are driven by radiation pressure due to metal absorption lines in the UV (Castor et al., 1975). However, the mechanism for RSG winds remains poorly understood, although there are a number of theories as to what could be driving winds in cool supergiants which are described in detail in Section 1.4.1. For the evolution of RSGs, the combination of initial mass of the star and mass loss rate can have significant effect on the late stage evolution of the star and the resulting supernova. Figure 1.2 shows the evolutionary tracks of different

initial mass RSGs. This idea that a massive star peels off its H-rich outer envelope through stellar winds on the main-sequence is known as the ‘Conti Scenario’ (Conti, 1976) which historically, the evolution of massive stars has been thought to follow. This is outlined below:

- (i) Stars with initial masses in the range of  $8 - 15M_{\odot}$ , stellar winds which are not strong enough to remove the entire hydrogen envelope on the main sequence (Maeder, 1981; Maeder & Meynet, 2003), so it evolves to the RSG phase where it spends the duration of its life before dying as a core collapse supernova (Maeder, 1981; Maeder & Meynet, 2003).
- (ii) Intermediate initial mass stars ( $\sim 15M_{\odot} - 30M_{\odot}$ ) can lose a considerable fraction of their envelope, causing the star to undergo only a brief RSG phase before evolving back towards hotter temperatures. Here it evolves to either a blue supergiant (BSG) or Wolf Rayet (WR) star (Stothers & Chin, 1979). These are late-stage evolved stars with strong, broad emission lines due to their powerful winds. They have experienced such significant mass loss that it leaves their helium cores exposed. It is thought that these stars eventually die as Type Ib/c supernovae (Morozova et al., 2015; Fremling et al., 2016).
- (iii) High initial mass stars ( $\gtrsim 30M_{\odot}$ ), the entire envelope can be lost by the time hydrogen in the core is exhausted. If the envelope is depleted, it can’t expand which prevents evolution to the cool red side of the Hertzsprung-Russell (HR) diagram for the most massive stars. These stars instead either evolve directly from the MS to a WR star, or experience a high mass loss blue supergiant/Luminous Blue Variable phase due to their proximity to Eddington limit, whereby they completely bypass the RSG phase (Stothers & Chin, 1968, 1978). This ultimately means that the highest mass stars on the MS that never evolve to cool temperatures creates a maximum possible luminosity for RSGs. This is discussed in further in Section 1.3.1.

## 1.3 Observations of red supergiants

### 1.3.1 The Humphreys-Davidson limit

It is well established that there is an empirical upper limit to Red Supergiant (RSG) luminosity (Stothers, 1969; Sandage & Tammann, 1974a), often referred to as the

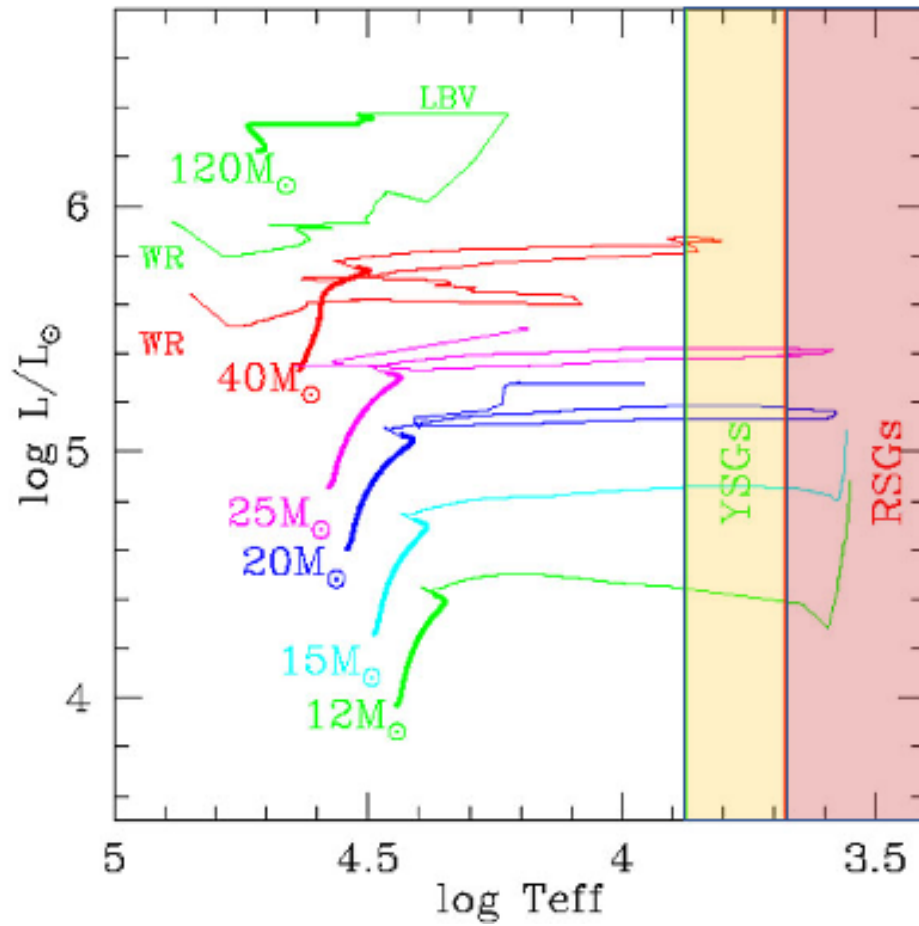


FIGURE 1.2: A HR diagram showing the Geneva evolutionary tracks for solar metallicity ( $z = 0.014$ ) taken from from [Massey \(2013\)](#). It shows the difference in evolution for varying initial masses, highlighting that the highest mass stars bypass the RSG phase completely.

‘Humphreys-Davidson (HD) limit’ (Humphreys & Davidson, 1979). The HD limit has often been explained as being a manifestation of mass loss during the lifetime of the star, caused by line-driven stellar winds or episodic eruptions of mass-loss as seen in luminous blue variables (LBVs) (e.g. Humphreys & Davidson, 1979; Chiosi & Maeder, 1986). The fraction of mass lost from the stellar envelope is dependent on the initial mass of the star. Under this explanation, the HD limit therefore represents the luminosity which corresponds to the most massive star that may still experience a RSG phase.

The first measurement of the HD limit in the literature is  $\log(L/L_{\odot}) = 5.8 \pm 0.1$  inferred by Humphreys & Davidson (1979). This was achieved using a sample of optically selected cool supergiants in the Milky Way and the Large Magellanic Cloud (LMC). This was later revised to  $\log(L/L_{\odot}) = 5.66$  in Humphreys (1983). Figure 1.3 shows where the approximate upper luminosity boundary lies for LMC supergiants, taken from Humphreys & Davidson (1979). Davies, Crowther & Beasor (2018, hereafter, DCB18) revisited the HD limit in the Magellanic Clouds, with more complete samples and higher precision multi-wavelength photometry, finding an upper limit of  $\log(L/L_{\odot}) = 5.5$  for both the Small Magellanic Cloud (SMC) and the LMC. This is important because if line driven winds stripping the envelope of the star and inhibiting red-ward evolution, then we would expect the HD limit to be metallicity dependent. This can be attributed to the mechanism behind hot star winds on the MS, discussed previously in 1.2. Since they are driven by radiation pressure due to metal absorption lines in the UV, this means wind strength is sensitive to metallicity and we therefore would expect a dependence of wind strength on metallicity resulting in a metallicity dependence of the HD limit. Therefore, the HD limit of the LMC and SMC being the same goes against evolutionary theory.

To study the HD limit at higher metallicity, the most obvious environment would be the Milky Way. However, there are a number of obstacles in studying the RSG population of the Milky Way such as high foreground extinction and uncertain distances, therefore only an incomplete luminosity distribution of RSGs in the Galaxy is achievable. Although, Davies & Beasor (2020) argue that even with an effective sample size of over 100, there were still no RSGs with luminosity greater than  $\log(L/L_{\odot}) = 5.5$  in the Galaxy, and conclude the HD limit at solar metallicity is comparable to that of the SMC and LMC. However, studies of stellar populations in the plane of the Milky Way will always be subject to criticisms of completeness. Therefore, to investigate the HD limit at high metallicity, a similar galaxy-wide study is required, but in a higher metallicity galaxy. We therefore study the RSG population of M31 to investigate the

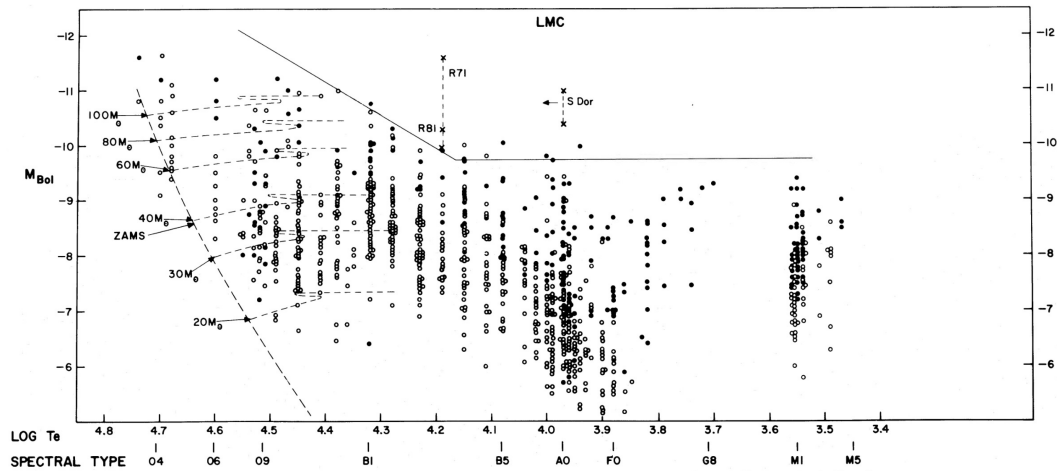


FIGURE 1.3: A HR diagram showing the bolometric magnitudes and temperatures of galactic supergiants with spectral types O through to M, from [Humphreys & Davidson \(1979\)](#). The solid line shows the estimated upper limit of supergiant luminosity, which is shown to be  $M_{\text{bol}} = -9.8$  mag or  $\log(L/L_{\odot}) = 5.8$ .

HD limit and this is discussed in depth in Section 2.

### 1.3.2 Type IIP progenitors

Evolutionary models have predicted that single stars with masses between  $8 - 25M_{\odot}$  will end their lives in the RSG phase ([Maeder & Meynet, 2003](#)). These stars will explode as a type II SN, a class of supernovae distinguishable from type I SNe due to the presence of hydrogen in their spectra. RSGs are usually classified further as ‘IIP’ due to the plateau in its subsequent light curve. This class of SNe are also speculated to leave behind a neutron star (e.g. [Heger et al., 2003](#)). Stars with initial masses greater than  $\sim 30M_{\odot}$  are expected to evolve back to the blue and die as type Ibc or ‘hydrogen-poor’ SNe. These more massive stars have the potential to become black holes (BH), with suggestions in the literature that these high mass RSGs implode quietly and evolve to a BH without a SN explosion ([Adams et al., 2017](#); [Sukhbold et al., 2018](#)). Observational studies indicate the threshold in initial mass and luminosity space for direct-to-BH RSGs  $\gtrsim 20M_{\odot}$  and  $\gtrsim \log(L/L_{\odot}) = 5.2$  (see, [Sukhbold & Adams, 2020](#)).

SN progenitors are usually classified using comparisons with pre-explosion images of the SN explosion site. In the prominent case of the SN1987A<sup>1</sup>, a core collapse supernova

<sup>1</sup>Another reason SN1987A remains such an important event was the coinciding detection of a neutrinos which is considered to be confirmation that Type II supernovae are triggered by the collapse of stellar cores ([Podsiadlowski, 1992](#)).

which exploded in the Large Magellanic Cloud. The progenitor was initially expected to be a RSG as per the theoretical expectation at that time, massive stars exploded as either a RSG or WR star. However, spatial and spectroscopic information as well as comparison with pre-explosion imaging concluded the progenitor of this SN was actually a hotter, more compact blue supergiant (Gilmozzi et al., 1987; Walborn et al., 1987). This changed the view of the blue supergiant stage from just being a ‘middle’ phase passed through during its evolution, but to another potential channel to the stars death. Based on calculations in Saio et al. (1988), the initial mass of the progenitor was estimated to be  $20M_{\odot}$  and may have experienced a blue-red-blue evolution, before dying as a type II SN. It is during its red supergiant phase where it is thought to have emitted the dust ring observed at the site of the SN (see, Podsiadlowski et al., 1990; Podsiadlowski, 1992).

### 1.3.2.1 The red supergiant problem

As discussed previously in Section 1.3.2, prior to SN, if an explosion site has been imaged it is possible to directly confirm the SN progenitor. From this, estimates of their masses as well as final luminosities can also be determined. A  $\sim 10$  year, volume limited (28Mpc) study by Smartt (2009), used this method to further investigate what type of progenitor produces which class of SNe. They compared 20 Type II SN progenitors (18 type IIP and 2 with unknown subcategories) with stellar evolution models to determine the minimum and maximum initial mass limits for the progenitors of these SNe. They found the minimum mass required for stars to explode as Type IIP SNe was  $8.5^{+1.0}_{-1.5}M_{\odot}$  consistent the observed upper mass limit for the formation of white dwarfs (Williams et al., 2009). However, the maximum mass limit was found to be  $16^{+1.5}_{-1.5}M_{\odot}$  resulting seemingly in a much lower upper mass cut off for RSG progenitors. This was later revised to  $17M_{\odot}$  is Smartt (2015). Therefore, this absence of higher mass red supergiant SN progenitors leaves a gap in our understanding of the fates of stars with masses upwards of  $\sim 18 - 30M_{\odot}$ . RSGs of higher masses have been observed but none have been successfully established as progenitors in pre-supernova images (Walmswell & Eldridge, 2012). This is known as the “Red Supergiant Problem” in the literature, first coined by Smartt (2009). When considering this problem from a luminosity perspective, since a mass discrepancy also implies a luminosity discrepancy, the expected upper mass limit can then be inferred from the HD limit and converted to initial mass (see, Smartt et al., 2003; Maund & Smartt, 2005, etc). Since the HD limit for the Magellanic clouds and the Milky Way is found to be  $\log(L/L_{\odot})=5.5$ , we should expect to find SN progenitors with pre-explosion luminosities comparable to this. However, from studies such as Smartt (2009), Smartt (2015) and Davies & Beasor (2018) the most luminous object

found so far is SN2009hd with  $\log(L/L_{\odot}) = 5.24 \pm 0.08$ . This is in tension with the HD limit.

Efforts to reconcile the discrepancies of the RSG problem include adaptations to our understanding of stellar physics or omitted systematic effects. For example, [Kochanek et al. \(2008\)](#) suggest that some stars within the  $8 - 25M_{\odot}$  range have the capabilities of collapsing directly to black holes without a preceding supernova event (e.g. [Heger et al., 2003](#); [Kochanek et al., 2008](#)), or that perhaps the mass threshold at which black-holes (BHs) form is lower ([Smartt, 2009](#)). [Fryer \(1999\)](#) discuss the sensitivity of core-collapse simulations, and demonstrates that by reducing neutrino energy by 20% reduces the mean neutrino energy by a factor of 2 which then reduces the minimum mass for black hole production to  $\sim 15M_{\odot}$ . Further, simply enhancing the rate of mass loss has been suggested as way to resolve the tension between the RSG problem and evolutionary model predictions ([Georgy et al., 2013a](#)). However, there is little observational justification for doing so, with more recent mass loss rate calculations of both hot and cool supergiants being revised down (e.g. [Beasor et al., 2020](#); [Björklund et al., 2021](#)).

In [Walmswell & Eldridge \(2012\)](#), they show that by omitting the effects of further extinction resulting from the dust produced from RSG winds, giving rise to an underestimated luminosity for the most massive late-stage RSGs. When taking into account this additional extinction, new estimates of the initial masses of previously observed Type IIP progenitors find the maximum likelihood mass progenitor is  $21_{-1}^{+2}M_{\odot}$ . This is an upward revision on the [Smartt \(2009\)](#) result, and much better agreement with the predicted initial mass estimates from single star evolution models, however in [Kochanek et al. \(2014\)](#) they point out that the dust also scatters light into the line-of-sight, so the results of [Walmswell & Eldridge \(2012\)](#) are over-estimated. In [Davies & Beasor \(2018\)](#), they take a closer look at another cause of systematic error in estimating initial masses of type IIP progenitors, the underestimate of bolometric correction (BC) for RSGs when approaching the end of its life. When converting pre-explosion photometry into an initial mass, the BC used to convert a single-band flux into a bolometric luminosity doesn't take into account the increase in BC due to the RSGs shift to later spectral types when close to SN, plus the difficulties in converting pre-explosion brightness to bolometric luminosity ( $L_{final}$ ) as well converting  $L_{final}$  to  $M_{initial}$ . This once again results in a systematic underestimate of a star's luminosity, and therefore its initial mass. Once these systematics are accounted for they argued that  $M_{max}$  increases to  $21M_{\odot}$  with a  $1\sigma$  upper error bar extending to  $30M_{\odot}$ , concluding that evidence for the missing higher mass stars had only a minor statistical significance, not significant enough to suggest

there are ‘missing’ high mass type IIP progenitors. There is now almost unification of observation and theory with the [Davies & Beasor \(2020\)](#) and [Sukhbold et al. \(2018\)](#) finding that the mass threshold for type IIP SNe is around  $20M_{\odot}$  or  $10^{5.3}L_{\odot}$ , however the discrepancy with the HD limit is still remains unresolved.

## 1.4 Red supergiant mass loss

Previously in Section 1.2, the effects of mass loss on the evolution of massive stars across the HR diagram is discussed. Following on, in the present section, the fundamental properties of this mass loss is discussed.

A combination of various observational techniques provide evidence that massive stars experience winds. One of the most prominent spectroscopic features of the presence of stellar wind is a ‘P-Cygni profile’ in the star’s spectral lines which of both absorption and emission in the profile of the same spectral line indicative of fast moving material moving away from the star. The emission line emerges from a dense stellar wind near to the star, while the blue-shifted absorption feature is created where the radiation passes through circumstellar material rapidly expanding in the line of sight of the observer (ref). Characteristics such as wind velocity and density can be also be inferred from the spectral features of massive stars ([Conti & McCray, 1980](#)). For RSGs in particular, they are known to be strong sources of infrared radiation, due to the dust particles in their winds absorbing and re-emitting the star’s light at longer wavelengths. Observations at these wavelengths show that circumstellar dust shells are typically present around all M-type giants and supergiants ([Gehrz & Woolf, 1971](#)) and the presence of this infrared emission is a strong indication of the existence of a wind. The warm dusty circumstellar medium (CSM) surrounding RSGs can act as a diagnostic tool to understand the mass loss history in this evolutionary stage.

### 1.4.1 Red supergiant winds

Unlike stellar winds in the hot star regime, the driving mechanism for cool star winds remains uncertain and so mass-loss rates cannot be calculated from first principles. Instead, observations are needed to contribute to stellar evolution models to aid in understanding the process behind it.

In the literature, it has been widely assumed that the mechanism of instigating mass-loss in M supergiants is radial pulsations (e.g. [Gehrz & Woolf, 1971](#); [Bowers et al., 1983](#)).

Similar to asymptotic giant branch (AGB) stars, RSG winds are thought to be driven by dust from stellar pulsations which send gas from the surface up to the extended atmosphere where the dust grains condense, with stellar pulsations lifting gas from the stellar surface up to the outer atmosphere where the dust grains then condense (see, [Hoefner & Dorfi, 1997](#); [Höfner & Olofsson, 2018](#)). Radiation pressure on the dust grains from the star triggers outward movement, dragging the surrounding gas away with it, thus driving both gas and dust comprised winds ([Höfner, 2008](#)). The process for the dust grains to condense is also dependent on density which means both an adequate amount of material is necessary at a sufficient distance from the central star for dust formation to occur.

However, the pulsations in RSGs are thought to be much lower in amplitude compared to AGB stars (e.g. [Wood et al., 1983](#)), which may not be efficient to propel enough material far enough to the cooler regions of the extended atmosphere ([Verhoelst et al., 2009](#)). Stellar models have not successfully managed to replicate this process to obtain the RSG mass loss rates we observe ([Arroyo-Torres et al., 2015](#)). Other mechanisms that might give rise to mass loss in the RSGs phase are convection and rotation (e.g. [Langer & Heger, 1999](#)) and any other processes which elevate materials into the outer atmosphere. Although, these largely have no observational motivated basis for them to singularly be the mechanism for RSG mass loss. More recently, in the work by [Kee et al. \(2021\)](#), they review how atmospheric turbulence may play a role in initiating and determining the mass-loss rates of RSGs following on from work by [Josselin & Plez \(2007\)](#). They derive a theoretical, dust-free model for the mass loss rates of RSGs and conclude that pressure as a result of turbulent velocities in RSGs can alone be sufficient to explain the mass-loss rates of RSGs, even in the absence of any dust opacity from circumstellar dust. Also, in [Rau et al. \(2018\)](#), it is also suggested that magnetohydrodynamic Alfvén waves in the chromospheres of AGBs have the ability to drag material from the star which could similarly be occurring in RSGs.

### 1.4.2 Measuring $\dot{M}$

Despite the inability to obtain a mass loss prescription from first principles at the current time, one can be empirically derived and used to estimate mass loss rates of cool supergiants. Early examples of this include studies of the M5 supergiant  $\alpha$  Herculis, the primary star in a visual binary system surrounded by a common envelope. A paper by [Deutsch \(1956\)](#) show that violet displaced absorption cores i.e. broad absorption lines that are shifted towards the shorter violet wavelengths, relative to the rest of the

absorption lines in the spectrum, are commonly seen in cool red giant and supergiants. These can be used to infer a wind speed as they are interpreted as arising from mass outflows at velocities of  $\sim 10 \text{ km s}^{-1}$  (see, Reimers, 1975; Wallerstein, 1981). From this,  $\dot{M} \sim 3 \times 10^{-8} M_{\odot} \text{ yr}^{-1}$  was inferred by Deutsch (1956). Later work by Gehrz & Woolf (1971) found that the dusty winds of this star produces extra emission in the mid-IR to the detriment of flux from the visible region. With a few assumptions, e.g. adopting a density profile and a gas-to-dust ratio assuming all silicon were in solid form, the mid-IR dust emission can be modelled by solving the radiative transfer equation through the dusty wind. From this  $\dot{M}$  was determined for  $\alpha$  Herculis, finding  $\dot{M} \sim 9 \times 10^{-8} M_{\odot} \text{ yr}^{-1}$ , consistent with Deutsch (1956). This is deemed a lower mass loss limit, as the dust condensation process may not be entirely complete.

The most widely known  $\dot{M}$  prescription is by de Jager et al. (1988). This was developed from a study of 271 predominantly population I galactic stars with spectral types ranging from O to M. Their mass loss rates were taken from various sources in the literature as well as using various methodologies to do so, e.g. dust shell modelling, CO rotational lines and masers (these are discussed in more detail below).

In regards to RSGs, the sample used to derive the de Jager relation only contains 15 RSGs, which are quite diverse in their properties (luminosity, initial mass, metallicity etc), as are the methods adopted to determine  $\dot{M}$  since they taken from various bodies of work. In addition, uncertain and outdated distance measurements are used, which means that  $L_{bol}$  is incorrect, resulting in considerable internal scatter ( $\pm 0.5 \text{ dex}$ ) of the mass loss measurements (Mauron & Josselin, 2011). This spread is significant, as it's the difference between the star losing the whole envelope or virtually none of it (Beasor et al., 2020), which has considerable implications for how the star evolves and the classification of the resulting SN. Lastly, it has also been shown in Beasor et al. (2020) to greatly overestimate the total amount of mass lost for the highest mass objects in post-MS phases, again which has important ramifications for the evolution of RSGs. The de Jager prescription, however, is incorporated heavily in stellar evolution models. This is discussed in more depth in Section 1.4.3.

More recent prescriptions use various techniques to determine  $\dot{M}$ . A study by van Loon et al. (2005) use a sample of galactic and LMC AGB stars and RSGs and measured  $\dot{M}$  by modelling their SEDs using radiative transfer code DUSTY (more details on DUSTY in Section 3.2). The limitation of this prescription is that it solely applies to 'dust enshrouded' stars, which in turn means that it only favours stars with particularly high

---

mass loss rates and cannot be applied if the circumstellar envelope is not very dusty. Similarly, methods that include objects that emit masers (e.g. [Goldman et al., 2017](#)) are biased towards higher  $\dot{M}$  RSGs.

Other methods of obtaining a mass loss rate for cool supergiants include modelling the molecular emission lines of the wind (230 GHz, 115 GHz) using rotationally excited lines of carbon monoxide (CO), a method also used to study the circumstellar dust shells of AGB stars as they are a powerful diagnostic for the study of circumstellar envelopes. (e.g. Knapp et al., 1982). To derive  $\dot{M}$  from CO lines, modelling with radiative transfer codes of the dust and line emission are used (see work by, Groenewegen, 1994; Schöier & Olofsson, 2001; Decin et al., 2006; De Beck et al., 2010; Matsuura et al., 2016). This method finds higher  $\dot{M}$  compared to previous approaches and the ability to observe these molecular lines unveils details relating to profiles of kinetic temperature, expansion velocity, and density (Decin et al., 2006). From these studies, the range in  $\dot{M}$  for RSGs is found to be as low as  $\sim 5 \times 10^{-9}$  in Schöier & Olofsson (2001) and as high as  $3 \times 10^{-4}$  (see both, Decin et al., 2006; Matsuura et al., 2016).

A study by Beasor et al. (2020) expanded on previous empirical mass loss prescriptions by including a current mass parameter instead of only scaling with luminosity and effective temperature, which means it also takes into account the surface gravity of the star. This results in more than one possible  $\dot{M}$  for the same position on the HR diagram, but this degeneracy can be broken when studying RSGs in coeval clusters with known initial masses. They determine  $\dot{M}$  for the RSGs in both NGC 2004 and RSGC1 from mid-IR modelling of SEDs using radiative transfer code DUSTY. This finds a new initial mass-dependent  $\dot{M}$  prescription that finds mass-loss rates lower than previously derived prescriptions. This indicates that for single stars, RSGs cannot lose enough envelope mass through quiescent winds and will therefore die as a hydrogen-rich SN, providing there are no additional stripping mechanisms at play. The implications of implementing this new lower prescription into stellar evolution models is discussed in Section 1.4.3.

As previously mentioned, the results from Beasor et al. (2020) show that quiescent mass-loss is ineffective at removing the stellar envelope, however this doesn't rule out the eruptive, episodic mass loss similar to what is seen for Luminous Blue Variables (LBVs) (Smith, 2006). A few RSGs with these seemingly high mass loss rates, e.g. VY Canis Majoris and VX Sagittarii (hereafter, VY CMa and VX Sgr) are thought to represent this very fast stage of evolution defined by a high mass loss rate, often referred to as a 'superwind' phase (Humphreys & Lockwood, 1972).

Suggestive evidence for a superwind phase include early time radiation from IIP SNe

imply large CSM. If the CSM is optically thick, there is a delay in the shock breakout, allowing further cooling before the explosion erupts through the stars surface. This results in a quicker rise in the optical light-curve, with less time for the radiation to move to the optical (Moriya et al., 2017). Flash spectroscopy, which can be used to probe the CSM, finds that the density of the CSM compared to that of pre-SN RSGs such as Betelgeuse, is orders of magnitude more dense (Harper et al., 2001).

In a study by Bruch et al. (2021), of the 10 events for which rapid follow-up spectroscopy within 2 days was obtained, 6-8 displayed flash-ionised spectral features, which is evidence for transient emission from a surrounding distribution of CSM. This suggests that large fractions of IIP SNe may possibly display evidence for dense CSM around the progenitor if they are capable of being observed early enough. In the example of SN2013fs discussed in Moriya et al. (2017), which was detected caught with in a few hours after the explosion and its first spectrum was taken in about 6 hours after the explosion. It was found to have a flash spectroscopic feature with narrow lines indicating the existence of dense CSM. Although, the narrow emission disappeared after a few days and the spectra changed to what would be expected from a typical IIP SN. Yaron et al. (2017) suggest that the dense CSM needed to explain the early SN properties of SN 2013fs is a manifestation of the increase of the progenitor's  $\dot{M}$  prior to the explosion. Light-curve modelling from Morozova et al. (2017) also suggests that a dense CSM located at the location of the progenitor is necessary to explain the early light-curve properties of SN2013fs.

Estimations can be made for how long a superwind phase would need to last in order for enough envelope to be stripped to have a significant affect on the evolution of the star. In Davies, Crowther & Beasor (2018), they discuss that stars undergoing this phase may appear as OH/IR stars, exhibiting large infrared excesses and circumstellar maser emission. They find for the LMC, 4 out of 73 or their cool supergiants have OH masers and  $L_{\text{bol}} > 5$ . Therefore, if all OH/IR maser emitting RSGs experience a superwind phase, assuming the RSG lifetime is  $\tau \sim 10^6$  years, this would imply a superwind phase lasting  $\sim 5 - 6 \times 10^4$  years which would require a mass loss rate of  $\dot{M} \sim 10^{-4} M_{\odot} \text{yr}^{-1}$  to lose several solar masses of envelope, significant enough to affect the stars' evolution. Decin et al. (2006) similarly quantify a possible superwind phase for VY Cma using CO emission lines showing that the star experienced an episode of high mass loss  $\sim 3.2 \times 10^{-4} M_{\odot} \text{yr}^{-1}$  roughly 1000 years ago, lasting approximately 100 years, followed by a relatively low  $\dot{M}$  phase  $\sim 1 \times 10^{-6} M_{\odot} \text{yr}^{-1}$  lasting a further  $\sim 800$  years. They then estimated the current mass loss rate for VY CMA to be  $8 \times 10^{-4} M_{\odot} \text{yr}^{-1}$ . In

Chapter 3, a similar study is carried out, investigating the lengths of superwind phases for M31 RSGs.

### 1.4.3 $\dot{M}$ implemented in stellar models

Despite the inability to derive a mass loss prescription from first principles, one can instead be empirically derived and put into stellar models, as discussed earlier in Section 1.4.2, as seen in the works of [de Jager et al. \(1988\)](#); [van Loon et al. \(2005\)](#); [Beasor et al. \(2020\)](#) etc, where for a given luminosity, there is a corresponding mass loss rate. Figure 1.4 shows evolutionary tracks on a HR diagram as a result of 3 separate mass loss prescriptions implemented into stellar models. Panel (a) of Figure 1.4 depicts the evolutionary tracks from [Maeder & Meynet \(2000\)](#) from the GENEVA stellar evolution code.

The main predictions for the fates of RSGs from the [Maeder & Meynet \(2000\)](#) GENEVA tracks are as follows:

- A  $25M_{\odot}$  will evolve to the cool supergiant phase where it will die as a IIP hydrogen-rich SN. This places a maximum RSG progenitor mass at most likely somewhere between  $25 - 30M_{\odot}$ .
- A  $40M_{\odot}$  will experience a short-lived RSG phase before evolving back towards the blue side of the HR diagram where it will eventually die as hydrogen-poor type Ib/c SN.
- For stars with initial masses  $60M_{\odot}$  and above,  $\dot{M}$  is high and so there is already not enough envelope mass left to expand and cool, so they never reach the RSG phase.

The GENEVA models were updated in [Ekström et al. \(2012\)](#), which included revisions to properties such as chemical abundances, opacities, overshooting etc. However, the crucial parameter that was changed was  $\dot{M}$ . In the earlier [Maeder & Meynet \(2000\)](#) models, when the star cools below  $\sim 10,000\text{K}$  the [de Jager et al. \(1988\)](#) prescription is implemented for the cool supergiant phase, whereas the [Ekström et al. \(2012\)](#) models use a combination of the [de Jager et al. \(1988\)](#), [van Loon et al. \(1999\)](#) and [Sylvester et al. \(1998\)](#) mass loss prescriptions in the cool regime for stars with masses greater than  $15M_{\odot}$  and  $\log T_{\text{eff}} > 3.7$ . Further to this, an additional criteria implemented, where for stars with mass greater than  $20M_{\odot}$ , if goes above 5x the Eddington limit (where the Eddington limit is the theoretical maximum luminosity beyond which radiation pressure

will overcome gravity) then the mass loss rate is multiplied by a further arbitrary factor of 3. This is not found from an empirical measurement, but it does stop the star from being super Eddington and helps sustain stability. The result of this increase in  $\dot{M}$  is what governs the blue-ward evolution post RSG phase for  $20M_{\odot}$  stars in these models which we do not see for the [Maeder & Meynet \(2000\)](#) models, shown in panel (b) of [Figure 1.4](#).

Using the [Beasor et al. \(2020\)](#) prescription, which is previously described in detail, uses RSGs in clusters rather than field RSGs as used in the [de Jager et al. \(1988\)](#) method. This accounts for uncertain distances and initial masses by assuming they are all the same for each cluster. Then by using several clusters each with different initial mass RSG samples, then luminosity can be used as a proxy for evolution. In the [Beasor et al. \(2021\)](#) paper, the effects of the chosen  $\dot{M}$  prescription implemented into the MESA-MIST stellar evolution code (see, [Paxton et al., 2011b](#)) is discussed. As with the GENEVA models, the MESA models also adopt the [de Jager et al. \(1988\)](#) prescription for the cool supergiant phase. Panel (c) shows the evolutionary tracks when the [Beasor et al. \(2020\)](#) prescription is implemented into the MESA models. In their comparative study with MESA-MIST, they keep all parameters the same except for changing  $\dot{M}$  in cool phase, where MESA previously used exclusively the de Jager prescription, with no added enhancement like in the GENEVA models. They found the HR diagram and the end points of evolution looked essentially the same for the mass range studied ( $12 - 27M_{\odot}$ ), where there are no stars losing enough mass to evolve to the blue. This suggests there is no single star pathway for WR/stripped SNe. This is further supported by the fact most massive stars above  $30M_{\odot}$  are in binary systems (e.g. [Sana et al., 2012](#); [Bodensteiner et al., 2021](#)). Further, in the example of a  $20M_{\odot}$ , GENEVA were predicting a mass loss of  $\sim 10M_{\odot}$  forcing it back blue-ward, however [Beasor et al. \(2020\)](#) only find a mass loss of  $1 - 2M_{\odot}$ , thus being much below the threshold to remove the hydrogen envelope and move it back to the blue. This means that  $\dot{M}$  isn't that important in driving stars to the blue. Another point discussed is the relation between initial and final mass of RSG. The final mass in MESA-MIST when using the de Jager prescription causes a plateau at the highest masses  $\sim 25M_{\odot}$ , whereas [Beasor et al. \(2021\)](#) find a positive correlation, which indicates that there is also a direct positive correlation between initial mass and envelope mass. If this is the case in nature, its possible that if you could measure envelope mass after SN, you could then use it to determine initial mass. The effects of the Beasor prescription in MESA-MIST on the HD limit is discussed in detail in [Section 2.3.4](#).

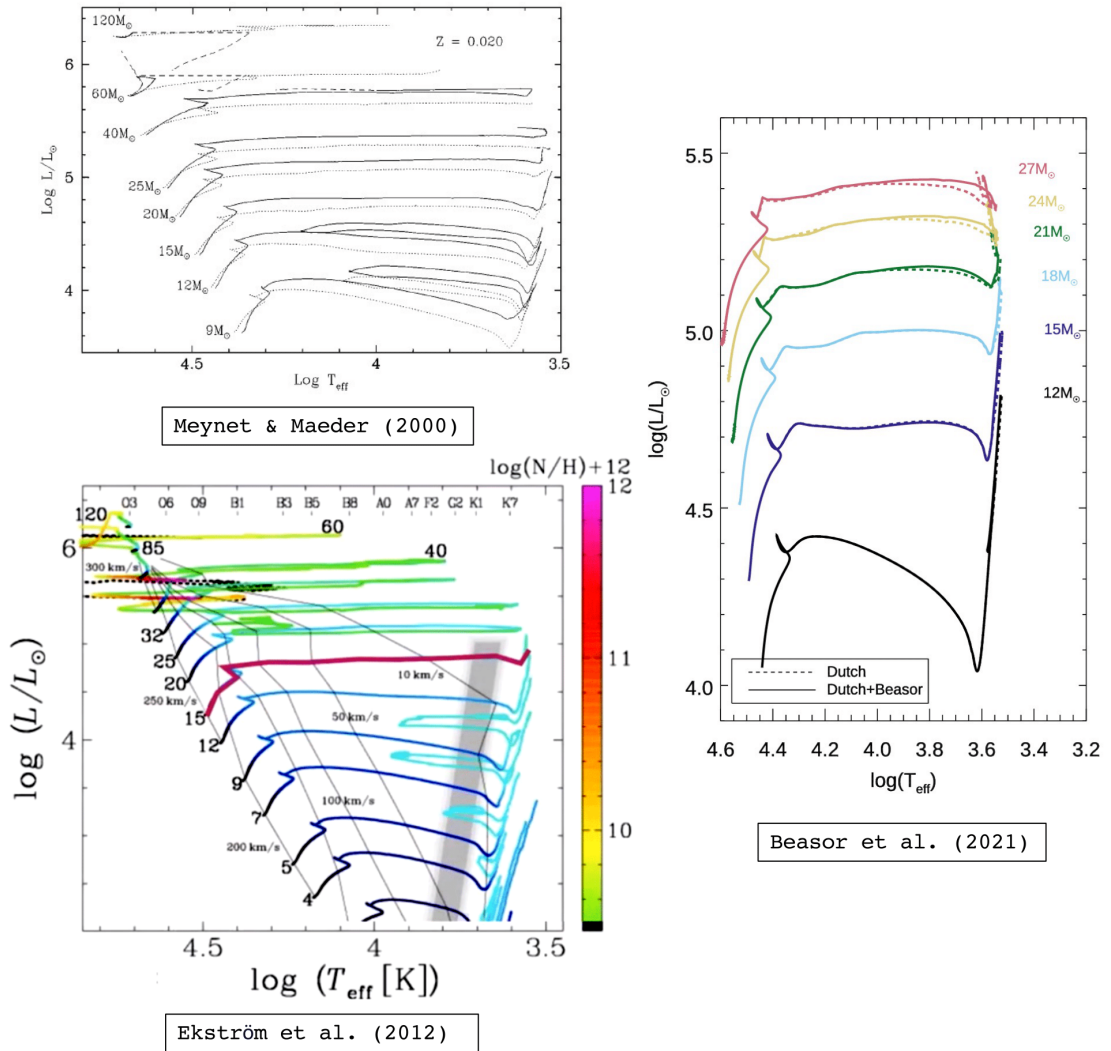


FIGURE 1.4: Evolutionary tracks from (a) Maeder & Meynet (2000), (b) Ekström et al. (2012), (c) Beasor et al. (2021), showing the ramifications for evolution when using different mass loss prescriptions in stellar models.

## 1.5 This Thesis

To summarise the motivations of this thesis, I will attempt to explore **3** key unanswered questions in the topics of massive stellar evolution. These questions are:

### 1. The Humphreys-Davidson limit of RSGs:

- What is the HD-limit for RSGs in M31?
- How does it compare to the limit found for the LMC and SMC in Davies, Crowther & Beasor (2018)?
- Is there a metallicity dependence/are line-driven winds responsible for the HD-limit?

### 2. Mass loss rates of RSGs:

- What are the mass loss rates of M31 RSGs?
- Are any M31 RSGs experiencing a superwind phase?
- How long would this superwind phase need to last to remove the entire envelope of an RSG?

### 3. Using machine learning techniques to estimate red supergiant mass loss rates and luminosities:

- Can machine learning techniques be used to find a quicker and cheaper way of scaling up the study in Chapter 3?
- Can this model be successfully deployed onto an unseen sample of M33 RSGs to determine their mass loss rates and luminosities, thereby expanding our sample size and putting tighter constraints on  $\dot{M}$  for the superwind phase?

Question **1** will be explored in detail in Chapter 2, where we investigate the Humphreys-Davidson limit of RSGs in M31 and compare to both observations and model prediction of the HD limit for both the LMC and SMC. Chapter 3 addresses question **2**, using radiative transfer code DUSTY to obtain mass loss rates of M31 RSGs and put constraints on the timescales of possible 'superwind' phases. In Chapter 4, we explore question **3** by using machine learning techniques to train a model to make predictions of M31 RSG mass loss rates and luminosities. We then deploy this model on a sample of unseen M33 RSG data to see if we can determine mass loss rates and luminosities for those RSGs

too. Finally, in Chapter 5 presents a summary of the results and findings of the work carried out in this thesis.

## Chapter 2

# The Humphreys-Davidson limit of Red Supergiants in Local Group Galaxies

The empirical upper limit to Red Supergiant (RSG) luminosity, known as the Humphreys-Davidson (HD) limit, has been commonly explained as being caused by the stripping of stellar envelopes by metallicity-dependent, line-driven winds. As such, the theoretical expectation is that the HD limit should be higher at lower metallicity, where weaker mass-loss rates mean that higher initial masses are required for an envelope to be stripped. In this chapter, we test this prediction by measuring the luminosity function of RSGs in M31 and comparing to those in the LMC and SMC as well as compare to model predictions using the GENEVA stellar evolution models.

## 2.1 Method

### 2.1.1 Compiling a sample of M31 red supergiants

To compile a sample of RSGs candidates in M31, we use photometry from the *Spitzer* mid-infrared point source survey, (IRAC/MIPS:  $3.6\mu\text{m}$ ,  $4.5\mu\text{m}$ ,  $5.8\mu\text{m}$ ,  $8.0\mu\text{m}$  and  $24\mu\text{m}$ ) from [Khan 2017](#) which utilises the IRAC and MIPS survey data from [Mould et al. \(2008\)](#) and [Gordon et al. \(2006\)](#), respectively. The image quality details of the Spitzer telescope can be seen in Table 2.1. RSGs tend to have excess in the mid-IR due to the presence of warm dust stellar winds which can obscure stars at optical wavelengths. Therefore, any particularly dusty or ‘dust enshrouded’ stars ([van Loon et al.](#),

2005) may be too faint to be detected by optical or possibly even near-IR surveys. Additionally, at these longer wavelengths there is less sensitivity to interstellar reddening. By using the Khan catalogue as a basis, we expect to have a much higher level of completeness than can be achieved from optical or near-IR surveys.

TABLE 2.1: The full width half maximum (FWHM) and spatial resolutions for the Spitzer IRAC and MIPS wavebands used in this work [Fazio et al. \(2004\)](#); [Rieke et al. \(2004\)](#).

Wavelength	FWHM (")	Spatial Resolution (at the distance to M31 (pc))
IRAC1 (3.6 $\mu$ m)	1.66	6.12
IRAC2 (4.5 $\mu$ m)	1.72	6.34
IRAC3 (5.8 $\mu$ m)	1.88	6.93
IRAC4 (8.0 $\mu$ m)	1.98	7.30
MIPS1 (24 $\mu$ m)	5.90	21.76

To locate our target stars, we first constructed colour-magnitude diagrams (CMDs) using the *Spitzer* photometry ([Khan, 2017](#)). Next, we overplotted a sample of known RSGs from [Massey & Evans \(2016\)](#), to define the location of our target stars in mid-IR colour-magnitude space. We place a colour threshold at the blue limit of known RSGs in M31, as well as a magnitude cut corresponding to  $\log(L/L_{\odot}) \sim 4.8$ , using a distance to M31 of 770 kpc ([Karachentsev et al., 2004](#)) determined from distance calculations to Cepheid Variables using their period-luminosity relationship, which is consistent with the distance calculated in [Li et al. \(2021\)](#). This was to avoid any Asymptotic Giant Branch stars (AGBs) or Red Giants contaminating our sample which have similar luminosities to the lowest mass RSGs ([Ferrari et al. 1970](#); [Lamb et al. 1976](#); [Brunish et al. 1986](#)). The colour and magnitude cuts are listed in Table 2.2. In addition to this, we made a radius cut at 40 kpc (where the dust-free exponential disk of scale length  $R_d = 5.3 \pm 5$  kpc, [Courteau et al. 2011](#)), using the physical de-projected radius, assuming an inclination angle of  $77.5^{\circ}$  ([Tempel et al., 2010](#)).

Next we cross-matched our candidates with the RSG catalogues from [Massey & Evans \(2016\)](#) and [Gordon et al. \(2016\)](#) to ensure all the brightest candidates from these optical surveys had been re-acquired through our mid-IR cuts. We found 10 objects with  $\log(L/L_{\odot}) > 5$  from [Massey & Evans \(2016\)](#) and 14 from [Gordon et al. \(2016\)](#) that do not appear in the Khan catalogue, (reasons for which are discussed in Section 2.1.3), which are then manually added in to our sample of RSG candidates. This results in a sample of 7893 RSG candidates so far. These stars are then cross-matched to the

following catalogues to obtain multi-wavelength photometry and astrometry for each candidate:

- Local Group Galaxy Survey (LGGS) UBVRI photometry [Massey et al. \(2006\)](#).
- Gaia EDR3 photometry (BP and RP bands) and astrometry (proper motion and parallax) [Gaia Collaboration \(2020\)](#).
- Two Micron All Sky Survey (2MASS) JHK photometry [Cutri et al. \(2003\)](#).

After co-adding the optical/near-IR photometry, we applied an extra colour criteria of  $\text{Gaia Bp-Rp} > 1$  to further screen out any objects that are too blue in colour to be RSGs. We then also use Gaia astrometry as a method of removing foreground stars. We aim for as high a completion rate as possible, so we remove any objects with a proper motion deviating more than  $4\sigma$  from the motion of M31 ([Salomon et al., 2020](#)). This constraint of  $4\sigma$  was a trade-off between capturing all the possible M31 RSGs and limiting the number of foreground objects contaminating our sample and potentially biasing the high end of our luminosity function. If a  $5\sigma$  cut-off is applied, we are left with 377 objects (before any high resolution image checks) which would be excluding just over 30 objects, some of which are confirmed RSGs. A  $3\sigma$  cut-off results in 1012 objects remaining, and when cross-matched against known RSG catalogues ([Massey & Evans \(2016\)](#); [Gordon et al. \(2016\)](#) etc) we do not find any more luminous confirmed or candidate RSGs that would change the morphology of the luminosity function and resulting  $L_{\text{max}}$ .

The total number of RSG candidates found and used in this work is 415, which can be seen over-plotted on an image of M31 in [Figure 2.1](#). Other studies looking at M31 RSGs, ([Ren et al., 2021a](#), e.g.) have larger sample sizes of RSGs, but the main aim of those studies is compiling a complete sample of RSGs down to the dimmest stars. In the present work, we apply stringent constraints on our sample (i.e. placing a lower magnitude limit corresponding to  $\log(L/L_{\odot})=4.8$ ) with a greater emphasis on the higher end of the luminosity function by locating RSGs with luminosity greater than this. Subsequently, in [Section 2.3.3.1](#), we show the effects of sample size on  $L_{\text{max}}$  and how using a larger sample size of RSGs would not affect our  $L_{\text{max}}$  estimates.

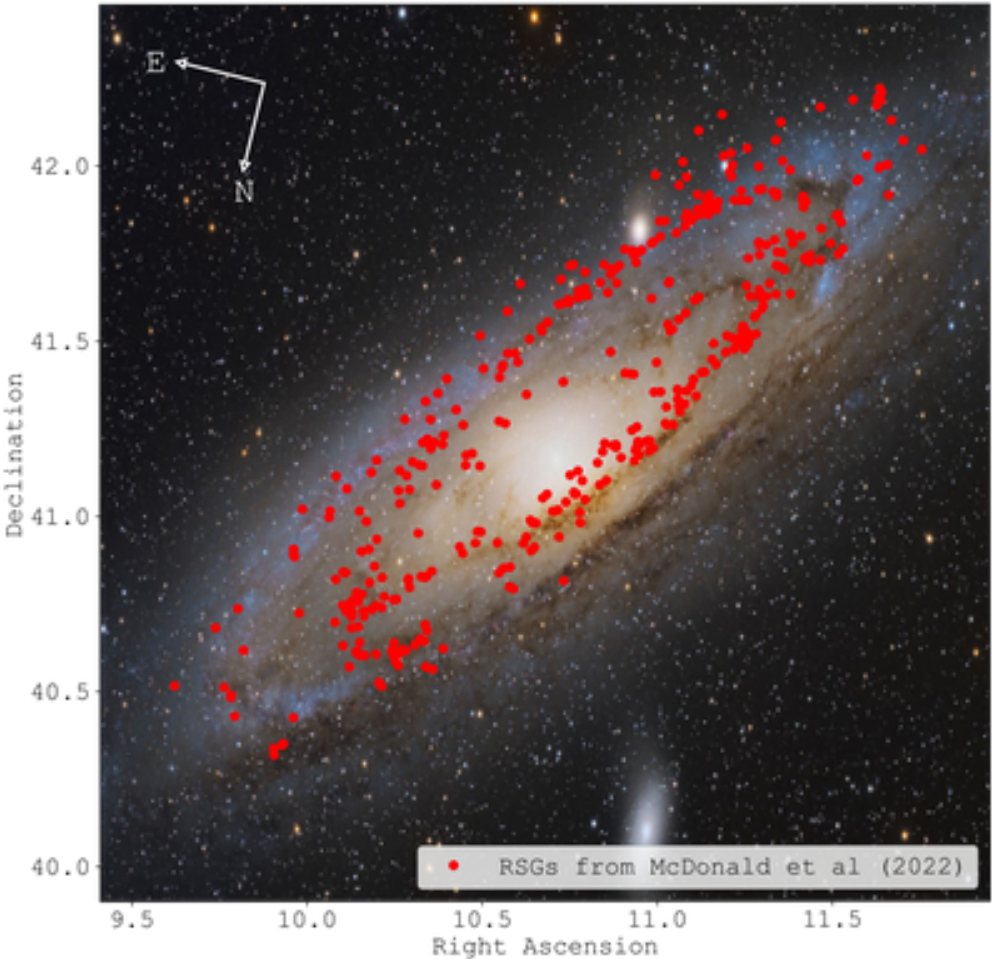


FIGURE 2.1: The right ascension and declination of the 415 RSG candidates used in this study of M31.

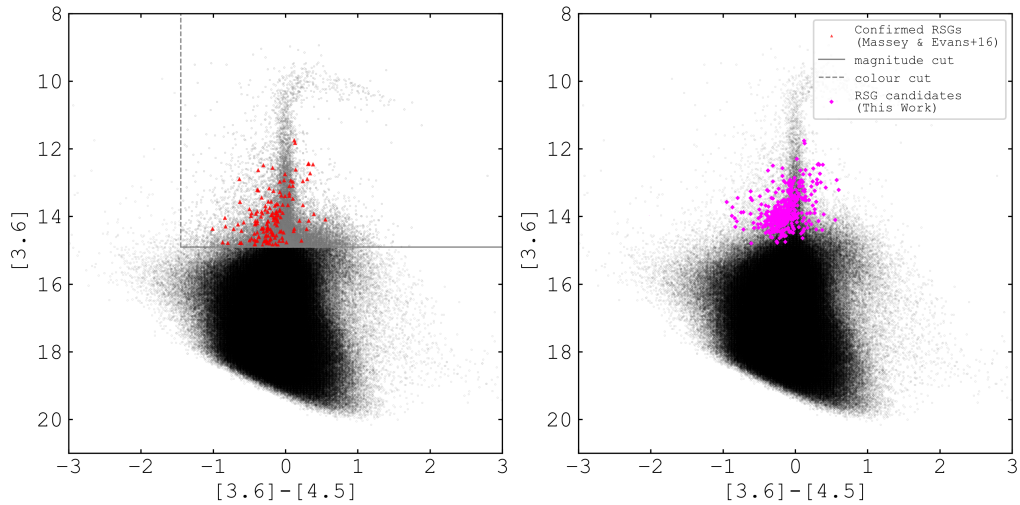


FIGURE 2.2: (a) A colour magnitude diagram, where the black points in both panels indicate all the M31 point sources detected by Spitzer IRAC/MIPS (Khan, 2017). The grey points show the sources which fit the criteria to be a likely RSG candidate based on the colour (dashed grey line) and magnitude (solid grey line) cuts applied, to find the first constraint towards establishing a sample of RSG candidates. The red triangles indicate known M31 RSGs with determined spectral classifications by Massey & Evans (2016) from which we have based our colour and magnitude cuts around. All other mid-IR cuts can be seen in Table 2.2. (b) The magenta points indicate all the RSG candidates (with available Spitzer mid-IR photometry) we find and use in the present work after all photometric and astrometric cuts have been applied.

### 2.1.2 Correcting for foreground extinction

Since we do not have associated spectroscopic information for all of these RSG candidates, we cannot correct for extinction using intrinsic colours. Furthermore, the colours of RSGs are often affected by circumstellar extinction, which unlike interstellar extinction does not reduce the observed bolometric flux (see Section 2.1.3). For these reasons, we must obtain an estimate of the foreground extinction separately. To do this we utilise an M31 extinction map (Dalcanton et al., 2015), surveyed by The Panchromatic Hubble Andromeda Treasury project (PHAT, Dalcanton et al., 2012). This provides a foreground extinction correction,  $A_v$ , for any of our RSG candidates that are situated within the north-east quadrant of M31. Each RSG candidate was then de-reddened according to the Cardelli et al. (1989) reddening law for the optical photometry, and Rieke & Lebofsky (1985) for the near-IR.

The candidates which are located outside the PHAT footprint cannot be individually extinction corrected. For these stars, we adopt the median  $A_v$  of the 149 RSGs that

TABLE 2.2: The *Spitzer* colour and magnitude cuts that were applied to locate our target stars. The cuts are based on the colours and magnitudes of known confirmed RSGs from Massey & Evans (2016), indicated by the red triangles in Fig 2.2. All the *Spitzer* point source detections for M31 are shown in black.

<i>Spitzer</i> magnitudes (IRAC/MIPS)	Magnitude cut (mags)
IRAC1 ( $3.6\mu\text{m}$ )	14.9
IRAC2 ( $4.5\mu\text{m}$ )	15.0
IRAC3 ( $5.8\mu\text{m}$ )	14.8
IRAC4 ( $8.0\mu\text{m}$ )	14.8
MIPS1 ( $24\mu\text{m}$ )	12.8
<i>Spitzer</i> colours (IRAC/MIPS)	Colour cut (mags)
[3.6] - [4.5]	-1.45
[3.6] - [5.8]	-1.3
[3.6] - [8.0]	-1.0
[5.8] - [8.0]	-0.6
[3.6] - [24]	0.0
[8.0] - [24]	0.0
[4.5] - [24]	0.4

are covered by PHAT. From the median and the 68% probability limits, we determine an average  $A_v = 1.19 \pm 0.10$ .

To investigate whether the assumption of using a uniform  $A_v$  for the stars not covered by PHAT introduces any systematics into our results, we determine the bolometric luminosity of the 149 candidates using both their individual  $A_v$  from the extinction map and the median  $A_v = 1.19$ . shows that the number of objects in each bin of the luminosity function when using both the average uniform  $A_v$  and the individual PHAT extinction corrections. Though the exact number of objects in each bin is different, the two are consistent to within the Poisson errors (See Figure 2.3). Furthermore,  $L_{\text{max}}$  is the same whichever extinction correction method is used. Therefore, we conclude that the assumption of a uniform  $A_v$  results in a luminosity distribution and  $L_{\text{max}}$  which are stable to within the error margin.

### 2.1.3 Determining bolometric luminosity

We converted the de-reddened photometry into fluxes using Vega calibrated zero point fluxes for each filter from the SVO Filter Profile Service (Rodrigo & Solano, 2020). Using these fluxes, we plot spectral energy distributions (SEDs) for each RSG candidate

and integrate under the SED to determine bolometric luminosity, using IDL routine `int_tabulated`, adopting an M31 distance modulus of 24.4 (Karachentsev et al., 2004). In doing so, we make the same assumption as DCB18 that any flux lost to absorption by circumstellar material is re-radiated at longer wavelengths, and so by integrating under the SED from the optical to the mid-IR we obtain all the star’s flux. Figure 2.4 shows the SEDs of the most luminous candidates with complete photometry from optical to the mid-IR. In Section 2.2.1.1, we discuss in more detail the brightest RSG candidates as well as any bright objects which were rejected from our sample.

A few of the objects in our sample have incomplete photometric coverage, often due to them being undetected at longer wavelengths. These objects were identified when comparing the sample of stars found in the present work with previously compiled M31 RSG catalogues (Massey & Evans, 2016; Gordon et al., 2016)), where we found 24 stars with  $\log(L/L_{\odot}) > 5$  were missed from our study. *Spitzer*/IRAC and MIPS images<sup>1</sup> of these objects show they appear to be spatially extended in the mid-IR, and as a result are absent from the Khan (2017) point source catalogue. To estimate luminosities of these objects, we employ an alternative method of using a K-band bolometric correction ( $BC_K$ ) which we outline next.

#### 2.1.4 Bolometric corrections

In this section, we use the RSGs with complete photometric coverage to determine bolometric corrections (BCs) appropriate for M31. We use K-band photometry since a  $BC_K$  at this wavelength does not appear to be sensitive to spectral type (DCB18). Furthermore, the extinction at this wavelength in mag is only around 1/10th of that in the V-band. The bolometric correction is then used to estimate luminosities for the stars with incomplete SED coverage.

We individually de-redden the near-IR photometry, prior to converting to bolometric luminosity by employing either (a) a uniform  $A_K = 0.13 \pm 0.02$  found from the median  $A_v = 1.19 \pm 0.1$  and the relation  $A_K = 0.11A_v$  from Rieke & Lebofsky (1985); or (b) the individual  $A_v$  if situated in the extinction map and finding  $A_K$  using the same  $A_v/A_K$  relation. We then calculate BC by finding  $M_{BOL} - M_{\lambda}$  for each of our RSG candidates, see Figure 2.5. We find the median  $BC_K = 2.71 \pm 0.12$  as well as  $BC_{IRAC1} = 3.18 \pm 0.15$ , where the uncertainty is the standard deviation. We also plot

<sup>1</sup>*Spitzer* images were taken from the NASA/IPAC Infrared Science Archive

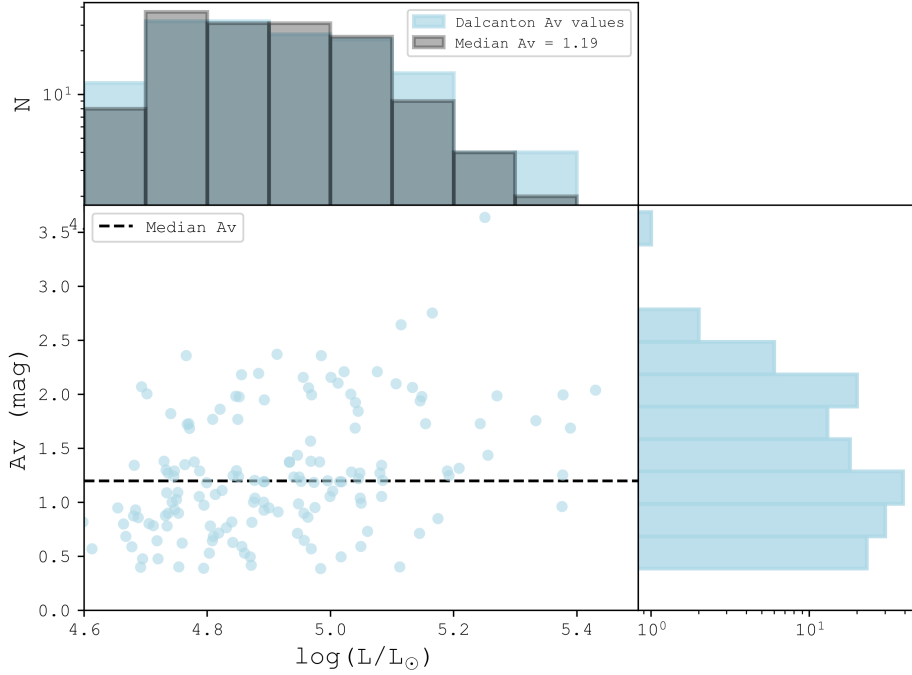


FIGURE 2.3: Top panel: A luminosity distribution of the 149 RSG candidates found in the region of M31 surveyed by HST PHAT (Dalcanton et al., 2012). The luminosities in light blue are determined using  $A_v$  taken directly from the Dalcanton et al. (2015) M31 extinction map. The grey distribution is the same stars but with their luminosities determined using  $A_v = 1.19 \pm 0.10$  which corresponds to the median of all the RSGs located within the PHAT surveyed region. Middle panel: Bolometric luminosity vs  $A_v$  of 149 RSG candidates present in the M31 extinction map. Right Panel: A distribution of the visual extinction values for each star, taken from the extinction map.

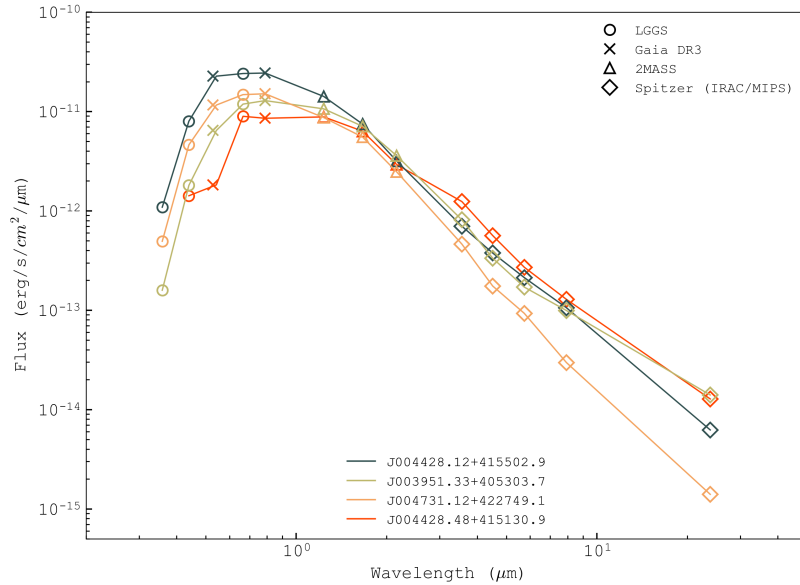


FIGURE 2.4: Spectral energy distributions of the most luminous Red Supergiant (RSG) candidates. These have  $\log(L/L_{\odot}) > 5.4$  with complete de-reddened photometry ranging from the optical through to the mid-infrared. The symbols in the upper legend indicate the catalogue source of the photometry and the lower legend provides the LGGs star name for each candidate. Each of these luminous RSGs are discussed in more detail in Section 2.2.1.1.

a binned average of  $BC_{\lambda}$  with  $M_{BOL}$  to show that within the uncertainties there is no systematic trend with brightness.

The  $BC_K$  we find for M31 is consistent with those found in previous studies for other local group galaxies. There is a good agreement with the median BC across spectral classes K and later derived for the LMC, with a median BC of  $2.81 \pm 0.08$  and SMC with  $2.60 \pm 0.09$  both from DCB18 as well as  $2.81 \pm 0.10$  for the Milky Way from Davies & Beasor (2018).

## 2.2 Results

### 2.2.1 The RSG luminosity function

The most important candidates for our investigation into the HD limit are those occupying the high end of the luminosity function. The photometric and astrometric constraints implemented, previously discussed in Section 2.1.1, ensure the stars in our sample have the appropriate colours, magnitudes and proper motion consistent with

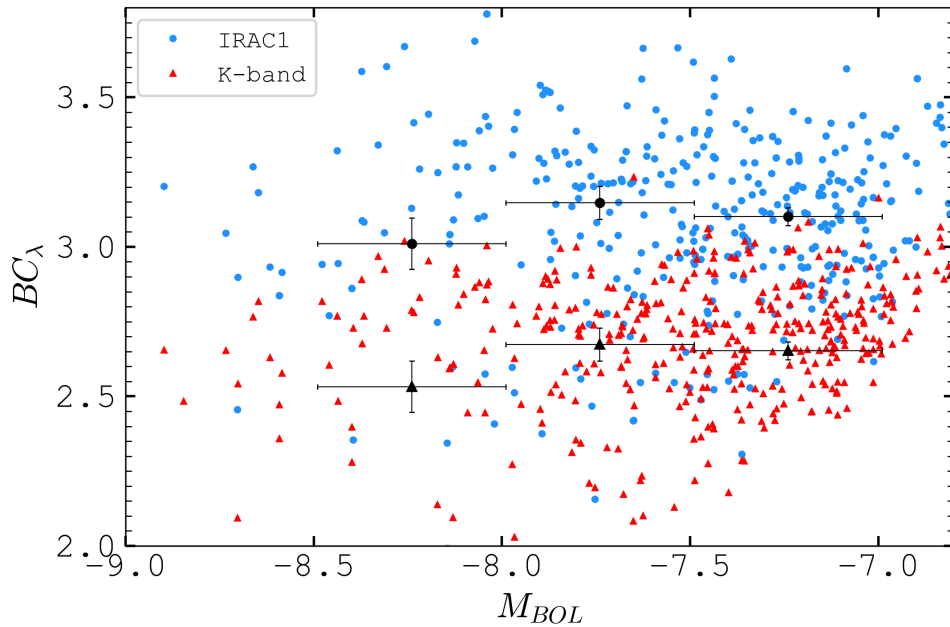


FIGURE 2.5: The offset  $M_{bol} - M_{\lambda}$  is used to estimate the bolometric correction for each RSG candidate, in both the K-band seen in red and IRAC1  $3.6\mu\text{m}$  band, in blue.

being RSG candidates in M31. However, only approximately 25% of the sample has spectroscopic confirmation. This means that there may be some contamination. Therefore, a further verification step we applied was to inspect high spatial resolution archival images such as HST (and HST PHAT where possible), such that all objects at the bright end of the luminosity function ( $\log(L/L_{\odot}) > 5.3$ ) are consistent with being single sources.

The observational luminosity function of M31 RSGs is shown in Figure 2.6 by the light grey distribution. It shows the number of RSG candidates per log luminosity bin for M31, found in the present work. The two darker grey distributions show the number of RSG candidates we use in this study which are also found in previous M31 RSG studies. For the brightest RSGs, their luminosities and spectral classifications can be seen in Table 2.3. The most luminous candidates are discussed in more detail below.

### 2.2.1.1 Most luminous M31 RSG candidates and $L_{\text{max}}$

1. **J004520.67+414717.3**: This object has previously been assigned a spectral classification of M1I with a luminosity of  $\log(L/L_{\odot}) = 5.81$  by [Massey & Evans](#)

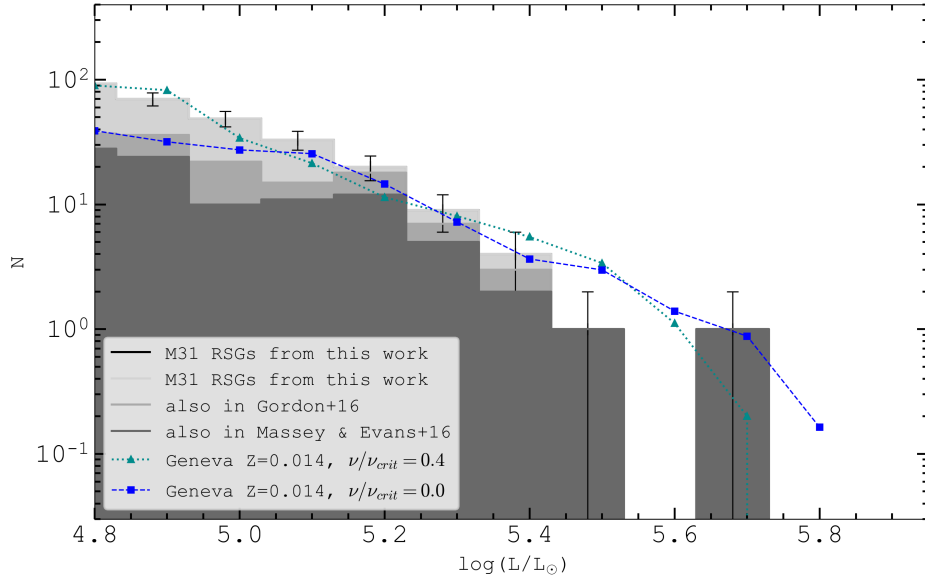


FIGURE 2.6: The Red Supergiant luminosity distribution for M31. The observed luminosity distribution from this work is shown in light grey, with the two darker grey distributions showing the number of RSG candidates we use in this study that are also found in previous M31 RSG studies. Over-plotted are the rotating ( $\nu/\nu_{crit} = 0.0$ ) and non-rotating ( $\nu/\nu_{crit} = 0.4$ ) model predicted distributions from the GENEVA models at solar metallicity ( $Z=0.014$ ) from [Ekström et al. \(2012\)](#). N.b. The brightest star at  $\log(L/L_{\odot}) = 5.71$  cannot be definitively ruled out, but is a borderline M31 candidate due to its proper motion. This is discussed further in Section 2.2.1.1.

(2016) and  $\log(L/L_{\odot}) = 5.94$  by [Gordon et al. \(2016\)](#). In the present work, we determine a luminosity of  $\log(L/L_{\odot}) = 5.75 \pm 0.11$ . This makes this object the brightest RSG candidate we find in M31. However, there are some caveats to the significance of this high luminosity object in regards to  $L_{\max}$ . Firstly, although this object has optical colours consistent with RSGs ( $B-V = 2.68$  and  $V-R = 1.55$ ), the source appears to be sat within spatially extended infrared emission, meaning that it does not appear in the Khan point-source catalogue. As a result its luminosity is determined using a  $BC_K$  where the large uncertainty is dominated by that on the bolometric correction. Further, this candidate has a proper motion which deviates from the M31 proper motion at the  $2\sigma$  level. This raises the possibility that it is a foreground object, which is also suggested in [Massey & Evans \(2016\)](#), as they find the radial velocity of this object overlaps foreground star velocities. This casts further uncertainty on its luminosity as the M31 distance assumed in the luminosity calculation is no longer appropriate if not an M31 member. Since we cannot definitively rule out this object since it has a RSG classification, it remains in our sample. However, we will treat this object with caution in regards to the HD limit.

2. **J004428.12+415502.9**: This candidate has been previously classified as a K2I RSG from [Massey & Evans \(2016\)](#) with a luminosity of  $\log(L/L_{\odot}) = 5.64$ , as well as a luminosity of  $\log(L/L_{\odot}) = 5.89$  from [Gordon et al. \(2016\)](#). It has also been described as a Long Period Variable candidate in [Soraisam et al. \(2018\)](#) in their study of RSG variability in M31. We initially found a luminosity of  $\log(L/L_{\odot}) = 5.63$ , but closer inspection of SDSS images show it to be two blended stars of similar colour. The brighter of the two stars has astrometry consistent with M31, but the fainter has a high proper motion and is therefore likely to be a foreground object. From the ratio of the two stars' fluxes, we estimate that the M31 star has an apparent brightness 0.1dex greater than the foreground star. This leads to a revised brightness for the RSG of  $\log(L/L_{\odot}) = 5.53 \pm 0.03$ .
3. **J004539.99+415404.1**: This star is classified as a M3I RSG with a luminosity of  $\log(L/L_{\odot}) = 5.81$  in [Massey & Evans \(2016\)](#) and  $\log(L/L_{\odot}) = 6.09$  in [Gordon et al. \(2016\)](#). In the present work, we initially calculated a luminosity of  $\log(L/L_{\odot}) = 5.81$  from its SED, but in HST images and in Gaia DR3 we find that the object resolves into two sources. One source has no Gaia astrometry but the other has a large detectable proper motion in Gaia DR3, indicating foreground membership. The two sources also have comparable brightnesses and colours at Gaia Bp and Rp wavelengths (the RSG candidate:  $Bp-Rp = 2.389475$  and the

nearby red object:  $B_p - R_p = 2.389486$ . We have full SED coverage for this object, but the derived luminosity will consequently contain flux contributing from both sources in the near and mid-IR, which results in an over-estimation of the objects luminosity. Under the assumption that the star with no astrometry is an M31 member, and that the stars are of comparable apparent brightness at all wavelengths, we use the 2MASS K-band photometry (which detects these objects as only one source) and allocate a K-band flux to the RSG, that is half of the total K-band flux. We then use a K-band BC to determine its luminosity, which we find to be  $\log(L/L_\odot) = 5.49 \pm 0.09$ .

4. **J003951.33+405303.7**: This candidate has been previously identified as a ‘possible RSG’ in [Massey et al. \(2009\)](#), but has not been spectroscopically confirmed. This object has optical colours consistent with RSGs and in SDSS images appears as a single object for which we find a luminosity of  $\log(L/L_\odot) = 5.46 \pm 0.02$ . This object also passed our proper motion constraint of deviating less than 4sigma from the proper motion of M31, consistent with M31 membership. We find no reason to exclude this object based on its high resolution images, therefore it remains in our sample.
5. **J004731.12+422749.1**: This object is a ‘possible RSG’, according to [Gordon et al. \(2016\)](#) with a luminosity of  $\log(L/L_\odot) = 5.53$  but has not been spectroscopically confirmed. This object passed our proper motion cuts and is therefore presumed to be an M31 member. In our work, we determine a luminosity of  $\log(L/L_\odot) = 5.44 \pm 0.04$  and find no reason to reject this object and so it remains in our sample.
6. **J004428.48+415130.9**: This is a confirmed RSG with a spectral type of M1I and a previously determined luminosity of  $\log(L/L_\odot) = 5.60$  by [Massey & Evans \(2016\)](#) and  $\log(L/L_\odot) = 5.64$  by [Gordon et al. \(2016\)](#). The proper motions of this object are consistent with the proper motion of M31, so we presume that this object is an M31 member. Lastly, this star appears to be a single object in HST images for which we find a luminosity of  $\log(L/L_\odot) = 5.43 \pm 0.02$  from its SED.

### 2.2.1.2 Stars rejected from this work

The following objects are those that met both our colour and magnitude criteria and have  $\log(L/L_\odot) > 5.3$ , but were rejected after inspecting their high resolution images. The reasons for rejection are described below:

LGGS Name	RA DEC (J2000)	$\log(L/L_{\odot})$	Classification
J004520.67+414717.3	00 45 20.66 +41 47 17.1	$5.75 \pm 0.11^*$	RSG (M1I)†
J004428.12+415502.9	00 44 28.11 +41 55 02.7	$5.53 \pm 0.03$	RSG (K2I)
J004539.99+415404.1	00 45 39.98 +41 54 03.9	$5.49 \pm 0.09^*$	RSG (M3I)
J003951.33+405303.7	00 39 51.32 +40 53 03.6	$5.46 \pm 0.02$	‘Possible’ RSG
J004731.12+422749.1	00 47 31.04 +42 27 48.2	$5.44 \pm 0.04$	‘Possible’ RSG
J004428.48+415130.9	00 44 28.47 +41 51 30.7	$5.43 \pm 0.02$	RSG (M1I)

TABLE 2.3: The name, position and bolometric luminosity of the RSG candidates with  $\log(L/L_{\odot}) > 5.4$  found in this study. We also provide the SIMBAD object classification of each candidate, assigned by [Massey et al. \(2009\)](#)/[Massey & Evans \(2016\)](#). Full analysis of these objects and their luminosities are described in Section 2.2.1.1. \*The uncertainty of these luminosities is dominated by the error on the  $BC_K$ , discussed further in Section 2.1.3. †This is our borderline candidate which has been previously classified as an M1I supergiants but our caveats for this objects are discussed in Section 2.2.1.1.

1. **J004257.58+411740.1**: Our initial estimate of this star’s luminosity was  $\log(L/L_{\odot}) = 5.81$ . However, despite having both mid-IR and optical colours consistent with RSGs, this object is located within the bulge of M31 where there is little to no star formation occurring making it unlikely to be a massive star. Also, the object appears spatially extended in HST B-band images, consistent with the object being a globular cluster, which is also suggested by [Wirth et al. \(1985\)](#). Therefore, we reject this object from our sample.
2. **J004336.68+410811.8**: This object appears in the [Gordon et al. \(2016\)](#) sample, estimated to have a luminosity of  $\log(L/L_{\odot}) = 5.86$ . It is also mentioned in the [Massey & Evans \(2016\)](#) study as a possible RSG but has no derived luminosity due to the object having no K-band photometry. However, the object is resolved in HST U-band imaging, showing that it is instead a star cluster. The object was rejected from our sample.

### 2.2.1.3 Sample completeness

Inferring an upper luminosity limit of cool supergiants is difficult due to the steep power law present in the RSG luminosity function, as a result of both the initial mass function (IMF) and the short lifetimes of massive stars. This means low number statistics have a strong influence on our results, as  $L_{\max}$  is extremely sensitive to sample size (discussed in more detail in Section 2.3.3.1). Therefore we aim to ensure sample completeness for all RSGs with  $\log(L/L_{\odot}) > 5$ , since we are focused on the high end of the RSG luminosity function and the HD limit. Below this luminosity, we are at more risk of

including contaminating objects. To aim for completeness, as mentioned in Section 2.1, we cross-checked our sample with other M31 RSG catalogues which instead optically select their RSGs, to check all previously identified RSGs were acquired through our mid-IR cuts. There were, however, a small number of objects that were missing from the Khan catalogue, as previously discussed in Section 2.1.3 which are sat in spatially extended mid-IR emission, meaning that they are not point-sources in the mid-IR. Therefore, the only RSGs that could be missed by our sample selection are those which are faint in the optical (e.g. due to circumstellar dust) but also spatially extended in the mid-IR due to confusion with other nearby sources, and hence missing from the point-source catalogue. Any objects absent from the mid-IR point source catalogue, but were bright in optical wavelengths were manually added to our sample. All RSG candidates found in the present work which were *also* found in previous studies can be seen in Figure 2.6. The total number of RSG candidates we found in this study is 415, although for the statistical analysis carried out in the present work (see Section 2.3.2 onward) we take our sample size to be the 117, which is the number of RSGs with  $\log(L/L_{\odot}) > 5$ .

In Massey & Evans (2016), they have a sample of 251 M31 RSGs with assigned spectral classifications, where 50 of these have a luminosity greater than  $\log(L/L_{\odot}) > 5$ . From their sample we have re-acquired all 50 of those with  $\log(L/L_{\odot}) > 5$  in our sample.

The total number of RSGs with  $\log(L/L_{\odot}) > 5$  in Gordon et al. (2016, hereafter, GHJ16,) is 139. We re-acquired 128 of these either with our cuts or were manually added to our sample if not present in the Khan (2017) catalogue. The remaining 11 objects were inspected in HST and SDSS imaging, and in each case, we found justification for rejecting them from our sample. The reasons for rejection in each of these 11 individual cases are discussed in Section 2.2.1.4.

This means our sample contains all the known RSGs in M31 with  $\log(L/L_{\odot}) > 5$  from previous work as well as 48 candidates which we found through our own colour/magnitude criteria<sup>2</sup>

---

<sup>2</sup>It should be noted that when we calculated the luminosities using our SED method of all the stars from previous work, some had revised luminosities meaning that they no longer had luminosities greater than  $\log(L/L_{\odot}) > 5$ , hence our sample size greater than  $\log(L/L_{\odot}) > 5$  is smaller than in Gordon et al. (2016).

#### 2.2.1.4 Rejected stars from [Massey & Evans \(2016\)](#) and [Gordon et al. \(2016\)](#)

Below are the objects from previous M31 RSG catalogues which we have rejected from our study:

1. **J004105.97+403407.9, J004431.71+415629.1, J003942.43+403203.5 and J003811.56+402358.2:** These objects from GHJ16 have Gaia EDR3 proper motions which indicate they are foreground objects, deviating from M31's proper motion by  $\sim 3 - 4\sigma$ .
2. **J004303.21+410433.8 and J004052.19+403116.6:** These two objects are present in the GHJ16 sample but have assigned spectral types of B0.5I and B8, respectively, found in [Massey et al. \(2016\)](#).
3. **J004416.28+412106.6 and J004259.31+410629.1:** For the object J004416.28+412106.6, although described as an RSG candidate in GHJ16, both [Massey et al. \(2016\)](#) and [Azimlu et al. \(2011\)](#) classify this as an HII region. It also has a low B-V colour of 0.22 which corresponds to a spectral classification much earlier than K or M. Similarly for J004259.31+410629.1, this object has a low B-V colour of 0.70 which again suggests an early spectral type. Gaia EDR3 also shows J004259.31+410629.1 to have a huge proper motion ( $19.8 \text{ mas yr}^{-1}$ ), suggesting that it is not an M31 object. Additionally, [Soraisam et al. \(2020\)](#) discuss that not only is this object located within an HII region, it also shows characteristics of being W-Ursae-Majoris contact binary, with J004259.31+410629.1 being foreground.
4. **J003948.45+403131.5:** This object has a Gaia Bp-Rp colour of 0.73 which means it does not meet our red criteria. It is absent from the [Khan \(2017\)](#) mid-IR catalogue for M31 due to being spatially extended and has crowded LGGs photometry, which Gaia EDR3 is unable to resolve. It is described as a young cluster in [Caldwell et al. \(2009\)](#); [Kang et al. \(2012\)](#) and is therefore rejected from our sample.
5. **J004331.04+411815.9 and J004336.68+410811.8:** These two objects are both located in the halo of M31 and appear to be spatially extended in HST

PHAT images, which suggests that they are possibly globular clusters.

## 2.3 Discussion

### 2.3.1 Comparison to previous work

Our results show that the luminosities determined in the present work are on average lower compared to those found for the same stars in previous work, especially those at the high end of the luminosity function. In particular, for the stars J004539.99+415404.1, J004520.67+414717.3 and J004428.12+415502.9, [Massey & Evans \(2016\)](#) find  $\log(L/L_{\odot}) = 5.81, 5.81$  and  $5.64$ , respectively. These are  $0.32$  and  $0.06$  and  $0.11$ dex brighter than found in the present work. The same is seen when compared to [Gordon et al. \(2016\)](#), where they find  $\log(L/L_{\odot})$  of  $6.09, 5.94$  and  $5.89$ , which is  $0.60, 0.19$  and  $0.36$ dex brighter than this work. This is shown in [Figure 2.7](#), where there is both a systematic offset between the luminosity samples as well as object to object differences. Below we describe the differences between these studies in more detail.

#### 2.3.1.1 Comparison with [Massey & Evans \(2016\)](#) and [Neugent et al. \(2020\)](#)

Firstly, to correct for foreground visual extinction  $A_v$  in ME16, they adopt a uniform value of  $A_V = 1$  derived from their spectral fits to optical spectrophotometry of each RSG in their sample. Later work by [Neugent et al. \(2020\)](#), use the same approach but also introduce a brightness-dependent extinction component which causes the brightest RSGs to have extinctions proportional to their K-band brightnesses. This then has the effect of systematically shifting the brighter RSGs to higher luminosities and warmer temperatures, which leads to a higher  $L_{\max}$  of  $\log(L/L_{\odot}) \approx 5.7$ , compared to when adopting a uniform  $A_v = 1$ , which results in a reduced  $L_{\max}$  of approximately  $\log(L/L_{\odot}) \approx 5.5$ . Though [Massey et al. \(2021\)](#) comment that using this added extinction component leads to ‘much better agreement with the evolutionary tracks’ and than would have occurred by adopting a uniform  $A_v$ , our goal in the present work is to test these same evolutionary models. Therefore, for us to use these models to inform our choice of extinction correction would be circular logic on our part. Instead, we employ an independent method to estimate each star’s extinction, specifically, through the use of an M31 extinction map ([Dalcanton et al., 2015](#)) and adopting the median  $A_v = 1.19 \pm 0.10$  for those not covered by the map. Therefore, the extinctions we assign

to the brightest objects are inevitably lower than those adopted by [Neugent et al. \(2020\)](#).

To obtain bolometric fluxes, ME16 employ the  $T_{\text{eff}} - BC_K$  relation, derived from fitting MARCS model atmospheres to optical spectra from [Massey et al. \(2009\)](#). However, it is well known that these model atmospheres perform poorly at optical wavelengths, leading to systematic errors in  $T_{\text{eff}}$  and in  $BC_K$  (see [Davies et al., 2013](#)). Our method of estimating  $L_{\text{bol}}$  from integrating the SED is free of any such model dependencies.

Another factor which directly affects their luminosities is HST PHAT and Gaia EDR3 showing some of their most luminous RSGs resolving into multiple sources. In the present work, we have flagged that both J004539.99+415404.1 and J004428.12+415502.9 resolve into two objects, both with one source having a proper motion inconsistent with M31 and the other being a likely M31 member. When we account for the luminosity of the blended stars in these cases, it results in a downward revision of the our original SED derived  $L_{\text{bol}}$ .

We find our luminosities to be broadly consistent with those found from [Massey & Evans \(2016, hereafter, ME16\)](#), however there is a disagreement when it comes to the higher luminosity RSGs. We include comparisons with more recent work by [Neugent et al. \(2020\)](#), who also measure the RSG luminosity function in M31 and adopt a few of the same techniques as ME16 such as, extinction correction method and the use of a  $BC_K$  to determine bolometric luminosity. Here we discuss the possible reasons for differences in luminosity for these objects.

### 2.3.1.2 Comparison with [Gordon et al. \(2016\)](#)

The bolometric luminosities calculated for the RSG candidates in [Gordon et al. \(2016, hereafter, GHJ16\)](#) are on average 0.16dex higher than those found for the same stars in the present work. Figure 2.7 shows the systematic offset in luminosity between the two studies. In GHJ16, they adopt the same approach of integrating SEDs to obtain  $L_{\text{bol}}$ , although they only integrate from the optical to the near-IR K-band, unless there is evidence for circumstellar dust where they then integrate out to the  $22\mu\text{m}$  WISE band. However, the WISE mid-IR photometry has limited angular resolution, where the  $22\mu\text{m}$  waveband has a FWHM of  $12''$ , a factor of 2 coarser than MIPS, which can result in incorrect cross-identification of objects in different catalogues, as highlighted by GHJ16 themselves. An informative example of this is the source J004539.99+415404.1, which

appears in the GHJ16 catalogue as having  $\log(L/L_\odot) = 6.09$ . In their analysis, GHJ16 employ photometry from the ALLWISE catalogue across all four bands. However, inspection of the WISE images at  $12\mu\text{m}$  and  $22\mu\text{m}$  reveal that there is no point source at this position. Instead, at these wavelengths we see only the bright background emission of the underlying spiral arm which is incorrectly attributed to the RSG in the ALLWISE point-source catalogue. This phenomenon is responsible for GHJ16 overestimating the luminosities of many objects in their sample.

A second difference between the present work and GHJ16 is how extinction is accounted for. GHJ16 explore two separate methods: firstly, they estimate  $A_V$  from colours of nearby O and B type stars; and secondly, they derive  $A_V$  from the relation between neutral hydrogen column density and the colour excess  $E(B-V)$  along the line of sight to each RSG candidate. However, since a large fraction of their RSGs have no nearby OB stars, not all of their RSGs have  $A_V$  estimates from both methods, where  $\sim 67\%$  of their stars have HI-based  $A_V$  estimates only. In the circumstances where there is an extinction measurement available via both methods, the OB star method is favoured. However, this method often yields a much larger  $A_V$  compared to their alternate method. One example being, the RSG candidate J004304.62+410348.4, for which they find  $\log(L/L_\odot) = 5.40$  with  $A_V = 2.1$  from their OB colour method which they adopt, but they also find and  $A_V = 1.3$  from the neutral hydrogen column density method. Using these higher extinction values contribute to the higher luminosities for these stars.

### 2.3.2 Comparison to lower metallicity galaxies

To make a broader test of the metallicity dependence of  $L_{\text{max}}$  and the luminosity function, we perform two comparisons. Firstly, we compare the empirical luminosity functions of the LMC and SMC with M31. Secondly, we compare the M31 luminosity function and  $L_{\text{max}}$  to theoretical expectations of lower metallicities using population synthesis.

#### 2.3.2.1 Observational comparisons between the LMC and SMC

We look at the cumulative RSG luminosity function for M31 and compare with the empirical SMC and LMC distributions from DCB18, looking at all RSGs with  $\log(L/L_\odot) > 5$ , where our sample is considered to be complete. In these galaxies, the metallicities are thought to be  $\sim 0.25Z_\odot$  and  $0.5Z_\odot$ , respectively (Russell & Dopita, 1990). As noted

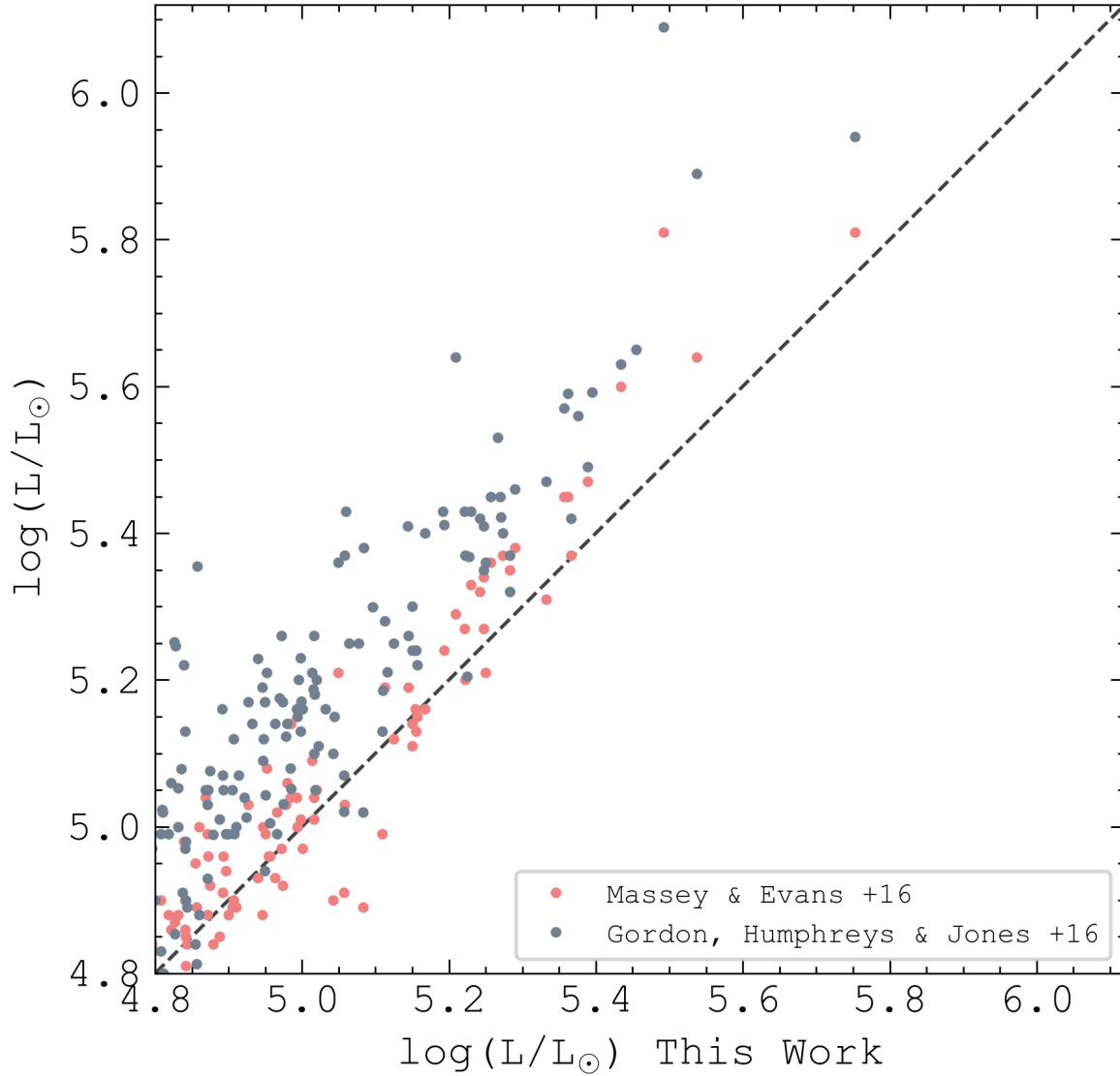


FIGURE 2.7: Comparison of bolometric luminosities found in the present work and previous studies of M31 RSGs. The grey points denote the luminosities from this work compared with [Gordon et al. \(2016\)](#) and pink points shows the comparisons of this work with the luminosities from [Massey & Evans \(2016\)](#). The black dashed line indicates the 1:1 line.

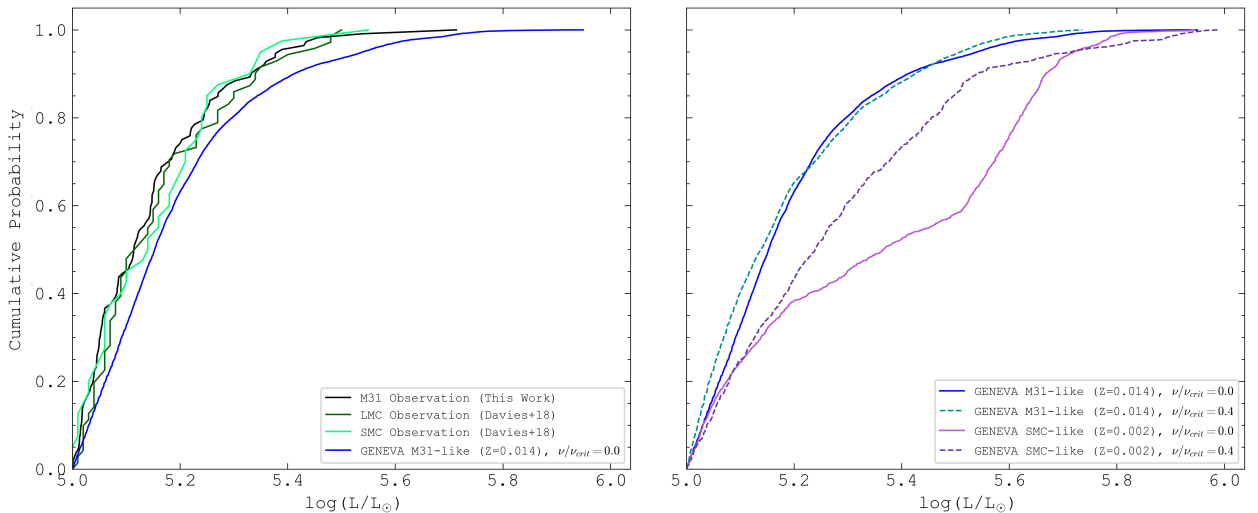


FIGURE 2.8: Left Panel: The cumulative luminosity distribution of all the Red Supergiants with an observational luminosity  $\log(L/L_{\odot}) > 5$  in M31 from this work, as well as for the Large and Small Magellanic Clouds from [Davies, Crowther & Beasor \(2018\)](#).

Right Panel: Cumulative luminosity distribution of the cool supergiants with a luminosity  $\log(L/L_{\odot}) > 5$  from the model luminosity functions predicted by GENEVA, at both solar (from [Ekström et al., 2012](#)) and SMC-like metallicities (from [Georgy et al., 2013b](#)) for both the rotating and non-rotating models. We include the ‘M31-like’ non-rotating model predicted distribution in the left panel for comparison.

previously, we assume that the M31 metallicity lies in the range of  $1.06 - 1.66Z_{\odot}$  determined by [Zurita & Bresolin \(2012\)](#) from direct temperature measurements from HII regions, where the stars present are also used to establish metallicity (e.g. [Venn et al. \(2000\)](#) and [Crowther \(2001\)](#)). The left panel of Figure 2.8 shows the similarities of the observed cumulative luminosity functions for M31, SMC and LMC. We perform a Kolmogorov-Smirnov (KS) test to evaluate these similarities by measuring the differences between the cumulative distribution functions. We find for the empirical M31 distribution compared with the SMC and LMC, a 60% and 44% probability, respectively, that they are drawn from the same parent distribution. Hence, the probability that the RSG luminosity function in the three galaxies are consistent with one another is within  $1\sigma$ . Furthermore, each galaxy has the same  $L_{\max}$  to within 0.1dex, at  $\log(L/L_{\odot}) \sim 5.5$ . Therefore, we find no evidence that the luminosities of RSGs have a dependence on metallicity. In the next section, we will compare these empirical findings to theoretical predictions.

### 2.3.3 Theoretical predictions of the luminosity distribution

To compare our observational results to theoretical predictions, we perform a population synthesis analysis. We do so by first generating a sample of random initial masses between  $8 - 60M_{\odot}$  according to the Salpeter initial mass function (IMF). Each star is randomly assigned an age between 0 and 38 Myr, under the implicit assumption of a constant star-formation rate. We then match these to evolutionary tracks using the SYnthetic CLusters Isochrones & Stellar Tracks (SYCLIST) from the Geneva group at solar metallicity ( $Z=0.014$ ) (Ekström et al., 2012), to interpolate  $L_{\text{bol}}$  and  $T_{\text{eff}}$  from the track of each simulated star, removing any stars with age greater than the stars maximum expected lifetime. We also apply a temperature cut at  $\log T_{\text{eff}} < 3.8$  to ensure the sample consists of cool supergiants. We perform a Monte Carlo experiment where we draw a random sample of stars from the model population, matching the observed number of RSGs in M31 and show the mean number of stars in each luminosity bin for both the rotating and non rotating models. The result is a simulated luminosity distribution for a constant star formation rate.

The comparison of this simulated distribution to the observations shows that the model predictions perhaps slightly over-predict the number of luminous stars at the high end of the distribution compared to observation for M31, but more notably, predicts  $L_{\text{max}}$  to be much higher than we observe. However, at the high luminosity end we do have a very small sample size and so our results are subject to stochastic uncertainties, which we will quantify in Section 2.3.3.1.

The right panel of Figure 2.8 shows the model cumulative RSG luminosity functions at M31-like metallicity for both the rotating and non-rotating models. It can be seen that although the shape of the M31 cumulative distributions are quite similar, there is a distinct difference in  $L_{\text{max}}$ , where the non-rotating models predict a higher maximum luminosity compared to the rotating models. When comparing to the observed M31 cumulative distribution in the left panel of Figure 2.8, there is a clear difference between the model and observed distributions.

When we take a look at the model cumulative luminosity function of RSGs at SMC-like ( $Z=0.002$ ) metallicity (SMC-like tracks are from Georgy et al. 2013b), seen in the right panel of Figure 2.8, there is not only a clear difference between the distributions of the rotating and non-rotating models, but a distinct contrast between the model M31 and

model SMC distributions. Therefore, the models predict that we should see a difference between the RSG luminosity functions of M31 and the SMC. However, despite the contrast in metallicity, the observed RSG cumulative distributions are consistent with each other to within  $1\sigma$ .

We now compare the observational and model predicted M31 and SMC-like cumulative distributions using a KS test, as in the previous section. Here we find a probability of 5% (rotating) and 0.1% (non-rotating) for the M31 models compared with observations and a 0.02% (rotating) and  $10^{-6}\%$  (non-rotating) probability for the SMC models compared with observations. These low probabilities lead us to conclude that there is little similarity between the model distributions in the two galaxies and they are unlikely to be drawn from the same parent distribution. This is in sharp contrast with what we see in the empirical distributions of M31 and the SMC, which are statistically indistinguishable.

From our observational study of the M31 RSG population, as previously discussed, after the marginal candidate J004520.67+414717.3 with  $\log(L/L_{\odot}) = 5.75 \pm 0.11$ , the next five most luminous stars span the range of  $5.43 < \log(L/L_{\odot}) < 5.53$ , suggesting an upper luminosity limit for M31 of  $\log(L/L_{\odot}) \approx 5.5$ . In this section, we take a closer look at the statistical significance of  $L_{\max}$  at M31 and SMC-like metallicities as predicted from the Geneva models.

By simply looking at the parameter space occupied by the evolutionary tracks on a HR diagram, the Geneva models predict that  $L_{\max}$  for M31 should be in the range  $5.7 \lesssim \log(L/L_{\odot}) \lesssim 5.8$ , yet we observe a much lower limit of  $\approx 5.5$ . However, we are dealing with small number statistics at the high luminosity end. This results in stochastic effects where the  $L_{\max}$  we observe is a function of our sample size, meaning the larger the sample size, the higher the probability of sampling close to the true HD limit. Therefore, when comparing model predictions to observations, we must be careful to take this effect into account.

To investigate the effects of sample size on  $L_{\max}$ , we perform another Monte Carlo experiment where we randomly select  $N$  stars from the theoretical luminosity function and determine  $L_{\max}$  of that sample. We repeat this  $10^5$  times to find the average  $L_{\max}$  for each sample size of  $N$  cool supergiants with  $\log(L/L_{\odot}) > 5$ . The results of this

Monte Carlo are shown in Figure 2.9 for both M31 and SMC-like metallicities. It shows the  $L_{\max}$  we would expect to measure, plus the confidence intervals of that value, as a function of sample size. As one would expect, larger sample sizes result in the higher luminosity bins being more populated, meaning that the  $L_{\max}$  we observe is more likely to reflect the ‘true’  $L_{\max}$ , with a smaller associated uncertainty.

In each panel of Figure 2.9, the empirical  $L_{\max}$  for the sample size we observe for that galaxy is denoted by the black star. Although M31 shows agreement within  $3\sigma$ , the SMC shows a disagreement beyond the 99.7% confidence limit. This increasing disagreement between observations and theoretical predictions as a function of metallicity can be understood as follows: As shown earlier, the empirical  $L_{\max}$  is observed to be metallicity-invariant. By contrast, the theoretical expectation of  $L_{\max}$  in single star evolution is governed by metallicity-dependent mass-loss, and so increases with decreasing  $Z$ .

In summary, we find no significant difference in  $L_{\max}$  within the errors across a metallicity baseline of  $(0.25Z_{\odot} \text{ to } \gtrsim Z_{\odot})$ . This is in clear disagreement with theoretical expectations because  $L_{\max}$  predictions from the models are simply too high compared to observational measurements and this effect is predicted to only increase with decreasing metallicity.

### 2.3.3.1 Comparisons to theoretical predictions of $L_{\max}$

From our observational study of the M31 RSG population, as previously discussed, after the marginal candidate J004520.67+414717.3 with  $\log(L/L_{\odot}) = 5.75 \pm 0.11$ , the next five most luminous stars span the range of  $5.43 < \log(L/L_{\odot}) < 5.53$ , suggesting an upper luminosity limit for M31 of  $\log(L/L_{\odot}) \approx 5.5$ . In this section, we take a closer look at the statistical significance of  $L_{\max}$  at M31 and SMC-like metallicities as predicted from the Geneva models.

By simply looking at the parameter space occupied by the evolutionary tracks on a HR diagram, the Geneva models predict that  $L_{\max}$  for M31 should be in the range  $5.7 \lesssim \log(L/L_{\odot}) \lesssim 5.8$ , yet we observe a much lower limit of  $\approx 5.5$ . However, we are dealing with small number statistics at the high luminosity end. This results in stochastic effects where the  $L_{\max}$  we observe is a function of our sample size, meaning

the larger the sample size, the higher the probability of sampling close to the true HD limit. Therefore, when comparing model predictions to observations, we must be careful to take this effect into account.

Next, the effects of sample size on  $L_{\max}$  is explored. With a sample size of 415 RSGs in M31, this is only a factor of  $\sim 2$  larger than the number of RSGs found in the SMC in [Davies, Crowther & Beasor \(2018\)](#). However, in [Rahman et al. \(2016\)](#), the star formation rate (SFR) of M31 is thought to be a factor 10 greater than in the SMC (i.e.  $SFR_{M31} = 0.4M_{\odot}yr^{-1}$  and  $SFR_{SMC} = 0.04M_{\odot}yr^{-1}$  ([Kennicutt et al., 2008](#))) so it could be naively assumed that we would expect to see a factor of 5 more RSGs in M31 than in the SMC. In actual fact, there are fewer RSGs in M31 due to a low RSG-to-WR star ratio at higher metallicities, resulting in fewer RSGs overall ([Massey et al., 2021](#)). To test for the effects of sample size, we perform another Monte Carlo experiment where we randomly select  $N$  stars from the theoretical luminosity function and determine  $L_{\max}$  of that sample. We repeat this  $10^5$  times to find the average  $L_{\max}$  for each sample size of  $N$  cool supergiants with  $\log(L/L_{\odot}) > 5$ . The results of this Monte Carlo are shown in [Figure 2.9](#) for both M31 and SMC-like metallicities. It shows the  $L_{\max}$  we would expect to measure, plus the confidence intervals of that value, as a function of sample size. As one would expect, larger sample sizes result in the higher luminosity bins being more populated, meaning that the  $L_{\max}$  we observe is more likely to reflect the ‘true’  $L_{\max}$ , with a smaller associated uncertainty.

In each panel of [Figure 2.9](#), the empirical  $L_{\max}$  for the sample size we observe for that galaxy is denoted by the black star. Although M31 shows agreement within  $3\sigma$ , the SMC shows a disagreement beyond the 99.7% confidence limit. This increasing disagreement between observations and theoretical predictions as a function of metallicity can be understood as follows: As shown earlier, the empirical  $L_{\max}$  is observed to be metallicity-invariant. By contrast, the theoretical expectation of  $L_{\max}$  in single star evolution is governed by metallicity-dependent mass-loss, and so increases with decreasing  $Z$ .

In summary, we find no significant difference in  $L_{\max}$  within the errors across a metallicity baseline of  $(0.25Z_{\odot} \text{ to } \gtrsim Z_{\odot})$ . This is in clear disagreement with theoretical expectations because  $L_{\max}$  predictions from the models are simply too high compared

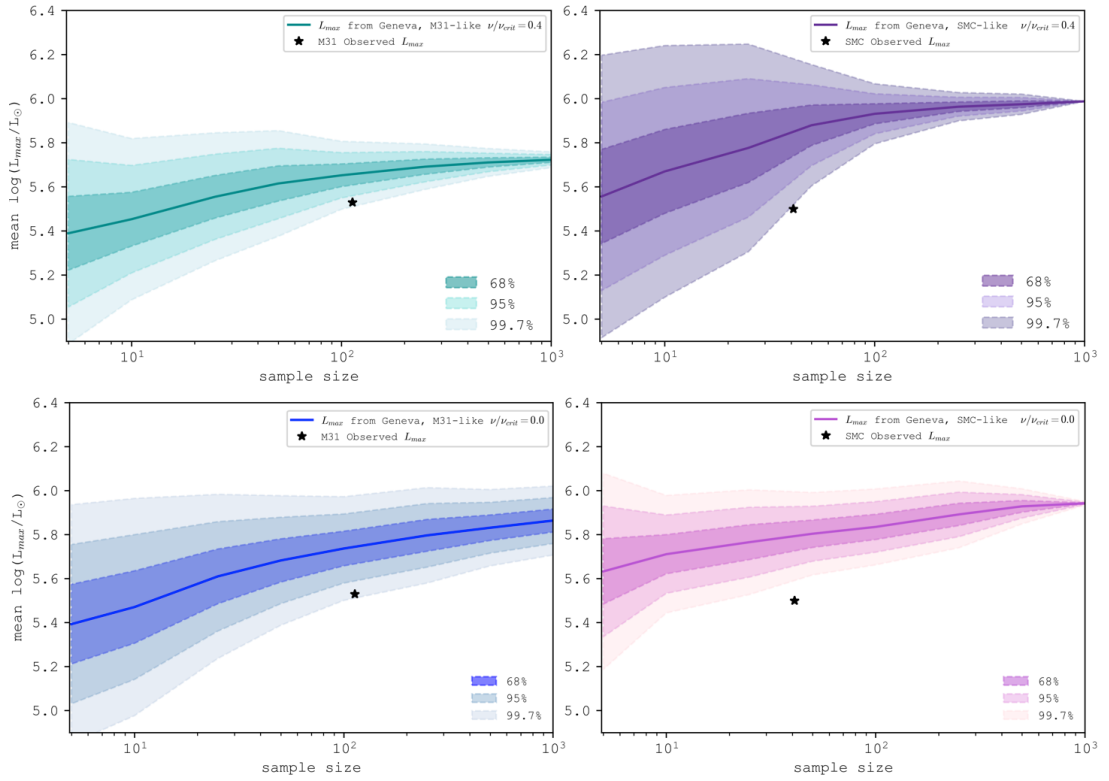


FIGURE 2.9: The expected  $L_{\max}$  for a range of sample sizes as predicted by the Geneva rotating models for both solar ( $Z=0.014$ ) and SMC-like ( $Z=0.002$ ) metallicities. The shaded regions indicate the confidence limits on  $L_{\max}$  as shown in the legend and the black stars indicate the observed  $L_{\max}$  and sample size for M31 from this work and the same for the SMC from [Davies, Crowther & Beasar \(2018\)](#).

to observational measurements and this effect is predicted to only increase with decreasing metallicity.

### 2.3.4 Possible explanations for a metallicity invariant HD limit

The results of this work have shown that the observational luminosity function of RSGs do not follow theoretical expectations, both in terms of  $L_{\max}$  and the shape of the luminosity function. There are several well-known sources of uncertainty in stellar evolutionary models, particularly in the pre-supernova phases of massive stars, such as mass-loss, mixing processes and rotational effects. In the present section, we discuss the possible implications these parameters may have for the theoretical predictions of the HD limit.

### Mass loss: Hot wind phase

Mass loss is a key process responsible for the stripping of the Hydrogen envelopes of stars. Hot star winds on the MS are driven by radiation pressure due to metal absorption lines in the UV, which means wind strength is sensitive to metallicity. It is this dependence of wind strength on metallicity which results in the predicted metallicity dependence of the HD limit in single star models. However, it has been seen from the cumulative luminosity functions of the RSGs in M31, LMC and SMC and from the invariance of  $L_{\max}$  across these galaxies that there is no metallicity dependence. Also, recent work has shown that the mass loss rates from these metallicity dependent hot star winds are being revised downward by a factor of  $\sim 3$  (e.g. [Sundqvist et al., 2019](#); [Björklund et al., 2021](#)), and so they are even less effective at removing the Hydrogen envelope than previously thought. Therefore, we conclude that line-driven winds in the hot star phases can **not** be the cause of the HD limit.

### Mass loss: RSG phase

We next take a look at the contribution of mass loss as a result of RSG winds, for which there is some evidence to suggest that more metal poor environments result in weakened RSG wind speeds (e.g. [Goldman et al., 2017](#)). The most widely used RSG wind prescription in stellar evolutionary codes is from [de Jager et al. \(1988\)](#), but is thought to over-estimate the rate of mass loss ( $\dot{M}$ ), particularly for more luminous RSGs, as discussed in [Beasor et al. \(2020\)](#). A new RSG  $\dot{M}$  prescription, presented in the latter study, implies that only a small fraction of envelope mass is lost during the RSG phase ( $\sim 1M_{\odot}$ ). This is considerably lower than with the prescription implemented in the Geneva models, in which up to  $\sim 50\%$  of the envelope mass can be lost during this period. In fact, with the [Beasor et al. \(2020\)](#) mass loss recipe implemented instead, higher mass stars ( $> 30M_{\odot}$ ) no longer evolve back to the bluer side of the HR diagram, resulting in a larger number of higher mass stars remaining in the RSG phase. Therefore, despite offering a more accurate description of  $\dot{M}$  for cool supergiants in stellar models, in regards to the HD limit the disagreement actually worsens, giving rise to an even greater upper limit of  $\log(L/L_{\odot}) \sim 6$ . This means that RSG winds are simply not strong enough to be responsible for the HD limit.

The lack of metallicity dependence means that line-driven winds cannot be responsible for the HD limit. However, this doesn't rule out the episodic type mass loss seen in Luminous Blue Variables (LBVs). LBV eruptive mass loss is so strong that the winds become optically thick and are likely to be driven by continuum radiation pressure in

super-Eddington phases (Smith, 2006). Since we observe LBV eruptions at high and low metallicity, LBV mass loss is not metallicity dependent (Smith & Owocki, 2006). This means we cannot rule out mass loss from LBV type eruptions as a potential cause of the HD limit. Similarly, Kraus et al. (2015) suggest that stars in the B[e] supergiant phase, are also thought to eject large amounts of material, much like LBVs which could be another possible type of mass loss contributing to the HD limit.

Further, it has been argued that the origin of LBV-type eruptions could be a consequence of binary interaction and mergers (e.g. Smith, 2014), which could also be an explanation for the existence of the HD limit (see next section).

### **Binarity**

Thus far, in seeking to understand the RSG populations across the three galaxies, we have exclusively considered single-star evolutionary models. However, it is becoming increasingly clear that such models are of limited relevance for the most massive stars. Several studies in the literature have concluded that the fraction of OB stars in binary systems are in the range of 50-60% or higher (Sana et al., 2012, 2013; Dunstall et al., 2015). Furthermore, the probability of a star being in a multiple, *and* that the star will interact with this companion, appears to increase with increasing mass (Duchêne & Kraus, 2013; Moe & Di Stefano, 2017). This is also suggested in the recent work of Bodensteiner et al. (2021), who find that the bias-corrected close binary fraction of the  $\sim 40$  Myr old massive SMC open cluster, NGC330, is  $34_{-7}^{+8}\%$ . This is a lower fraction compared to younger clusters in the Milky Way and LMC. For example, the Cygnus OB2 association within our Galaxy has an intrinsic binary fraction of  $\approx 55\%$  (Kobulnicky et al., 2014). The counterpart fraction for the overall B-star population of the LMC 30 Doradus region is found to be  $58 \pm 11\%$  (Dunstall et al., 2015). This means that above some mass threshold, it is reasonable to expect that the likelihood of a star evolving according to single stellar evolutionary tracks will eventually tend towards zero. Specifically, a star's evolution to the red will be prevented by interaction with a companion either in or before the Hertzsprung Gap. This means we would expect binary effects to also be contributing to the mass lost during a star's life and is therefore a possible explanation for the reduced  $L_{\max}$  we see in observations (Davies, Crowther & Beasor, 2018).

To investigate the effects of binarity on  $L_{\max}$ , we extracted the RSG luminosity function for a constant star formation history from the Binary Population and Spectral Synthesis (BPASS) models. These models assume the mass ratio and period distributions

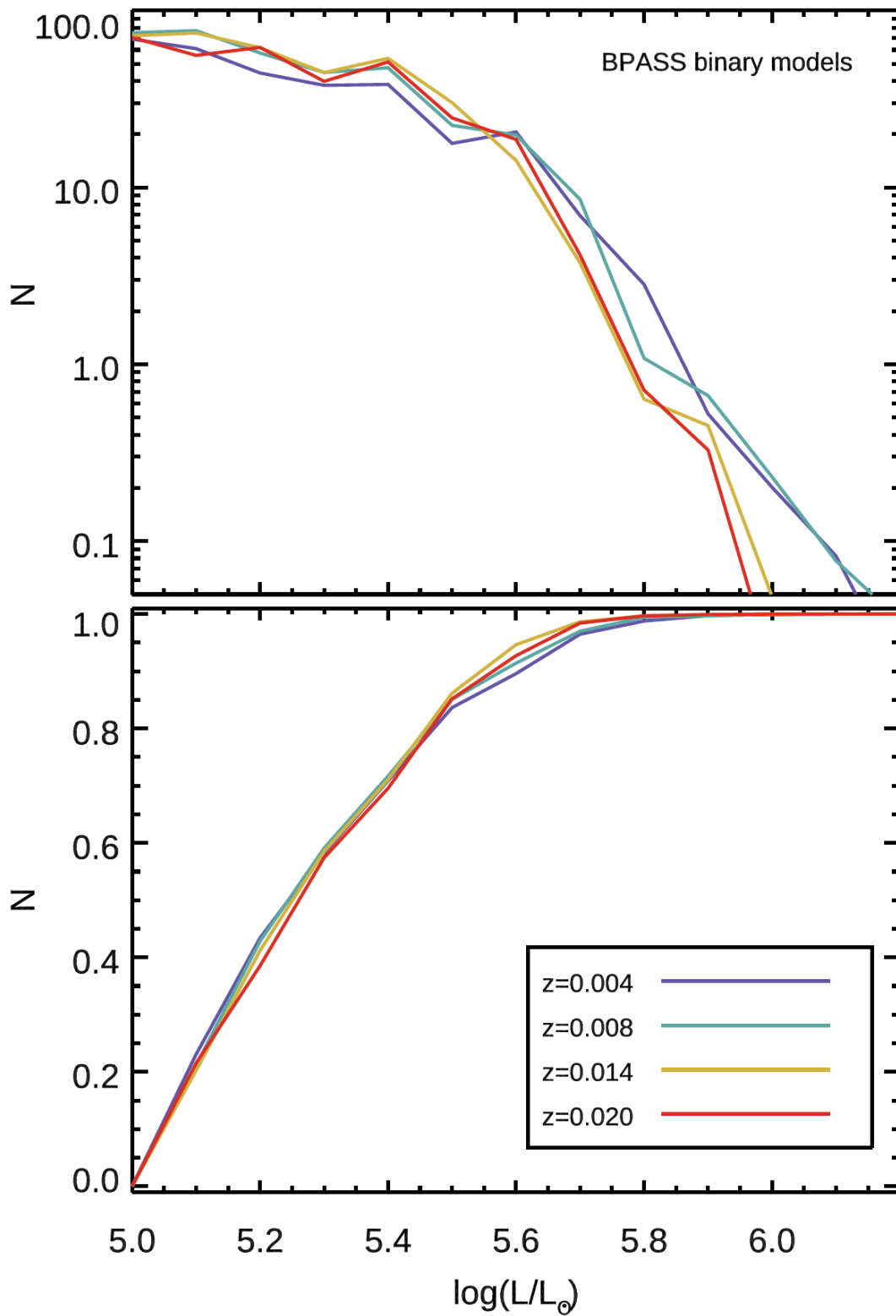


FIGURE 2.10: Top panel: Predictions of the luminosity function of cool supergiants from BPASS binary population synthesis for the metallicity range  $Z=0.004$  to  $Z=0.020$ . Bottom panel: The same result but shown as a cumulative luminosity distribution.

from Moe & Di Stefano (2017), which specify that stars with masses relevant for RSGs ( $M > 9 M_{\text{sun}}$ ) have close binary frequencies in excess of 80%. The BPASS RSG luminosity functions as a function of  $Z$  are shown in Figure 2.10. We still see a metallicity dependence and very high  $L_{\text{max}}$ , similar to single star models, in the metallicity range  $Z=0.004$  to  $Z=0.020$ .

Given the very high close binary fraction for massive stars set within the BPASS simulations, one would expect that most, if not all, of these stars would interact prior to the primary reaching the RSG phase. It is therefore intriguing that the BPASS-simulated RSG luminosity functions behave so similarly to those of the single star evolution models. In the future, it would be of interest to further mine the BPASS results to investigate the histories of the RSGs in these simulations.

## 2.4 Summary

In this work investigating the HD-limit of M31, we find the luminosity function of RSGs is independent of metallicity, based on the range of metallicities studied here (from SMC-like to M31-like). We find the HD limit to be  $\log(L_{\text{max}}/L_{\odot}) = 5.53 \pm 0.03$  in M31 ( $Z \gtrsim Z_{\odot}$ ), consistent with the limit found for both the LMC ( $Z \sim 0.5 Z_{\odot}$ ) and SMC ( $Z \sim 0.25 Z_{\odot}$ ), while the RSG luminosity distributions in these 3 galaxies are consistent to within  $1\sigma$ . We therefore find no evidence for a metallicity dependence on both the HD limit and the RSG luminosity function, and conclude that line-driven winds on the main sequence are not the cause of the HD limit. Also population synthesis analysis shows that the single star Geneva evolutionary models not only over-predict the number of luminous cool supergiants at the high luminosity end, but also over-predict  $L_{\text{max}}$ , particularly at lower metallicities.

## Chapter 3

# A mass-loss survey of M31 Red Supergiants

Insights into the mass-loss rates ( $\dot{M}$ ) of red supergiants (RSGs) are crucial for understanding stellar evolution, where the amount of mass lost from the Hydrogen envelope influences not only how the star evolves across the Hertzsprung-Russell (HR) diagram, but also the classification of the subsequent supernova. Studies in the literature show the evolutionary effects of changing the mass-loss rate of RSGs in stellar models, for example in [Meynet et al. \(2015\)](#), they find that in general, increased mass-loss rates of RSGs results in a reduced number of RSGs observed, due to the decreased RSG lifetimes. With the mass-loss rate increased by one order of magnitude, RSGs manifest at a later time time (8Myrs) compared to standard mass-loss rates (4Myrs). Additionally, this means the upper mass limit of stars which go on to spend time in the RSG stage is reduced. In [Beasor et al. \(2020\)](#), where  $\dot{M}$  is decreased compared to previous studies, higher mass stars ( $> 30M_{\odot}$ ) no longer evolve back to the bluer side of the HR diagram, resulting in a larger number of higher mass stars remaining in the RSG phase. This results in an inflated HD-limit of  $\log(L/L_{\odot}) \sim 6$ . This means that both the HD limit and luminosities of type II-P progenitors are extremely sensitive to changes in  $\dot{M}$  during the RSG phase.

It is still unclear what the driving mechanism governing RSG mass-loss is, which means  $\dot{M}$  cannot be derived from first principles, thus making predicting  $\dot{M}$  is challenging. However, a number of empirical prescriptions have been presented in the literature, which aim to correlate  $\dot{M}$  as a function of fundamental stellar parameters such as mass,

$L_{\text{bol}}$  and  $T_{\text{eff}}$  which can be incorporated into stellar evolution models. The most widely used prescription is by [de Jager et al. \(1988\)](#) (revised in [Nieuwenhuijzen & de Jager \(1990\)](#)), which was established using a study of 271 primarily population I galactic stars with spectral types from O to M. Their mass-loss rates were taken from various studies in the literature with the average  $\dot{M}$  determined and represented by one empirical formula with 2 parameters; effective temperature ( $T_{\text{eff}}$ ) and luminosity ( $L_{\text{bol}}$ ). The study then provides a regression to the data, fitting  $\dot{M}$  as a function of  $L_{\text{bol}}$  and  $T_{\text{eff}}$ . Since  $T_{\text{eff}}$  is approximately the same for all RSGs, it is essentially a 1D fit between  $\dot{M}$  and  $L_{\text{bol}}$ . However, each spectral class only has a small sample of stars (e.g. only 15 RSGs), which are biased towards luminous objects with high mass-loss rates as well as the sample being highly heterogeneous in their properties (luminosity, initial mass, metallicity etc). To sum up, since varied methods are adopted in determining  $\dot{M}$  from a number of different studies in the literature, plus the uncertain and outdated distance measurements used which lead to an incorrect luminosity, there is resulting substantial internal scatter ( $\pm 0.5\text{dex}$ ) on the mass-loss measurements (see [Maun & Josselin, 2011](#)). This margin of error leaves the problem entirely unconstrained with the cumulative mass lost in the RSG phase ranging from losing its entire H-envelope or none of it at all ([Beasor et al., 2020](#)). Such a considerable variation has substantial implications for the star's evolutionary path and the classification of the resulting supernova. Other prescriptions use varied techniques such as modelling stars' SEDs using radiative transfer code and using maser emitting objects to estimate  $\dot{M}$  (see, [van Loon et al., 2005](#); [Goldman et al., 2017](#)), but these methods are again biased towards higher  $\dot{M}$  RSGs. More recent prescriptions (e.g. [Björklund et al., 2021](#)) have seen a downward revision in the mass-loss rate on the main sequence as well as in the RSG phase in [Beasor et al. \(2020\)](#). The latter shows that quiescent mass-loss during the RSG phase is not effective at removing a significant fraction of the Hydrogen envelope, prior to core-collapse.

If quiescent mass-loss is not effective enough to solely remove a considerable amount of a star's envelope, then this places extra emphasis on potential short-lived high  $\dot{M}$  phases, such as those experienced by Luminous Blue Variables (LBVs) which have been suggested to remove several solar masses of material in extremely short periods of time. RSGs such as VY CMa and VX Sgr have seemingly high mass-loss rates, are thought to possibly represent this very fast stage of evolution defined by a high mass-loss rate, often referred to as a 'super-wind' phase ([Humphreys & Lockwood, 1972](#)). This phase would be too short to be captured by the [Beasor et al. \(2020\)](#) study, so a larger homogeneous sample would provide the best chance at finding any stars in this phase. In a study

by [van Loon et al. \(2005\)](#), they use a sample of ‘dust-enshrouded’ RSGs in the LMC and determine their mass-loss rates. These stars have sufficiently dense CSM which has the potential to obscure the star at optical wavelengths. To determine mass-loss, they modelled the stars’ spectral energy distributions finding relatively high  $\dot{M}$  which would place a fraction of their sample in the ‘super-wind’ phase ( $> 10^{-4} (M_{\odot}/yr)$ ). However, the focus on dusty stars means the [van Loon et al. \(2005\)](#) sample is heavily biased towards stars with high  $\dot{M}$ . M31 is a promising test-bed for finding an unbiased sample that catches RSGs in all  $\dot{M}$  phases, even the very brief ones such as the super-wind phase, so we can ascertain in which phase most of the mass is lost.

We investigate the mass-loss rates of RSGs at high metallicity, using our mid-IR selected sample of candidate RSGs in M31 and determine  $\dot{M}$  by fitting DUSTY models to their observed near and mid-IR photometry. If a high  $\dot{M}$  phase exists, with our large sample size we will be able to quantify both the duration of this phase as well as the total envelope mass the star could be capable of losing during such outbursts.

### 3.1 Method

#### 3.2 DUSTY: Radiative transfer code

For this work, we use the DUSTY radiative transfer code ([Ivezic et al., 1999](#)) to model the dust surrounding the RSGs in our sample. RSGs have cool, slow winds which can condense to dust relatively close to the star. This dust can absorb and re-emit radiation, for which DUSTY can then solve the radiative transfer equation. DUSTY models the distribution and properties of dust around a central source. It emulates the interaction between the stellar radiation and the surrounding dust grains, taking into account the absorption, scattering, and thermal emission processes. It makes a few assumptions such as, the dust distribution around the star being spherically symmetric. This simplifies the radiative transfer equations as they can be solved in 1D. Certain input parameters are required to be set in DUSTY, and the appearance of the output spectra is sensitive to these parameters chosen. DUSTY allows a grain size distribution to be specified as well as a mixture of different dust types. After defining the dust density profile, it determines the temperature of the dust from radiative equilibrium. Once  $\rho_0$  and the inner dust temperature  $T_{inner}$  as a function of radius,  $r$ , is obtained, we determine the opacity,  $\kappa(\lambda, r)$ , and then optical depth,  $\tau(\lambda, r)$ . Further, when assuming thermal equilibrium, the source function is  $S = B(\lambda, T)$ , where  $B(\lambda, T)$  is the Planck function. Finally, with  $\tau$  and  $B$  established, the radiative transfer equation can be solved to determine

the emergent flux as a function of  $\lambda$ .

In this chapter, we complement the study of [Beasor & Davies \(2016\)](#), for both selecting the model input parameters and the fitting methodology, which are each described in more detail below:

### 3.2.1 Model parameters

#### Input SED:

To begin, we used an input spectral energy distribution (SED) which will be reprocessed by the surrounding dust shell. We took a MARCS model atmosphere ([Gustafsson et al., 2008](#)), and a spectrum was generated using TURBOSPECTRUM ([Plez, 2012](#)). The parameters set for these models were representative of RSGs, i.e. micro-turbulent velocity  $4\text{km s}^{-1}$  and  $\log(g)=0$  ([Beasor & Davies, 2016](#)), although these have little effect on the resulting SED morphology due to the small temperature differential and all spectral variation is in optical wavelengths, which we are not fitting to. RSGs typically have effective temperatures of 3500–4100K, so we selected an  $T_{\text{eff}}$  reflective of this. Based on the RSG temperatures from [Patrick et al. \(2016\)](#), which find an average  $T_{\text{eff}}$  of  $3850 \pm 85$  based on a sample of 14 RSGs in NGC2100, we opt for a fiducial temperature effective temperature ( $T_{\text{eff}}$ ) for our input SED of 3900K in the present work. For completeness, in [Beasor & Davies \(2016\)](#), they investigated the sensitivity of the SED temperature and the affect this has on the resulting  $\dot{M}$  by comparing SEDs with varying temperatures spanning the range of typical RSGs, for which they found that the difference in was essentially negligible, with uncertainties  $< 10\%$ .

#### Dust grains:

Next, we selected the composition of the dust grains used in our models, which we chose to be of O-rich silicate dust. Excess Oxygen (compared to Carbon) results in O-rich dust which is observed in RSGs which exhibit mid-IR spectral features which arise at 9.7 and  $18\mu\text{m}$ , due to the presence of silicates ([Draine & Lee, 1984](#); [Buchanan et al., 2006](#)). This dictates the extinction efficiency ( $Q_{\lambda}$ ) which describes how the spherical dust shell will affect the propagating radiation and modify the input SED.

Alongside the dust composition, the dust grain size also needs to be specified in DUSTY. Similar studies in the literature which use radiative transfer models, the size of the dust grains used varies. For example, [van Loon et al. \(2005\)](#) use a constant grain size of

0.1 $\mu\text{m}$ , with dustier RSGs modelled with a smaller size of 0.06 $\mu\text{m}$ . In [Groenewegen et al. \(2009\)](#), they explored the impact grain size has on the output spectrum, finding that for O-rich LMC and SMC RSGs, a grain size of 1 $\mu\text{m}$  was a good fit to the observations. In [Scicluna et al. \(2015\)](#), for the RSG VY Canis Majoris, a constant grain size of 0.5 $\mu\text{m}$  is used, and similarly in [Smith et al. \(2001\)](#) for VY Canis Majoris, find the optimal grain size to be between 0.3 $\mu\text{m}$  and 1 $\mu\text{m}$ . With this considered, [Beasor & Davies \(2016\)](#) created models with a MRN power law and constant grain sizes of 0.1, 0.2, 0.3, 0.4 and 0.5 $\mu\text{m}$  to assess the effects of varying the grain size distribution has on  $\dot{M}$ , finally opting for a fiducial value of 0.3 $\mu\text{m}$ . They also conclude that increasing grain size has no effect on their derived  $\dot{M}$  values in addition to seemingly having no effect on  $A_v$ . Also, as discussed in [Beasor & Davies \(2016\)](#), since we are analysing stars' emission at wavelengths larger than the grain size, the efficiencies of scattering and absorption of dust is mostly independent of the grain size. For the work in this chapter, we also specify our grain size to be 0.3 $\mu\text{m}$  as well as a grain bulk density of  $3\text{gcm}^{-3}$ .

### Density distribution:

We provided DUSTY with a density distribution of  $r^{-2}$  assuming spherical symmetry. We also assume a steady state wind with outflow velocity ( $v_\infty$ ) of  $25 \pm 5\text{kms}^{-1}$  since we do not know the values for the RSGs in our sample. This is derived from previous outflow estimates (e.g. [van Loon et al., 2001](#); [Goldman et al., 2017](#)) who used maser emission to map the dust shells of other RSGs, finding  $v_\infty$  values consistent with  $\sim 20 - 30\text{kms}^{-1}$  for their sample of stars. This means that although we do not measure  $v_\infty$ , we can use a fiducial value and be confident that it introduces errors of no more than  $\pm 20\%$  into our  $\dot{M}$  estimates. Additionally, the shell is assumed to extend to  $10^4 \times$  its inner radius, where the outskirts of the shell are of a low enough density to have any effect on the spectrum.  $T_{inner}$  describes the temperature of this shell, for which we allow for a range between 300K-1200K increasing in steps of 100K. although this parameter is unconstrained so we kept it as a free parameter until we fit the data, see below in section 3.2.2. A maximum temperature of 1200K is chosen as it represents the commonly adopted silicate dust sublimation temperature, which is thought to be between 1000-1200K ([Schutte & Tielens, 1989](#); [van Loon et al., 2005](#)). Similarly for  $\tau_{nu}$ , which determines the dust shell mass, we set a range between 0.05 - 5.0 which again is a free parameter until the fit to the data is optimised. In comparison, [Shenoy et al. \(2016\)](#) who studied the mass-loss rates and cool dusty surrounding VY Canis Majoris and  $\mu$  Cep. They implemented a fixed  $T_{inner}$  of 1000K and a density distribution of  $\rho_r \propto r^{-q}$ , within the shell. They tested various optical depths with a range of exponents

$q \leq 2$  finding  $q=2$  failed to produce substantial dust to reproduce what is observed at the mid-IR end of the observed SED, and alternatively suggest that  $q=1.8$  was more suitable. This resulted in a mass-loss rate that is decreasing with time, due to increased dust at large radii than compared to a fixed  $\dot{M}$ . However, varying  $T_{inner}$  instead of fixing it at the sublimation temperature could also lead to a good fit, whilst using a  $q=2$  component, which would result in sufficient dust at large radii. In [Beasor & Davies \(2016\)](#), this is demonstrated using  $\mu$  Cep as an example, by creating a model and using the [Shenoy et al. \(2016\)](#) best fit parameters and density distribution, using a  $q=2$  density law leaving  $T_{inner}$  to be varied. They found that a model with  $T_{inner}=600\text{K}$  was a good fit to the [Shenoy et al. \(2016\)](#) model at wavelengths  $\leq 70\mu\text{m}$ . Therefore, for the work in this thesis, we will use a varied  $T_{inner}$  with  $q=2$  exponent.

### Gas to dust ratio:

For the gas-to-dust ratio ( $r_{gd}$ ), a vast number of observations of RSG winds suggest that  $r_{gd}$  is in the range of 100-500. It is assumed to scale with metallicity ([Marshall et al., 2004](#)), so for more metal rich galaxies like the Milky Way  $r_{gd}$  is 1:200, where as for more metal poor galaxies like the LMC and SMC,  $r_{gd}$  is 1:500 and 1:1000, respectively. In [van Loon \(2000\)](#), for obscured AGB and carbon stars a metallicity scaling of 1:200 is assumed. But some Milky Way RSGs suggest  $r_{gd}$  to be between 1:200-1000 for Betelgeuse ([Cannon et al., 2023](#); [De Beck et al., 2010](#)). In the present work, assuming that a more metal rich galaxy, i.e. M31, will be dustier,  $r_{gd}=1:200$  was assumed.

### 3.2.2 Fitting Methodology

Once the parameters are specified, we have a grid of dust shell models with set ranges for  $T_{inner}$  and  $\tau_v$ , which we used to fit a model spectrum for each of our RSGs. We created then synthetic photometric points to match our observed photometry for each RSG in the range of  $0.8\mu\text{m} > 24\mu\text{m}$  by convolving the model spectrum with the filter profiles of 2MASS (JHK) and *Spitzer* (IRAC/MIPS) (optical photometry is omitted from the fit due to the model SEDs being unable to simultaneously fit both optical the and near/mid-IR photometry. Since optical wavelengths do not provide much insight into mass loss behaviour of RSGs compared to longer wavelengths it was omitted). We then found the weighted mean of each synthetic photometric point to find the offset between synthetic and observed photometry, finding the optimum normalisation of each model. This is determined by the luminosity of the star, for which we use our values

determined in Chapter 2. We then used a  $\chi^2$  minimisation to identify the best fitting model spectrum to each RSG, where the smallest  $\chi^2$  corresponds to the best fit model.

$$\chi^2 = \sum \frac{(O_i - E_i)^2}{\sigma_i^2} \quad (3.1)$$

*Equation 3.2.2: Here  $i$  is the filter,  $O$  denotes the observed photometry,  $E$  represents the model photometry and  $\sigma^2$  is the associated uncertainty.*

### 3.2.3 Calculating $\dot{M}$

Mass-loss is derived using  $\tau_v$ , mass-density ( $\rho_0 = \frac{4}{3} \frac{\tau_v \rho_0 a}{Q_\lambda R_{in}}$ ) and the mass continuity equation ( $\dot{M} = 4\pi r^2 \rho(r) v_{inf}$ ), (method shown in [Beasor & Davies \(2016\)](#)) which results in the following equation:

$$\dot{M} = \frac{16\pi}{3} \frac{R_{in} \tau_\lambda \rho_d a v_\infty}{Q_\lambda} r_{gd} \quad (3.2)$$

*Equation 3.2.3: where  $R_{in}$  is the inner dust radius,  $\tau_v$  is the optical depth at  $0.55\mu\text{m}$ ,  $\rho_d$  is the grain bulk density,  $a$  is the grain size,  $v_\infty$  is the outflow velocity,  $r_{gd}$  is the gas-to-dust ratio and  $Q_\lambda$  is the extinction efficiency.*

The  $R_{in}$  value used is scaled in proportion to  $L_{bol}^{0.5}$ , where  $L_{bol}$  is the bolometric luminosity of the RSG, so we apply a scale factor of  $10_{L_{bol}}/10^4$  to our fiducial  $\dot{M}$ . The highest  $\dot{M}$  candidates can be seen in table 3.1.

## 3.3 Results

### 3.3.1 Modelling results

We ran our DUSTY fitting procedure for 387 M31 RSG candidates providing a mass-loss rate and best fit model for each RSG. Figure 3.1 shows the output spectrum from DUSTY for the RSG 00473111+4227488. The best fitting model spectrum for the observed photometry for this object identified by DUSTY was 400K with  $\tau = 0.05$ . DUSTY also outputs the attenuated flux, dust emission flux and scattered flux spectra, which can also be seen in Figure 3.1. The amount of attenuated flux is the total flux which reaches an observer after the absorption and scattering processes caused by the presence of dust grains surrounding the RSG, shown by the green dashed line. The dust

2MASS name	$\dot{M}(M_{\odot}\text{yr}^{-1})$	$\log(L/L_{\odot})$	$T_{inner}$ (K)	$\tau_{nu}$
00433528+4109595	1.21E-04	5.11±0.03	300K	3.0
00415905+4057186	1.06E-04	4.99±0.02	300	3.0
00445995+4128361	8.88E-05	4.84±0.03	300	3.0
00445934+4132266	7.89E-05	4.73±0.05	300	3.0
00451138+4137176	4.82E-05	5.13±0.02	500	3.0
00445852+4132290	4.41E-05	4.78±0.05	300	1.7
00441058+4131593	3.65E-05	4.89±0.04	500	3.0
00412201+4049413	3.60E-05	4.87±0.03	500	3.0
00434686+4112451	3.54E-05	5.04±0.02	500	2.5
00451173+4135310	3.29E-05	4.85±0.05	400	2.0

TABLE 3.1: Results for the 10 highest  $\dot{M}$  RSGs in M31, with their 2MASS designation, luminosity and best model fit  $\tau_{nu}$  and  $T_{inner}$ .

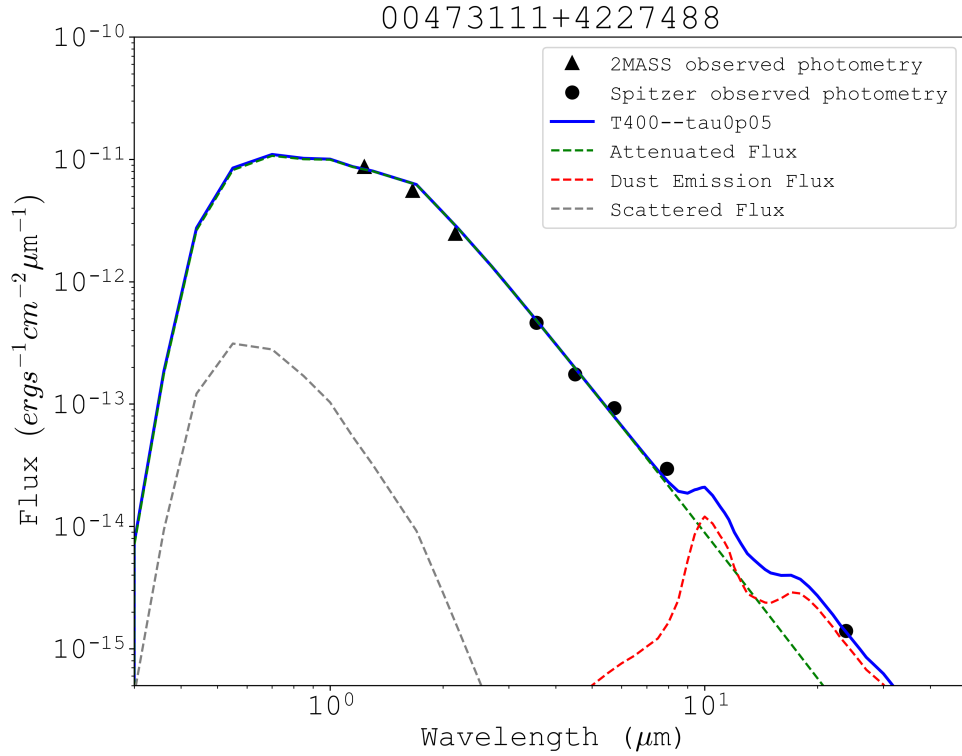


FIGURE 3.1: An example spectral energy distribution showing the observed photometry fitted to the best fit model spectrum (the blue line). The green line shows the attenuated flux, the red line shows the dust emission flux and the grey line shows the scattered flux.

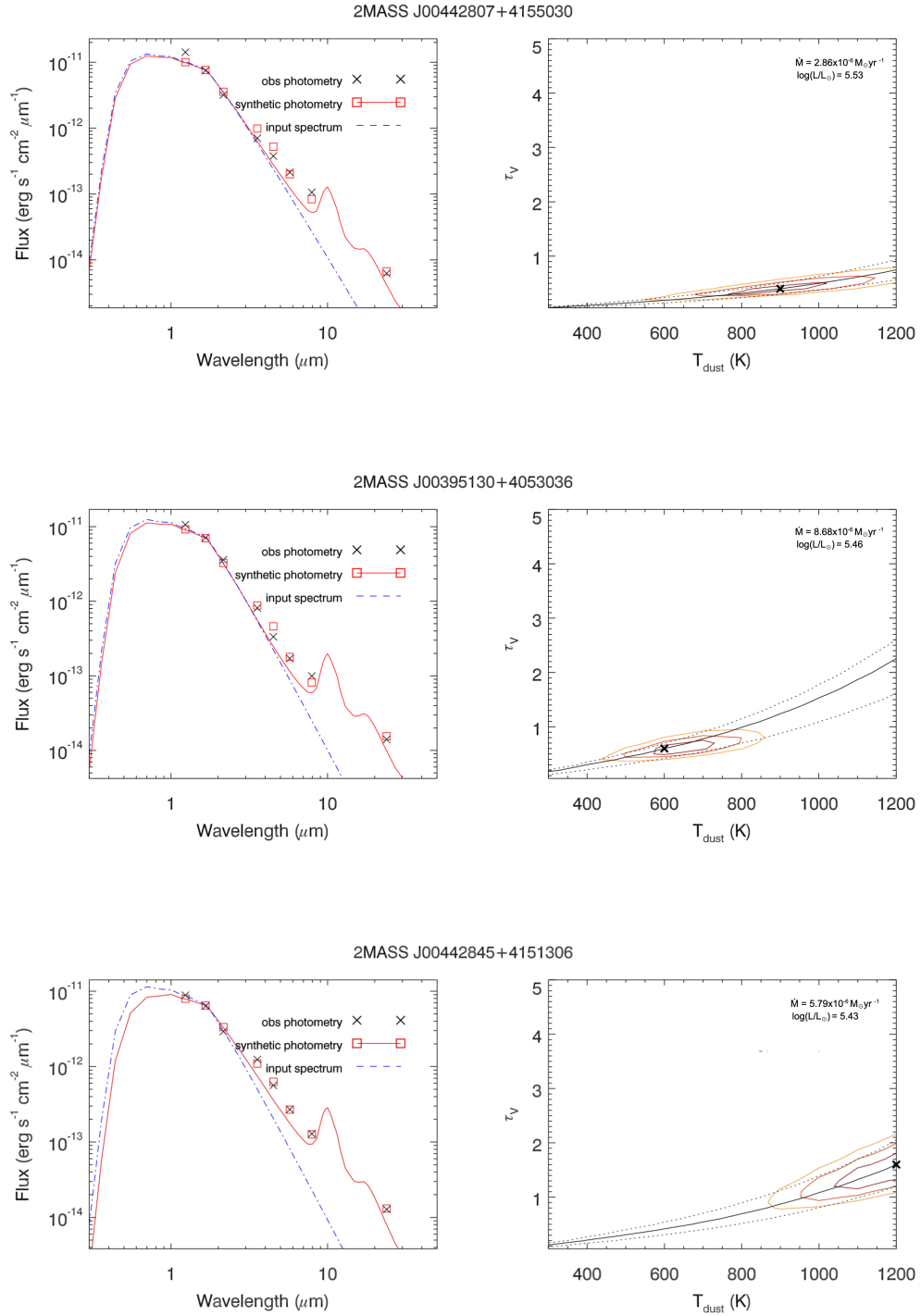


FIGURE 3.2: SED and contour for best fit model on a  $T_{inner} - \tau$  plane with the upper and lower  $\dot{M}$  contours overlapped on the right.

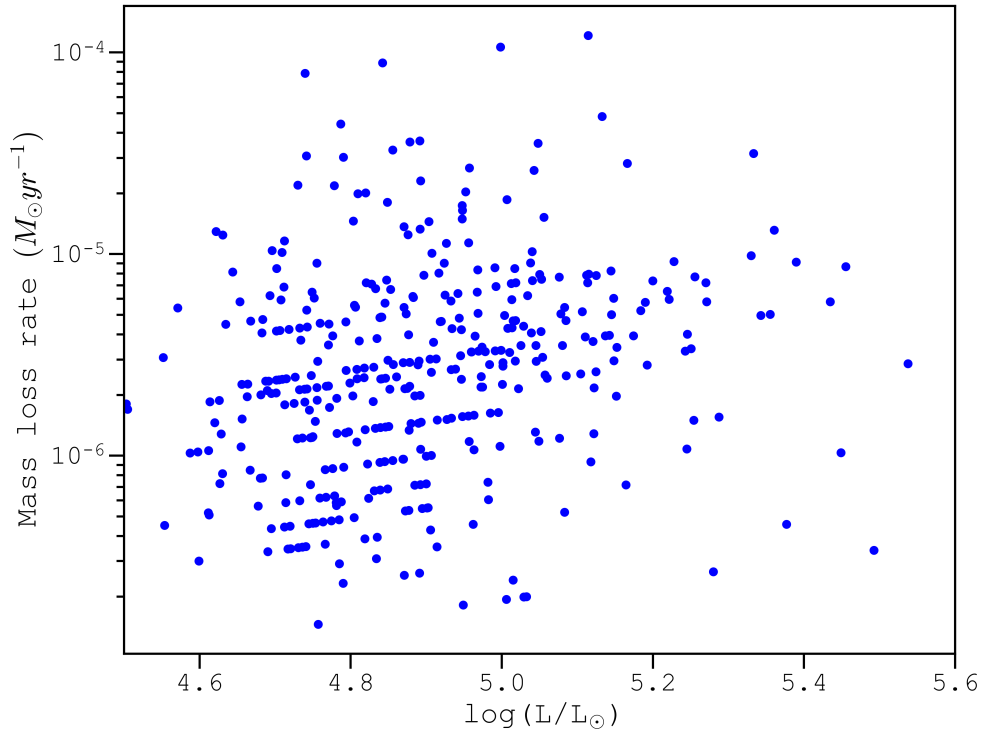


FIGURE 3.3: Plot showing mass-loss rate as a function of bolometric luminosity for the sample of M31 RSGs.

emission flux, described by the red dashed line, relates to the contribution of the dust to the overall observed flux from radiation emitted from the heated dust grains after absorbing photons directly from the RSG. The dust grains re-emit the absorbed energy as thermal radiation in the mid-IR. The grey dashed scattered flux lines represents the radiation that has changed direction due to scattering by the dust grains and can be observed at different wavelengths depending on the scattering properties of the dust. In RSGs, the re-emitted flux usually manifests as a characteristic bump at  $\sim 10\mu\text{m}$ , which is indicative of a large amount of circumstellar material present. Figure 3.2 then shows a further 3 example stars with their SEDs on the left panel as well as showing the best fit model on a  $T_{inner} - \tau$  plane with the upper and lower  $\dot{M}$  contours overplotted on the right.

Having calculated a mass-loss rate for each RSG, they can be seen in Figure 3.3, plotted against their bolometric luminosities which were derived in Chapter 2 from their SEDs. In clusters, RSGs show a strong positive correlation between  $\dot{M}$  and  $L_{bol}$  where where

all of the RSGs can be assumed to have the same metallicity, the same age and similar initial mass. For M31 though, since we don't control for age or mass, we see very little correlation between mass-loss rate and luminosity, which due to the fact RSGs with similar luminosities may have very different evolutionary paths. This plot, however, does show that there are several high  $\dot{M}$  objects ( $\gtrsim 10^{-5} M_{\odot} \text{yr}^{-1}$ ). As an initial sanity check for our calculated mass-loss rates, we plot K-24 $\mu\text{m}$  vs  $\dot{M}$ , see Figure 3.5, where the colour bar indicates optical depth. There is a strong link between K-24 $\mu\text{m}$  colour and tau, as well as K-12 $\mu\text{m}$  colour and tau seen in Yang et al. (2023) in a study of SMC RSG mass loss. Observing this relationship flags up any objects which may require further inspection i.e. those with high  $\dot{M}$  but low excess (stars occupying in the top right hand corner of Fig 3.5). The 10 highest  $\dot{M}$  RSGs can be seen in Table 3.1. These high rates may place them as candidates for stars which experience short lived high mass-loss or 'super-wind' phases. Details about this phase are discussed later on in Section 3.4.1.

To further investigate these high  $\dot{M}$  stars, we inspected high resolution images (e.g. PHAT) of all objects with  $\dot{M} > 10^{-5} M_{\odot} \text{yr}^{-1}$  with the Spitzer sources overlaid to take a closer look. It was found for several objects that the 24 $\mu\text{m}$  source appeared offset from the optical source in the images, so RGB images of all objects with  $\dot{M} > 10^{-5} M_{\odot} \text{yr}^{-1}$  were constructed, see Figure 3.4 for examples. Previously, in Section 2.1, we discuss how we set stringent limits when cross matching catalogues when obtaining multi-wavelength photometry for our RSG candidates, whereby sources greater than 1.5 arcsecs away from the Khan source were assumed to be not the same source. However, within the Khan Spitzer catalogue there seems to be some mis-match between sources, with detections of the 24 $\mu\text{m}$  waveband not necessarily belonging to the source of interest. This is possibly due to the use of aperture photometry where the flux is likely originating from surrounding objects (and/or noise) and not necessarily arising from the source of interest. It is seen that in the same location as the shorter wavelength sources, there is an absence of any longer wavelength detectable sources.

### 3.3.1.1 24 $\mu\text{m}$ offset correction

The 24 $\mu\text{m}$  band is crucial for estimating  $\dot{M}$  for RSGs. The expelled material from RSG winds form a dusty envelope surrounding the star, where the dust grains within this envelope absorb stellar radiation and re-emit it as thermal radiation in the mid-infrared. The thermal emission of this surrounding dust can provide insights into the circumstellar environment revealing information on mass-loss properties of the star and other key features such as dust composition and dust mass. Therefore these mid-IR wavelengths encode information on both the mass-loss rates of RSGs and the driving mechanisms

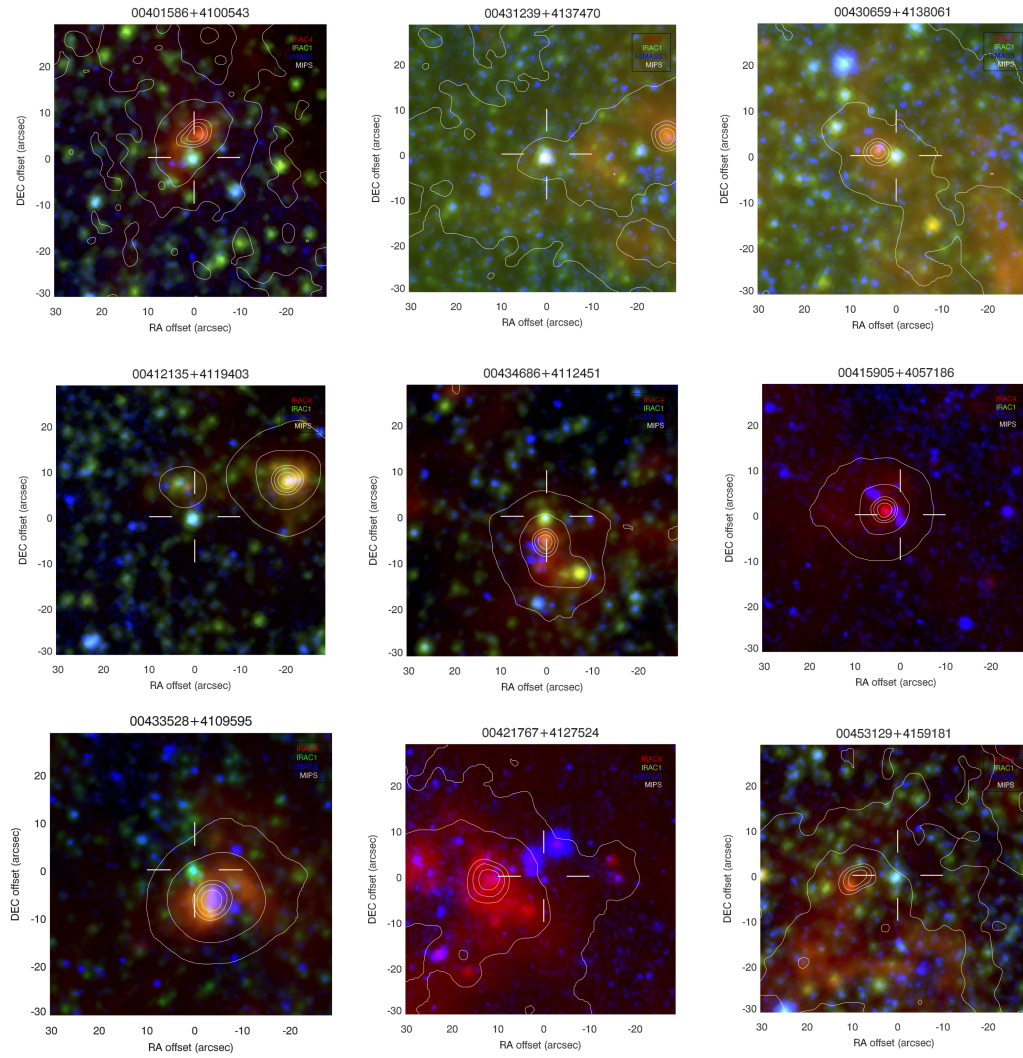


FIGURE 3.4: RGB images of RSGs in the sample. They consist of 2MASS NIR I-band and 3 Spitzer mid-IR bands,  $3.6\mu\text{m}$ ,  $8\mu\text{m}$  and  $24\mu\text{m}$ , revealing any offsets between sources.

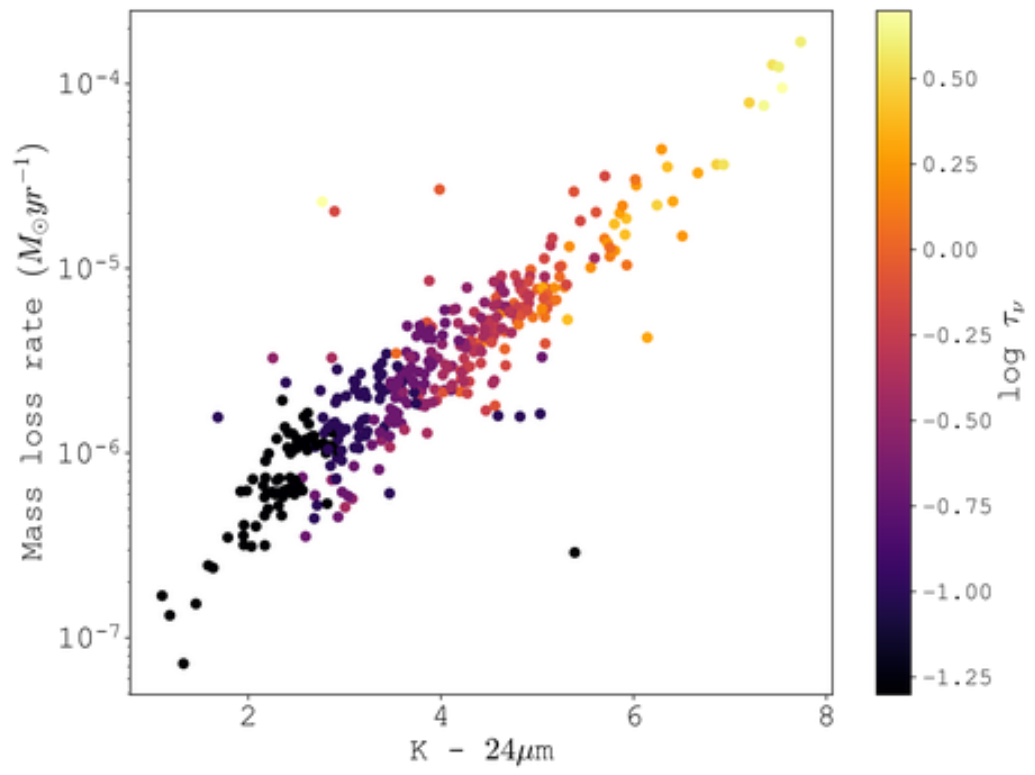


FIGURE 3.5: A colour - mass-loss plot for the RSGs used in this study. The colour bar shows the best fit  $\tau_{\nu}$  value assigned by our DUSTY fitting procedure.

responsible.

As discussed above, closer inspection of the Khan catalogue revealed some IR-bright sources are sat on diffuse emission or in close proximity to (but not associated with) a separate IR-bright point source. In lieu of any detectable source at  $24\mu\text{m}$ , we adopt an upper limit corresponding to the 50% completeness limit for this waveband which was approximately  $m_{24}=12.5$  mags where objects fainter than this become increasingly more unreliable. Figure 3.6 shows a revised version of Figure 3.3, this time indicating any objects with updated  $24\mu\text{m}$  mags and therefore updated  $\dot{M}$ , as per the downward arrows. There are 4 objects that remain in the sample with mass-loss  $> 10^{-5}M_{\odot}\text{yr}^{-1}$  due to no clear issues within their RGB images to apply an upper  $24\mu\text{m}$  limit. These objects are only marginally in the boundary for which we have said may possibly host super-wind RSGs and within the errors still do not have mass-loss rates high enough to be clear-cut super-wind candidates. However, later in Section 3.4.1, we constrain the length of time needed and the  $\dot{M}$  necessary in this phase to strip the stellar envelope entirely. This will give a better view of whether any objects in our M31 RSG sample could be classed these as super-wind RSGs. An updated list of the 5 highest mass-loss rate RSGs is seen in Table 3.2.

After re-examining all objects with  $\dot{M} > 10^{-5}M_{\odot}\text{yr}^{-1}$  and re-calculating  $\dot{M}$  with the upper  $24\mu\text{m}$  limit, this naturally creates an artificial cut-off around this point, seen in Figure 3.6. The aim here was not to provide an accurate  $\dot{M}$  vs  $\log L$  plot, but to show that there are no extremely high mass ‘super-wind’ objects present in the sample. Therefore, this means that it is possible that many of the mass-loss rates in this plot will be over-estimated for the same reason. This however has no effect on our conclusions, since the over-estimation of their mass-loss rates still do not place them in a super-wind phase.

### 3.4 Discussion

RSGs (and AGB stars) are thought to lose mass in the form of a ‘super-wind’, briefly discussed earlier in Section 1, and first explored in Humphreys & Lockwood (1972). Early radiation of Type II supernovae shows its progenitor has dense CSM surrounding the star to core collapse. This is seen through spectroscopy taken soon after shock breakout which unveils narrow emission lines which arise from the CSM, with inferred

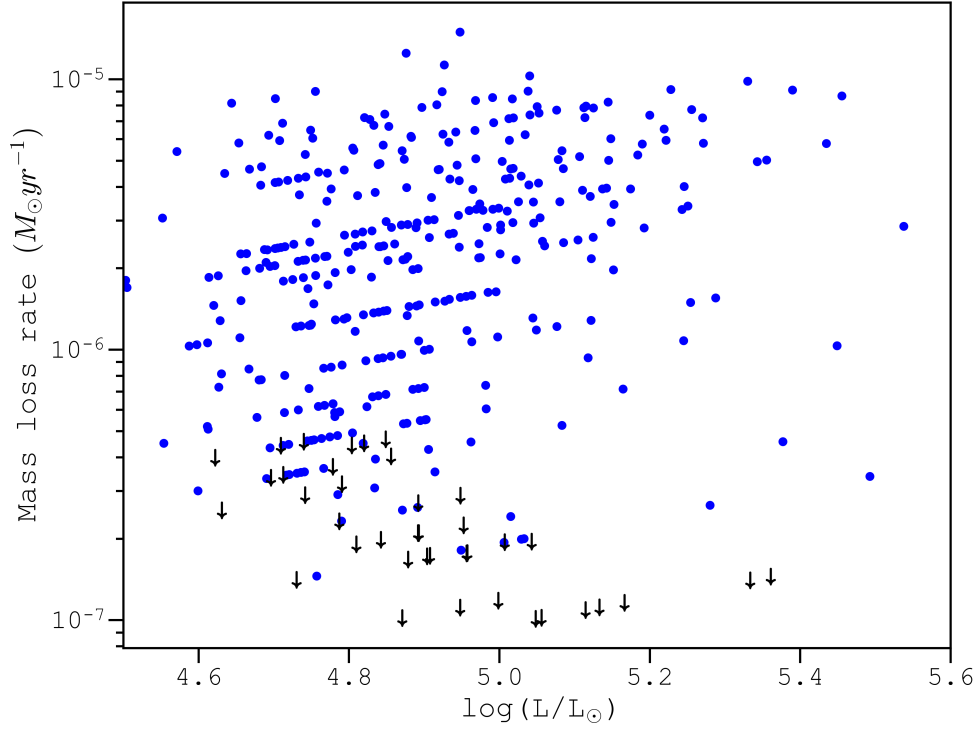


FIGURE 3.6: Same as Figure 3.3 except any objects with  $\dot{M} > 10^{-5} M_{\odot} \text{yr}^{-1}$  with offset sources have had their  $\dot{M}$  re-calculated using an upper  $24\mu\text{m}$  limit. These stars are shown by the black downward arrows.

2MASS name	$\dot{M} (M_{\odot} \text{yr}^{-1})$	$\log(L/L_{\odot})$	$T_{inner}$ (K)	$\tau_{\nu}$
00403605+4038230	1.50E-05	4.94±0.03	600	1.7
00412217+4040255	1.25E-05	4.87±0.03	700	2.0
00403438+4036272	1.13E-05	4.92±0.02	400	0.7
00443537+4151385	1.03E-05	5.04±0.02	600	1.1
00405948+4045425	9.83E-06	5.32±0.02	700	1.0
00452494+4207269	9.17E-06	5.22±0.01	500	0.6
00451490+4137348	9.12E-06	5.38±0.01	500	0.5
00412742+4112409	9.05E-06	5.03±0.02	400	0.5
00404274+4048389	9.02E-06	4.75±0.05	300	0.4
00442793+4152332	9.01E-06	4.92±0.02	600	1.1

TABLE 3.2: Revised 10 highest  $\dot{M}$  RSGs in M31 after an upper  $24\mu\text{m}$  limit has been applied, with their 2MASS designation, luminosity and best model fit  $\tau_{\nu}$  and  $T_{inner}$ .

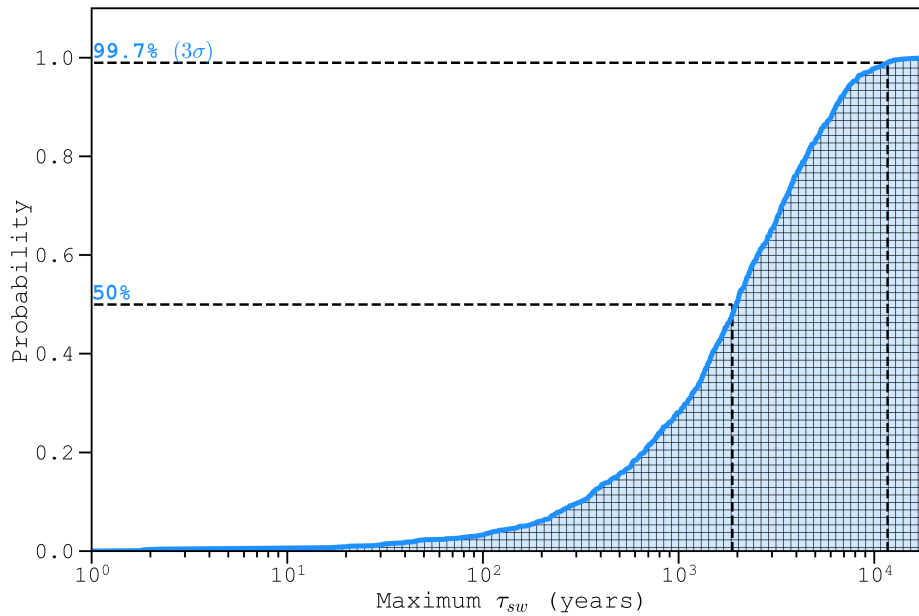


FIGURE 3.7: A cumulative distribution of the Monte Carlo results showing probability (fraction of the sample) as a function of maximum time spent in a super-wind phase.

densities between  $10^{-13}$  and  $10^{-14} \text{gcm}^{-3}$  implying a mass-loss rates between  $10^{-3}$  and  $10^{-1} M_{\odot} \text{yr}^{-1}$  (see, [Morozova et al., 2017](#); [Yaron et al., 2017](#); [Moriya et al., 2017](#)). In [Beasor et al. \(2020\)](#), they show that RSG winds are not effective at removing the hydrogen envelope which implies that stripped stars (type 1b/c progenitors) cannot evolve from single stars. Therefore if a super-wind phase occurs it must be removing the entire envelope in a short time.

To investigate this, we perform two tests. Firstly, we perform a Monte Carlo experiment to find the probability of observing an M31 RSG in a super-wind phase. Secondly, we use the MESA-MIST models to predict how high the super-wind mass-loss rate would need to be for RSGs to lose their entire envelope in this phase.

### 3.4.1 Super-wind analysis: Monte Carlo

The sample of M31 RSGs contains 387 objects provides us with the best chance of observing a RSG in the super-wind phase. The mass-loss rate of RSGs during this phase needs to be significant enough to remove the entire envelope and transpire within a short time-frame that makes it hard to capture. The Monte Carlo experiment is used

to assess the probability of observing RSGs in a super-wind phase based on the size of the sample. For this, we assume a uniform RSG lifetime of 1Myrs with an envelope mass of  $10M_{\odot}$  as 1Myrs is approximately 10% of the lifetime of a  $20M_{\odot}$  star. Of our sample of 387 RSGs, we do not observe any clear cut candidates which seem to be experiencing a super-wind phase. Taking this into account, we can estimate the maximum fraction of the RSGs lifetime needed to be spent in this phase required to remove the entire envelope.

The Monte Carlo experiment is constructed by first generating 387 random numbers between zero and 1 one for each RSG in our observed sample, each time recording the minimum number. This is repeated  $10^5$  times, where each minimum value represents the fraction of the time in the SW phase which is too small to be observed. The cumulative distribution of the results can be seen in Figure 3.7. It can be seen that for one RSG, if the phase lasted 3000 years, there is a 50% chance would miss it. Where  $p=99.7\%$ , the duration of a super-wind is  $\sim 10,000$  years which means we can exclude a phase lasting longer than this at the  $3\sigma$  confidence level. Since this is approximately 2% of the stars lifetime (assuming a nominal RSG lifetime of 1Myr), in order to lose  $10M_{\odot}$  during this time, it would require  $\dot{M}$  to be  $5 \times 10^{-4} M_{\odot} yr^{-1}$ . Therefore any phases shorter than this, would require an even higher  $\dot{M}$ . The minimum  $\dot{M}$  in a super-wind phase lasting  $< 3000$  years would therefore have to be  $\sim 1 \times 10^{-3} M_{\odot} yr^{-1}$ . Finally, if RSGs are spending  $\sim 1\%$  of their life in the super-wind phase, based on our sample size, we should expect to see 3-4 with stars with  $\dot{M}$  greater than  $1 \times 10^{-3} M_{\odot} yr^{-1}$ .

### 3.4.2 Super-wind analysis: MESA-MIST

To expand further on the results from the Monte Carlo, we use the MESA-MIST stellar evolutionary tracks to predict the mass-loss rates necessary to remove the entire hydrogen envelope  $M_{henv}$ . We look at RSGs with masses  $12M_{\odot}$ ,  $15M_{\odot}$ ,  $18M_{\odot}$ ,  $21M_{\odot}$ ,  $24M_{\odot}$ , and  $27M_{\odot}$ , and determine  $M_{henv}$  at the end of the MS as being the total current mass minus the mass of the He core. Then, we determine the remaining lifetime of the star. The time averaged mass-loss rate necessary to remove the envelope is then simply  $M_{henv}$  at the start of the RSG phase divided by RSG lifetime ( $\tau_{RSG}$ ). If  $\dot{M}$  is essentially negligible throughout the majority of its life then we can make the simplifying assumption that all mass is lost in the SW phase. To remove the envelope, the required  $\dot{M}$  in the SW phase then becomes:

$$\dot{M} = \frac{M_{henv}}{\text{fraction of time in SW phase} \times \tau_{RSG}} \quad (3.3)$$

This is shown in Figure 3.8 which has the MIST results over-plotted on the  $\dot{M}$  vs  $\log(L/L_{\odot})$  results from Section 3.3.1. There is no unique Mass-Luminosity relation for RSGs, so to compare theoretical results to our observations we need to make a simplification. For RSGs at the ends of their lives, Davies & Beasor (2020) showed that  $L \sim M^2$ , and that  $L \sim 10^5 L_{\odot}$  for a  $15M_{\odot}$  RSG. The luminosities of the MIST RSGs are therefore determined by normalising to a RSG with a mass of  $15M_{\odot}$  and luminosity of  $10^5 L_{\odot}$  using the following relation:

$$\left(\frac{L}{10^5 L_{\odot}}\right) = \left(\frac{M}{15M_{\odot}}\right)^2 \quad (3.4)$$

*Equation 3.4.2: where  $L$  is the luminosity of the RSG and  $M$  is the stellar mass both of which are being normalised to a RSG with a luminosity of  $10^5 L_{\odot}$  and a mass of  $15M_{\odot}$ , respectively.*

For the non-super-wind case, this is represented by the dark blue line in Figure 3.8. The middle blue line shows the results of a RSG which spends 10% of its lifetime in a super-wind phase, then we should observe 10% ( $\sim 30 - 40$ ) of our M31 RSGs with  $\dot{M}$  above the middle line, where again we do not see any. The light blue line shows RSGs spending 1% of its life in a super-wind phase, where we should be seeing  $\sim 3$  of our observed RSGs situated, and yet again we observe zero. In a sample of 387 RSGs, when expecting to see 3-4 objects in a super-wind phase, but observe none, this is not completely unexpected. This means we can't rule out a SW phase that is  $\leq 1\%$  of the RSG lifetime. However, to remove the envelope in a time-span as short as 1% of the RSG lifetime, the rate would need to be  $\sim 10^{-3} M_{\odot} \text{yr}^{-1}$ .

The only processes thought to remove mass at rates considerable enough to remove entire envelopes in short periods are eruptive episodes seen in LBVs or binary mass transfer. This has been investigated in the literature in a number of studies from other angles. Firstly Beasor & Smith (2022) show that if there is any viable single-star route that can produce a stripped envelope star, then it must be due to 'dust-enshrouded RSGs', which are RSGs heavily reddened by vast amounts of circumstellar dust, implying a high mass-loss rate and therefore a possible super-wind phase. Here  $\dot{M}$  is thought to be at least a factor of 10 higher than normal RSGs (Beasor et al., 2020), however, these stars are rare with only a one confirmed true dust-enshrouded RSG in the LMC

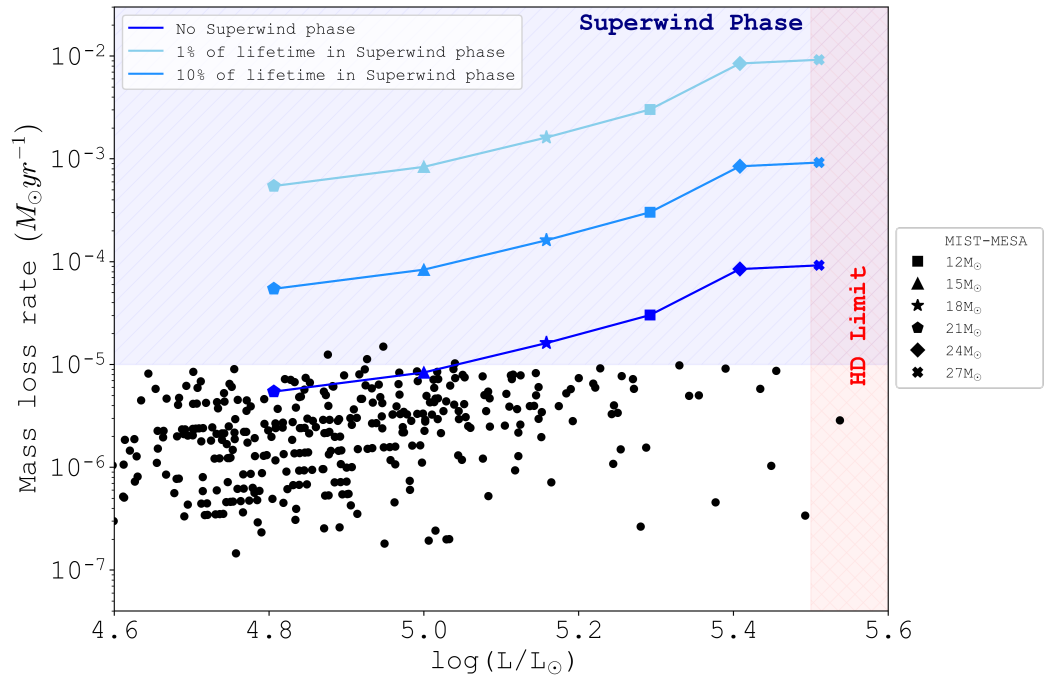


FIGURE 3.8: Mass-loss rate vs luminosity for the observed M31 RSG sample, with the MIST model predictions overplotted. The blue lines represent the mass-loss rate necessary in any SW phase to remove the envelope, where shorter SW phases require larger  $\dot{M}$ . The varied symbols on the MIST lines depict RSGs of different masses, as described in the legend on the right.

(WOH G64) and one dust enshrouded candidate also in the LMC (LI-LMC1100) [Beasor & Smith \(2022\)](#). They demonstrate that if this is a phase experienced by all RSGs as seen in Figure 3.7 in the present work, this phase must be short-lived. Additionally, if dust-enshrouded do represent a phase experienced by all RSGs prior to SN then the scarcity of these objects means that in the short time frame of the outburst, only a further  $1 - 2M_{\odot}$  of material would be stripped away from the envelope. Further, in [van Loon et al. \(1999\)](#) they look at the maximum RSG mass-loss rates from an alternative viewpoint, in that  $\dot{M}$  should be compared with the rate at which mass is consumed by nuclear burning ( $\dot{M}_{nuc}$ ) and this determines the evolutionary timescale in the absence of high mass-loss. For most of the RSGs in their study,  $\dot{M}_{nuc}$  which cannot remove a large fraction of their envelope before SN. Based on the number of stars with exceptionally high mass-loss rates where  $\dot{M}$  potentially exceeds  $\dot{M}_{nuc}$  (2, WOH G64 and IRAS04530-6916), they estimate that RSGs spend about 25% of their RSG lifetime in an intense mass-loss phase at  $\sim 10^{-3} M_{\odot} \text{yr}^{-1}$ . Overall, these results all indicate that the significance of winds in the context of massive stellar evolution and the formation of envelope stripped stars, is not as important as previously presumed.

### 3.4.3 Comparison Wang et al (2021)

A study by [Wang et al. \(2021, hereafter, W+21,\)](#) also investigates the mass loss rates of M31 RSGs. They use a similar method to the work in this thesis where they also fit observational photometry to SEDs using the DUSTY radiative transfer code. However they find a number of high mass loss RSGs (average  $\dot{M} = 2 \times 10^{-5} M_{\odot} \text{yr}^{-1}$ ) compared to the present work and other RSG mass loss studies. Determining the mass loss rate of RSGs is extremely sensitive to the parameters chosen to fit to the SED. For example, in this thesis a gas-to-dust ratio,  $r_{gd} = 1:200$  is chosen, whereas W+21 use 1:100. This difference alongside parameters such as grain bulk density, dust grain species and dust size distribution varying can lead to a difference in results to be up to one order of magnitude ([Yang et al., 2023](#)). Also, the SEDs of the highest mass loss rate RSGs in W+21 are not present in the paper which doesn't allow for inspection of the mid-IR excess they determine.

## 3.5 Summary

In this work, we determined the mass-loss rates of M31 RSGs, by modelling the mid-IR flux as a star surrounded by a dusty wind. We no clear-cut candidates for any RSGs experiencing a super-wind phase. If the super-wind phase is experienced by all RSGs,

---

then the lack of observed objects with  $\dot{M}$  high enough to be in this regime indicates that this phase is extremely short lived. The results of a Monte Carlo experiment show we can exclude a super-wind phase lasting longer than  $\sim 10,000$  years at the  $3\sigma$  confidence interval, with the minimum  $\dot{M}$  required to remove the envelope in this time being  $\sim 10^{-3}M_{\odot}yr^{-1}$ . Our M31 RSG sample finds zero objects with  $\dot{M}$  even close to this number. Ultimately, we argue that since the only processes known to remove considerable mass from in short time frames are LBV-like eruptions and binary interactions, for the formation of stripped-envelope stars, both main sequence and RSG winds are not significant enough to form these stars from single-star pathways.

## Chapter 4

# Using machine learning techniques to estimate red supergiant mass loss rates and luminosities

In Chapter 3, the importance of mass loss on the evolution of an RSG is discussed in detail, as well as the difficulty in measuring it directly. The cool temperatures of RSGs mean they are dominant sources of near-IR radiation, plus near-IR wavelengths suffers less from extinction caused by interstellar dust which allows us to probe deeper into the dusty circumstellar environment of these stars where the mass loss occurs. However interpreting mid-infrared observations of RSGs is challenging, as they are subject to various physical processes that can affect the observed signal. Optical wavelengths however can provide valuable insights into the behaviour of RSGs, such as the visible RSG spectrum which exhibits absorption lines such as TiO bands which can be used for temperature estimates. These optical observations can also indirectly uncover information about the mass loss processes in RSGs, where the strength and profile of these absorption (and also emission) lines in the optical spectrum can indicate the presence of stellar winds or outflows which can offer glimpses into the RSG mass loss mechanism. Additionally the optical variability of RSGs can sometimes be indicative of pulsations or episodic mass loss events which can similarly inform us about mass loss behaviour. By separately examining wavebands, a novel perspective on RSG mass loss may emerge, free from the dominant influence of the mid-IR.

In both Chapters 2 and 3, we've shown how we can use physical models to derive both

$L_{bol}$  and  $\dot{M}$  for a sample of M31 RSGs. In the current chapter we investigate whether machine learning may provide a promising solution to finding a quicker, cost effective method for deriving the same parameters. We aim to use a linear regression model to correlate both  $L_{bol}$  and  $\dot{M}$  with the stars' observables, including those observables not used in the modelling, but that are widely available (see Section 4.1). Thus, machine learning could be a way to rapidly find correlations and empirical calibrations between observables and physical properties for larger samples of stars, allowing for similar studies to those in Chapters 2 and 3 but on much larger scales and for many more galaxies.

## 4.1 Method

The objective of this study is to develop a machine learning algorithm that utilises a range of optical to mid-IR observational photometry to use as 'features' to determine accurate and precise mass loss rates and luminosities for RSGs.

For our input data, we use the observational photometric fluxes and known mass loss rates for the sample of M31 RSGs from Chapters 2 and 3 to train the model. This sample consists of RSGs in M31 which have available mid-IR photometry, so any with missing or incomplete coverage in Spitzer are removed from the sample. Therefore, the total number of M31 RSGs used throughout this Chapter is 387. The RSG fluxes used are calculated previously in Section 2.1.3 and converted to absolute flux in this work to account for distance. The fluxes used are bp and rp (Gaia eDR3), JHK (2MASS) and  $3.6\mu\text{m}$ ,  $4.5\mu\text{m}$ ,  $5.8\mu\text{m}$ ,  $8.0\mu\text{m}$  and  $24\mu\text{m}$  (Spitzer). These were chosen because they were previously used in both the determination of the HD-limit and mass loss rates of M31 RSGs and are also freely available in large surveys with coverage across a variety of local group galaxies.

### 4.1.1 Linear regression

The algorithm we use is a simple linear regression model which uses the equation of a line to form the basis of the model, to describe the relationship between a set of dependent variables  $y_n$  and a set of observations  $X_{(n,f)}$  where  $f$  is the number of observables per data-point. For a simple scenario of one independent feature and one dependent variable.

$$y = \beta_0 + \beta_1 X \quad (4.1)$$

Equation 4.1: where  $y$  is the dependent target variable,  $X$  is the independent input feature,  $\beta_0$  is the  $y$ -intercept (the value of  $y$  when  $x$  is 0) and  $\beta_1$  is the coefficient (slope) that represents the relationship between  $x$  and  $y$ .

To train the model, the fluxes for all the M31 RSGs are first split into a test and training set, in the ratio 25:75. A steep increase in the variation of the rms over 1000 random seeds is seen beyond a training sample fraction of 0.75. As such, a split of 25:75 gives the optimal balance of training and validation information to the reliability of assessment of the model performance on unseen data. A higher training fraction, e.g. 0.85, would result in a slight decrease in the rms error but the spread in rms is much higher ( $\sim 0.4dex$ ) compared to  $\sim 0.1$  at 0.75. An ordinary least squares (OLS) optimisation method is implemented which aims to find the best-fitting linear relationship between  $y_n$  and the target variable by minimising the sum of the squared differences. The goal of OLS is to find the coefficients of the linear equation that result in the smallest possible loss function which for this current work is the Mean Squared Error (MSE).

### 4.1.2 Varying the loss function

As discussed above, the loss function is a parameter which quantifies the difference between the output from the model and the true value and is a measure of how well the model is performing on the data set. By minimising this error, the model can strengthen its ability to make more accurate predictions.

In section 4.2.1, we use a mean squared error loss function, which measures the average squared difference between the predicted and true values, see equation 4.2. This penalises larger errors more so than smaller ones because the differences are squared, since larger errors contribute more to the overall loss value compared to smaller errors. Therefore the model aims to find the set of parameters that minimises the average squared difference between its predictions and the true values.

$$MSE = \frac{1}{N} \sum_{i=1}^N (y_i - \hat{y}_i)^2 \quad (4.2)$$

Equation 4.2: where  $N$  is the number of samples we are testing against,  $y_i$  represents the true values and  $\hat{y}_i$  is the average squared difference between the true and predicted values.

Mass loss model (MSE loss function)		
Features	Training set rms error	Test set rms error
All features	0.231	0.144
bp, rp, J, H and K	0.472	0.517
bp and rp	0.473	0.516
Luminosity model (MSE loss function)		
Features	Training set rms error	Test set rms error
All features	0.054	0.032
bp, rp, J, H and K	0.061	0.036
bp and rp	0.100	0.090
K only	0.091	0.064

TABLE 4.1: The rms errors for both the training and test set when varying the number of features used.

The results of using an MSE loss function in the model are seen in Table 4.1. For mass loss, when the model is trained on all features we see that the rms error for the test set is lower compared to the training set which is a good indication that the model is working efficiently. For luminosity, for all variations of features we see an improved rms error in the test set which again is a promising sign that the model is working well.

In this section, we introduce two new loss functions, huber loss and epsilon-insensitive loss where we use each in our regression model and observe how the rms error changes compared to when using a MSE loss function. An additional metric,  $R^2$  score, is also introduced in this section, as a means of offering a more comprehensive evaluation of the model's performance. The  $R^2$  score measures the proportion of variance in the dependent variable (i.e. mass loss and luminosity, in this case), that can be explained by the independent variables (fluxes). It therefore is a measure of how well the model explains the variation in the data. This is determined using the following equation:

$$R^2 = 1 - \frac{SS_{res}}{SS_{tot}} = 1 - \frac{\sum_i (y_i - \hat{y}_i)^2}{\sum_i (y_i - \bar{y}_i)^2} \quad (4.3)$$

Equation 4.3: where  $SS_{res}$  is the residual sum of squared errors of the regression model and  $SS_{tot}$  is the total sum of squared errors.

#### 4.1.2.1 Huber loss

Huber loss is a hybrid loss function which combines the characteristics of MSE, and the mean absolute error (MAE), which is the average absolute difference between the predicted and true values. It is designed to be less sensitive to outliers compared to a MSE loss function and uses a parameter,  $\delta$ , which controls the threshold where it transitions from behaving like MSE to MAE, i.e. from quadratic to linear. When the difference between the predicted and true values is within the  $\delta$  threshold, it penalises errors quadratically whilst a difference greater than the  $\delta$  threshold will be penalised linearly, see equation 4.4.

$$L_{\delta}(y, \hat{y}) = \begin{cases} \frac{1}{2}(\hat{y} - y)^2, & \text{if } |\hat{y} - y| \leq \delta \\ \delta|\hat{y} - y| - \frac{1}{2}\delta^2, & \text{otherwise} \end{cases} \quad (4.4)$$

*Equation 4.4: where  $L_{\delta}(y, \hat{y})$  is the huber loss and  $\delta$  is the threshold parameter that determines the point at which the loss transitions from quadratic to linear.*

To implement the Huber loss function, we use a linear regression model that utilises an optimisation algorithm called Stochastic Gradient Descent (SGD) to find the optimal coefficients. SGD is an iterative method that modifies the coefficients gradually based on randomly selected subsets of the training data, allowing the model to converge to the optimal solution. The  $\delta$  parameter is set to 1.35 which corresponds to the point where the quadratic and linear components of the Huber loss function intersect. This is a balance between robustness to outliers and the ability to capture the quadratic behaviour exhibited by significant errors. Once applied, 4 tests are performed where each time the number of input features is changed each time. The first test uses all 10 flux bands as inputs, for the second the mid-IR fluxes are removed, then only the optical fluxes and finally solely K-band fluxes. This is performed with both mass loss rate and luminosity as the target variable. The  $R^2$  score and rms error results of these analyses can be seen in table 4.2. For predicting mass loss rate when using all features, bp and rp only and K-band as inputs, the huber loss function performs essentially just as well as when using the MSE, with only marginally smaller values for  $R^2$  score and rms error. For luminosity however, huber loss performs comparatively well with the MSE in all 4 tests. The high  $R^2$  scores of 0.955 and 0.944 when using all features and all but mid-IR, respectively, strongly suggest that these features offer a means to predict consistent luminosities for our M31 red supergiants. Additionally, in the absence of those features, determining luminosity based solely on K-band fluxes can provide a

good alternative, with an  $R^2$  score of 0.863. This was also shown previously in Chapter 2, where in the absence of mid-IR photometry for our SEDs, a luminosity determined using a K-band bolometric correction was found to be a suitable alternative. The model using bp and rp fluxes performed the poorest, but still was able to predict luminosities more accurately than when using the same features to predict a mass loss rate.

#### 4.1.2.2 Epsilon-insensitive loss

The second loss function used is epsilon-insensitive loss, which measures the error between the predicted values and the actual values using a parameter,  $\epsilon$  which expresses a threshold for error. When the absolute difference between the predicted and true values is smaller than epsilon range, the loss is zero. When the difference exceeds epsilon, it is considered an error and contributes to the loss, proportionally to the deviation, see equation 4.5. By establishing the  $\epsilon$  threshold the epsilon-insensitive loss enables the model to prioritise significant errors while showing reduced sensitivity towards the smaller errors. This means epsilon-insensitive loss is generally more robust to outliers compared to the Huber loss and MSE.

$$L_{\epsilon}(y, \hat{y}) = \begin{cases} 0 & \text{if } |y - \hat{y}| \leq \epsilon \\ |y - \hat{y}| - \epsilon & \text{otherwise} \end{cases} \quad (4.5)$$

*Equation 4.5: where  $L_{\epsilon}(y, \hat{y})$  is the epsilon-insensitive loss and  $\epsilon$  represents the threshold value that determines the maximum allowable difference between the true value  $y$  and the predicted value  $\hat{y}$  before the loss is non-zero.*

A similar approach is employed as used for the Huber loss, where we use an SGD regressor, this time with the  $\epsilon$  parameter. This is set as  $\epsilon=0.1$  which means the the model will be tolerant to prediction errors within a range of  $\pm 0.1$ . This is a trade-off between model accuracy and robustness to outliers. An excessive  $\epsilon$  can lead to under-fitting because the model becomes too tolerant of errors and fails to capture important intricacies in the data and an  $\epsilon$  too low can lead to over-fitting, where the model becomes too sensitive to noise or small data fluctuations and may struggle to on unseen data. Similarly to huber loss, this new model is tried on the same 4 combinations of features, the results of these can also be seen in table 4.2. For mass loss predictions, the epsilon-insensitive loss performs better than both huber and the MSE loss in the model

using all features with an rms error of 0.108 and  $R^2=0.960$ . However similarly to using huber loss, for the other 3 tests the model performs poorly. These results suggest that without mid-IR fluxes, obtaining an accurate mass loss rate not feasible, as the model's ability to explain the variations in the target variable is very limited. For the luminosity predictions, epsilon-insensitive loss again performs well compared to huber loss and the MSE, showing its ability to accurately predict luminosity with high accuracy, regardless of whether using the full range of features, all but mid-IR fluxes or just K-band fluxes. In a similar manner, to huber loss for predicting luminosity, using only bp and rp is the worst performing model, but was still able to capture  $\sim 67\%$  of the variability of the luminosity using only these two input features. These results are discussed further in the next section.

After testing a few loss function alternatives, using the MSE loss function is found to be the optimal match. This is because outliers will have a strong influence on the results of this work and using the MSE ensures our trained model has no outlier predictions with large errors. This is a result of the MSE putting larger weight on these errors due to the square factor of the function. For the remainder of the work in this chapter, all models will be employing the MSE loss function.

### 4.1.3 Random states

A parameter used in training the linear regression models is random state, which is used to control the random seed when splitting the input dataset into training and testing data. Dealing with randomness can influence results and lead to variations in model performance metrics as different subsets of data being used for training and testing may affect the model's ability to generalise to unseen data. In particular, with small sample sizes where the variability in the data is relatively higher, even minor variations to splitting of the data can hinder the model's ability given the limited data it has access to. Therefore, a simple sampling test was performed to check that the results are stable for a number of different random seeds and assess the impact (if any) to gain insights into how sensitive the model is to the random splitting of the data.

For both the luminosity and mass loss model (with MSE loss functions), a random state in the range of 1 to  $2^{32} - 1$  (the maximum allowed value) is randomly selected to train-test-split, then the model is fit to the training data as normal, calculating the rms error of the test set each time. This is repeated for 1000 iterations where the standard deviation

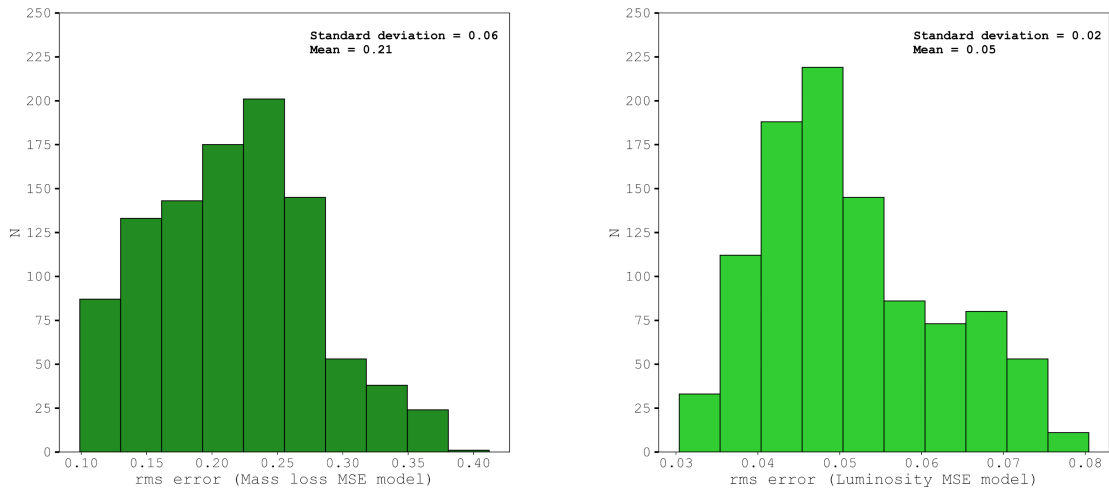


FIGURE 4.1: A distribution of the rms errors for both  $\log \dot{M}$  and  $\log L$ , resulting from varying the random state during the train-test-split process, using all features.

is then determined from the distribution of rms errors, see Figure 4.1. The standard deviation for the mass loss and luminosity models is 0.06 and 0.02, respectively. This suggests there is relatively low variability in the model’s performance across different random splits and the rms errors from different iterations are clustered closely around the mean value. This implies that the model’s performance was moderately stable, regardless of how the input data is split for training and testing.

## 4.2 Results

### 4.2.1 Mass loss rates of red supergiants using linear regression

Once the model has been trained, it is used to make  $\dot{M}$  predictions from the remaining fraction of unseen data. The best-fitting line is found which minimises the loss function, i.e. the difference between the predicted and actual target values. This is seen in figure 4.2. This plot shows the relationship between the input fluxes and mass loss rates with the estimated linear trend overplotted, where uncertainty is the 99.7% confidence limit, depicted by the red shaded region. The fit between points and regression line results in a root mean square (rms) error of 0.144 dex for the test set, which implies that the regression line reproduces  $\dot{M}$  to an average error of 0.144dex per data point, given the input fluxes used. Another metric used to assess the goodness of fit is the  $R^2$  score which measures the the proportion of the variance in the dependent variable that is explained by the independent variables used in the model by comparing the fit of the

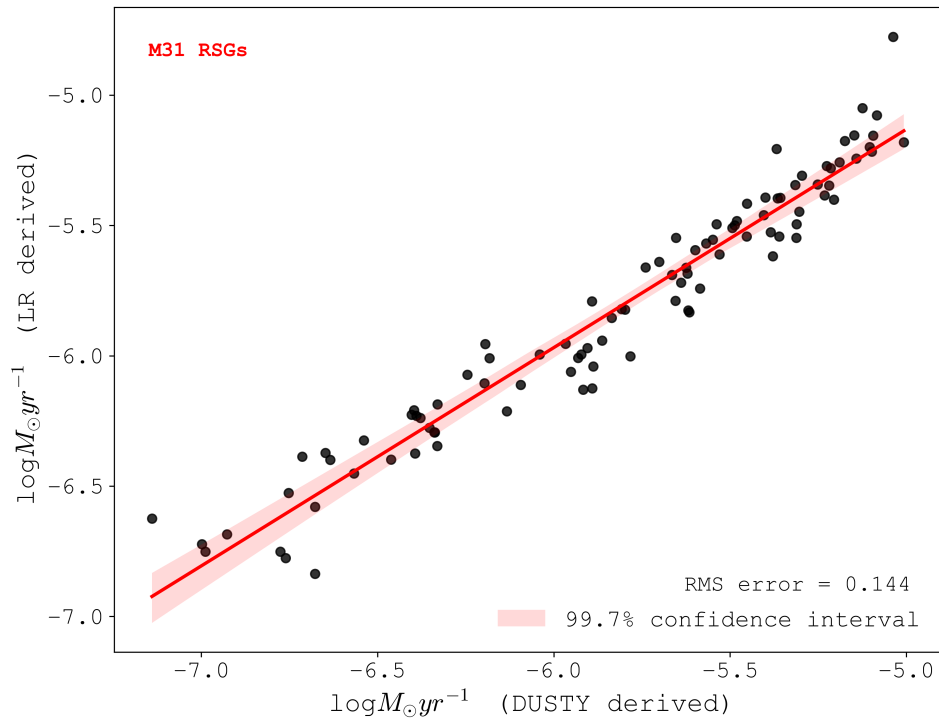


FIGURE 4.2: A linear regression plot where the model was trained on all 10 input features (optical through to mid-IR), showing the  $\dot{M}$  predictions from the model as a function of mass loss rates determined from DUSTY in the previous chapter.

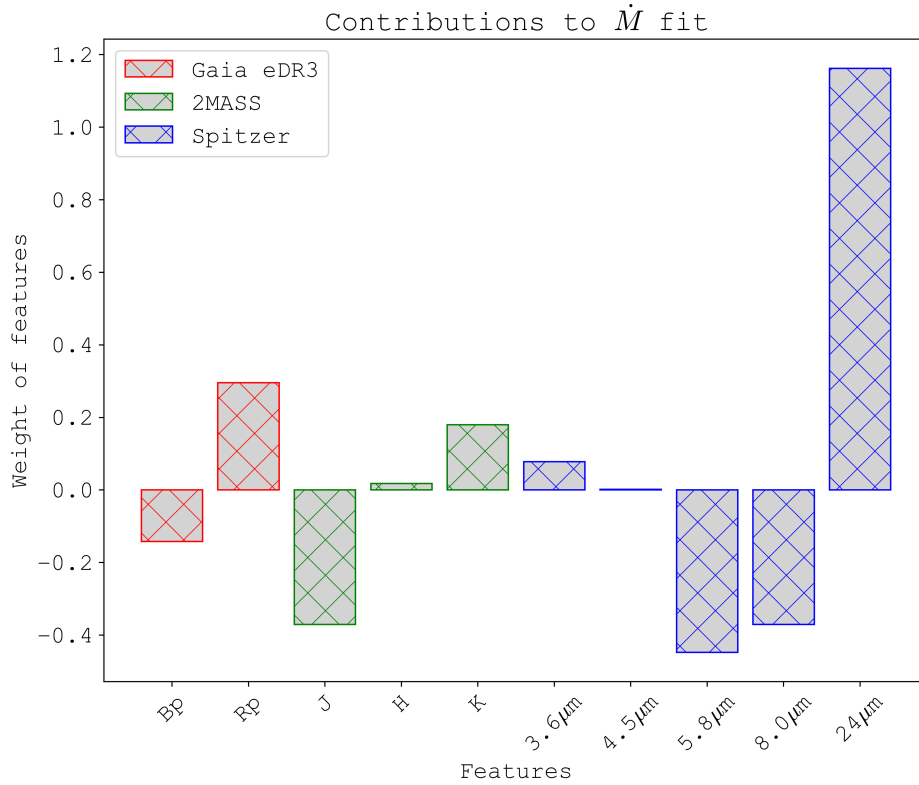


FIGURE 4.3: The coefficients for each of the independent variables used in the linear regression model, which each represent the weighting of each variable on the target value,  $\dot{M}$ .

chosen model with a horizontal straight line (the null hypothesis). The  $R^2$  score for this model is 0.931 which implies that 93.1% of the variability of the mass loss is explained by the model, and therefore 6.9% is due to either omitted variables in the model, stochastic effects and/or other relationships influencing the dependent variable that are not captured by the model. Therefore this metric is always used in conjunction with other tests of goodness of fit such as rms error, since interpreting the variability is challenging.

From Chapter 3, we know the importance of mid-IR photometry for studying the mass loss phenomena of RSGs. This is validated for our flux sample by exploring the optimised model's weights for each of the features. Figure 4.3 shows these coefficients for the features used in our regression model where it can be seen that there are both correlated and anti-correlated coefficients which represent the weights associated with each feature in the input data. In particular, the strong positive coefficient for the 24  $\mu\text{m}$  band shows the relative importance of this variable. The larger coefficient seen for 24  $\mu\text{m}$  suggests that it has the strongest influence on the mass loss rate compared to

the other features. In a scenario where too many features are resulting in over-fitting of the model, features with close to zero coefficients which are having a negligible influence on the predicted variable can be possibly be excluded from the model, simplifying it without compromising the performance of the model.

### 4.2.2 Mass loss rates from reduced datasets

In the previous section, the largest and therefore most influential coefficient in the model was for the  $24\mu\text{m}$  band. Building on this, we proceeded to test whether an adequate mass loss rate could still be obtained when using only optical photometry. Although optical wavelengths may not directly probe the circumstellar material responsible for the mass loss, and we don't have a physical model that can predict  $\dot{M}$  from Gaia bp/rp, a strength of using machine learning is that we can calibrate a relation if one is found to exist. For [Davies & Beasor \(2018\)](#) find for RSGs in clusters a clear trend of the most luminous and therefore most evolved RSGs have a later spectral type, and this correlation could be picked up in the Bp-Rp colour. Having the capability of predicting mass loss rates from shorter wavelength photometry would mean the wealth of archival optical data available could be used to perform large-scale surveys of red supergiants, providing valuable studies on their mass loss properties across different populations and evolutionary stages. Also, having additional avenues to explore RSG mass loss behaviour will result in better constrained rate estimates which are essential for models of stellar evolution, and ultimately will improve our understanding of the physics governing mass loss in RSGs.

Firstly, we explore the mass loss rates obtained by omitting any mid-IR data, using only bp, rp, J, H, and K bands as features in our model, thereby removing the main source of insights into dust and thermal emission. The experiment is then replicated for a second instance, this time using solely the bp and rp bands, excluding all near-IR data. From [Figure 4.3](#), it can be seen that our new highest weighting coefficient for the absence of mid-IR scenario is J band, with an anti-correlated weighting of -0.35, which would decrease the mass loss rate. For the bp and rp experiment, the rp band has the largest weighting of 0.25. [Figure 4.4](#) shows the results, with panel 1 showing the result of the Gaia and 2MASS features and panel 2 showing only Gaia. With the exclusion of mid-IR photometry, we see a clear increase in rms error from 0.144 when using all features to 0.517 with only optical to near-IR. This is evident that excluding the mid-IR features has a negative impact on the model's predictive performance, which is expected. However, there is very little difference to the rms error whether we

have the near-IR data or use only the optical bp and rp bands, as the rms error for the optical-only test yields an rms error of 0.516. Given the comparable rms errors for both cases, we again use the  $R^2$  score metric to further evaluate. We find  $R^2=0.113$  for the absent mid-IR model and  $R^2=0.116$  for the bp and rp model. Both of these metrics indicate that the features used are not good predictors of the target variable. Since we know the addition of mid-IR vastly increases the performance of the model, these low  $R^2$  scores and rms errors can be ultimately be attributed to the absence of important independent variables that have a strong relationship with the mass loss rate. Ultimately, this suggests that obtaining an adequate mass loss rate from photometric fluxes is not feasible when eliminating mid-IR data.

### 4.2.3 Predicting M31 red supergiant luminosity using linear regression

Luminosities of the RSGs used throughout this thesis were calculated in Chapter 2.1.3 by integrating their SEDs. The fluxes used to plot the SEDs are the same as the input fluxes used as the model's features, which means the target variable can be changed to also make estimations of luminosity. These can be compared to the SED luminosity to test the performance of the model.

Similarly, as done previously for mass loss, Figure 4.6 shows the weightings of the features that will be used for determining luminosity from the model. K-band wavelengths are favourable for studying red supergiant luminosity due to being less susceptible to reddening compared to lower wavelengths (Neugent et al., 2020). Therefore using K-band photometry is a cheap and effective method for determining RSG luminosity. However, we see a much larger weighting for J-band, which means that it is optimising on J-band which is minimising the error and/or maximising the performance of the model. This could be due to reasons such as smaller errors on J-band photometry, lack of sensitivity of 2MASS K-band, or larger errors for K-band magnitudes, which might result in a greater spread on the correlation between  $L_{\text{bol}}$  and K-band.

Using the same ratio of training and test data as used for mass loss, a subsequent linear regression model with an MSE loss function is used to estimate luminosity, see Figure 4.5. Firstly, the model performs strongly with an  $R^2$  score of 0.955 and rms error = 0.031 when incorporating all features. This signifies that the model captures approximately  $\sim 96\%$  of the variability in the target variable, suggesting a high level of accuracy in

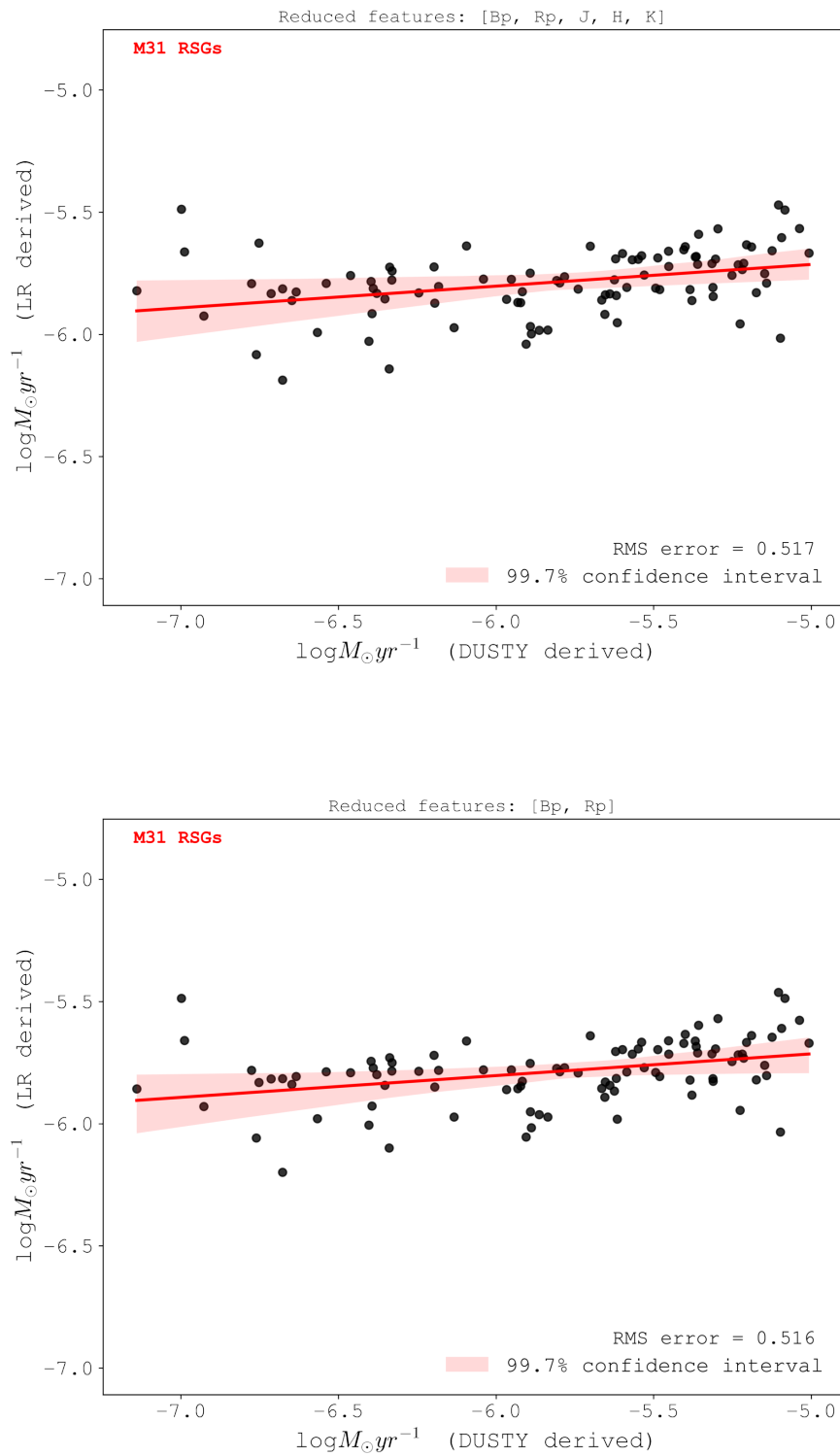


FIGURE 4.4: Same as Figure 4.2 but this time with the model trained on reduced features. In the top panel, the model is trained only on Gaia bp and rp and 2MASS J,H and K bands and the bottom panel shows the model trained solely on Gaia bp and rp bands.

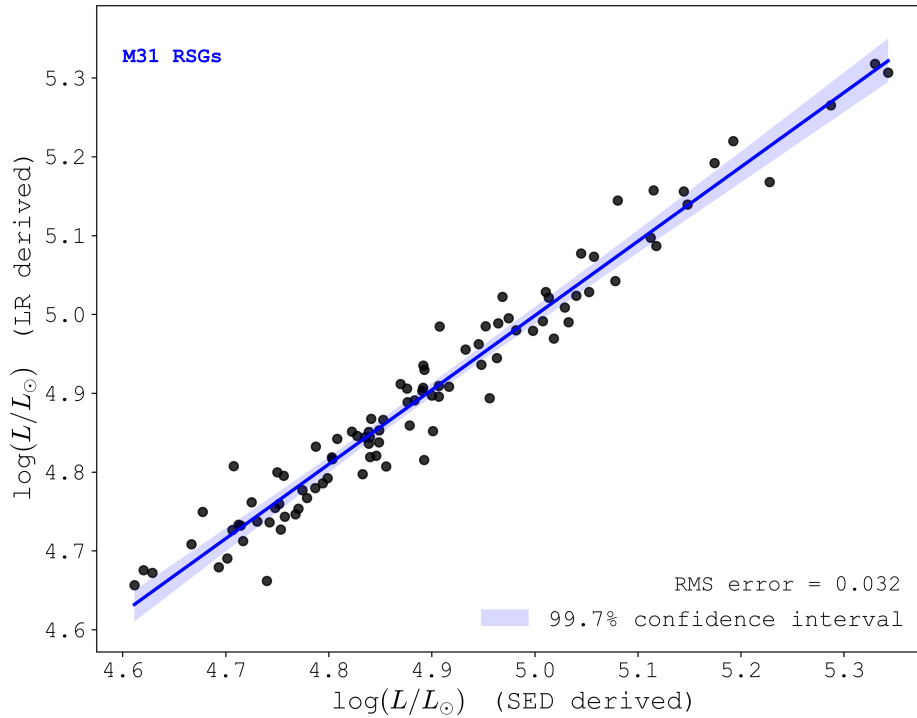


FIGURE 4.5: A linear regression plot where the model was trained on all 10 input features (optical through to mid-IR), showing the  $L_{\text{bol}}$  predictions from the model as a function of bolometric luminosity determined from their SEDs in Chapter 2.

predicting luminosity. The low rms error suggests that the model’s predictions are very close to the actual values and these results indicate a robust correlation between the input features used in the model and stellar luminosity. The model excluding mid-IR fluxes also demonstrates a strong performance with an  $R^2$  score of 0.944, in addition to the K-band model which scores 0.831. Using only bp and rp fluxes results under-performed with an  $R^2$  score of 0.661 and a marginally higher rms error of 0.090 and is therefore less effective at making accurate luminosity predictions.

#### 4.2.4 Luminosity from reduced datasets

In this section, we re-test the accuracy of our model on a reduced dataset for luminosity prediction. The same tests are performed for luminosity as done previously for mass loss, where firstly the mid-IR photometry is removed and the model only uses optical and near-IR features, then only optical features and finally only K-band.

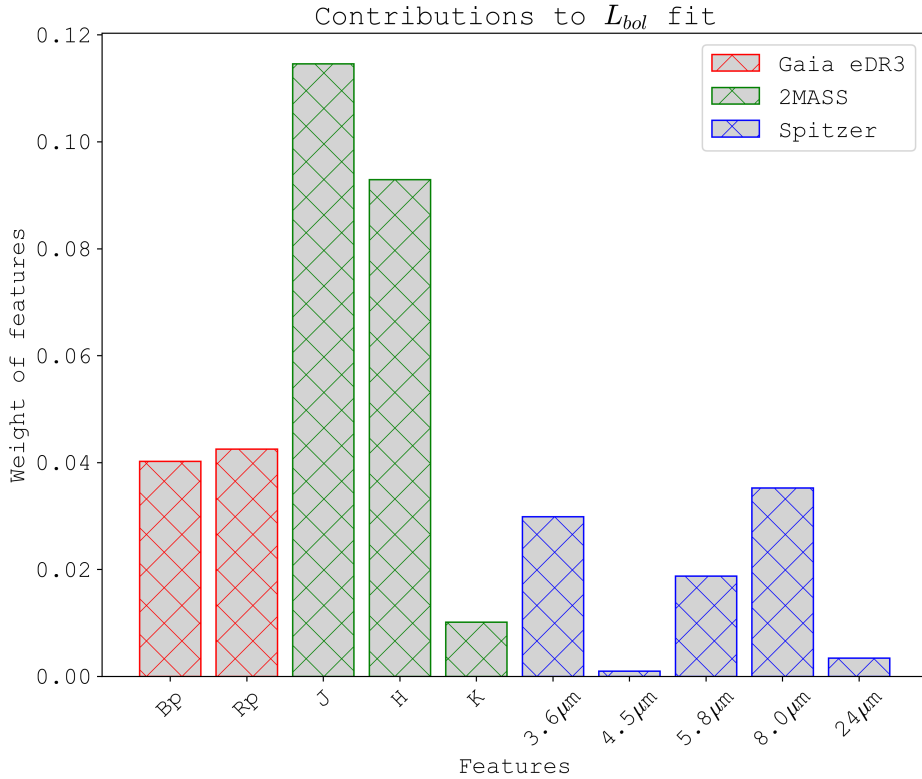


FIGURE 4.6: Same as Figure 4.3 but with the target value now being  $L_{bol}$ .

Figure 4.7 shows the linear regression plots for each of these reduced datasets used. Both the omitted mid-IR and K-band only models were found to accurately predict luminosity from these features, with  $R^2$  scores of 0.944 and 0.831, respectively. Whereas again, using only the optical bp and rp bands has difficulty reproducing luminosities as well as when using the other features. Table 4.2 shows the full set of results for each test.

### 4.3 Deployment and evaluation of the model performance on M33 red supergiant photometry

In the previous sections, it has been established that a linear regression model can be used to make accurate predictions for the mass loss rates and luminosities of RSGs. The next step is to implement this model onto unseen data to further test the performance. To do so, we use photometric fluxes of RSGs in local group galaxy, M33. The adopted distance to M33 used in the present work is 840 kpc (distance modulus =  $24.64 \pm 0.09$ ) from [Freedman et al. \(1991\)](#), based on measurements using Cepheid Variables. The sample of M33 RSGs and  $A_v$  extinction values used are taken from [Massey et al.](#)

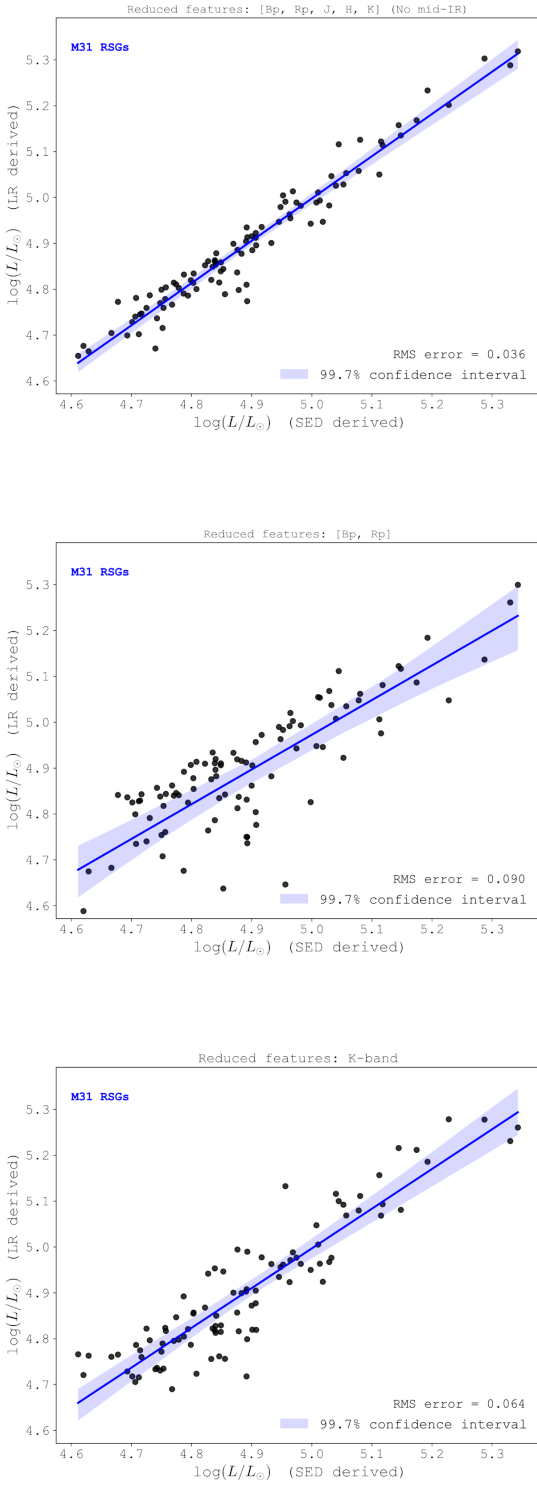


FIGURE 4.7: Same as Figure 4.5 but this time with the model trained on reduced features. In the top panel, the model is trained only on Gaia bp and rp and 2MASS J,H and K bands and the middle panel shows the model trained solely on Gaia bp and rp bands, and the bottom panel shows the results of the model trained only on the K-band.

Features used in the model				
	All features	No mid-IR bands	Only bp and rp	Only K-band
<b>M predictions:</b> <b>LF = MSE</b>	rms error = 0.144 $R^2$ score = 0.931	rms error = 0.517 $R^2$ score = 0.113	rms error = 0.516 $R^2$ score = 0.116	rms error = 0.522 $R^2$ score = 0.058
<b>M predictions:</b> <b>LF = Huber</b>	rms error = 0.150 $R^2$ score = 0.924	rms error = 0.527 $R^2$ score = 0.077	rms error = 0.531 $R^2$ score = 0.064	rms error = 0.534 $R^2$ score = 0.054
<b>M predictions:</b> <b>LF = epsilon insensitive</b>	rms error = 0.108 $R^2$ score = 0.960	rms error = 0.534 $R^2$ score = 0.054	rms error = 0.525 $R^2$ score = 0.086	rms error = 0.535 $R^2$ score = 0.048
<b><math>L_{bol}</math> predictions:</b> <b>LF = MSE</b>	rms error = 0.031 $R^2$ score = 0.955	rms error = 0.036 $R^2$ score = 0.944	rms error = 0.090 $R^2$ score = 0.661	rms error = 0.064 $R^2$ score = 0.831
<b><math>L_{bol}</math> predictions:</b> <b>LF = Huber</b>	rms error = 0.032 $R^2$ score = 0.956	rms error = 0.036 $R^2$ score = 0.945	rms error = 0.094 $R^2$ score = 0.634	rms error = 0.063 $R^2$ score = 0.836
<b><math>L_{bol}</math> predictions:</b> <b>LF = epsilon insensitive</b>	rms error = 0.044 $R^2$ score = 0.918	rms error = 0.045 $R^2$ score = 0.914	rms error = 0.089 $R^2$ score = 0.668	rms error = 0.066 $R^2$ score = 0.820

TABLE 4.2: The results of varying the loss function of the linear regression model on the chosen evaluation metrics.

(2021, 2023) (we adopt the same method as Chapter 2 where our M33 photometry is de-reddened according to the Cardelli et al. (1989) reddening law for the optical photometry, and Rieke & Lebofsky (1985) for the near-IR), which has been reduced to a sample of 171 RSGs which are either confirmed RSGs or RSG candidates and have full photometric coverage needed for the model, so consistent feature usage can be ensured. The sample data is then pre-processed so that the M33 data matches the format of the training data. This is achieved by collating and cross matching Gaia bp and rp magnitudes, 2MASS JHK and Spitzer IRAC and MIPS1 (Khan et al., 2015), which are then converted to fluxes using the magnitude-flux equation.

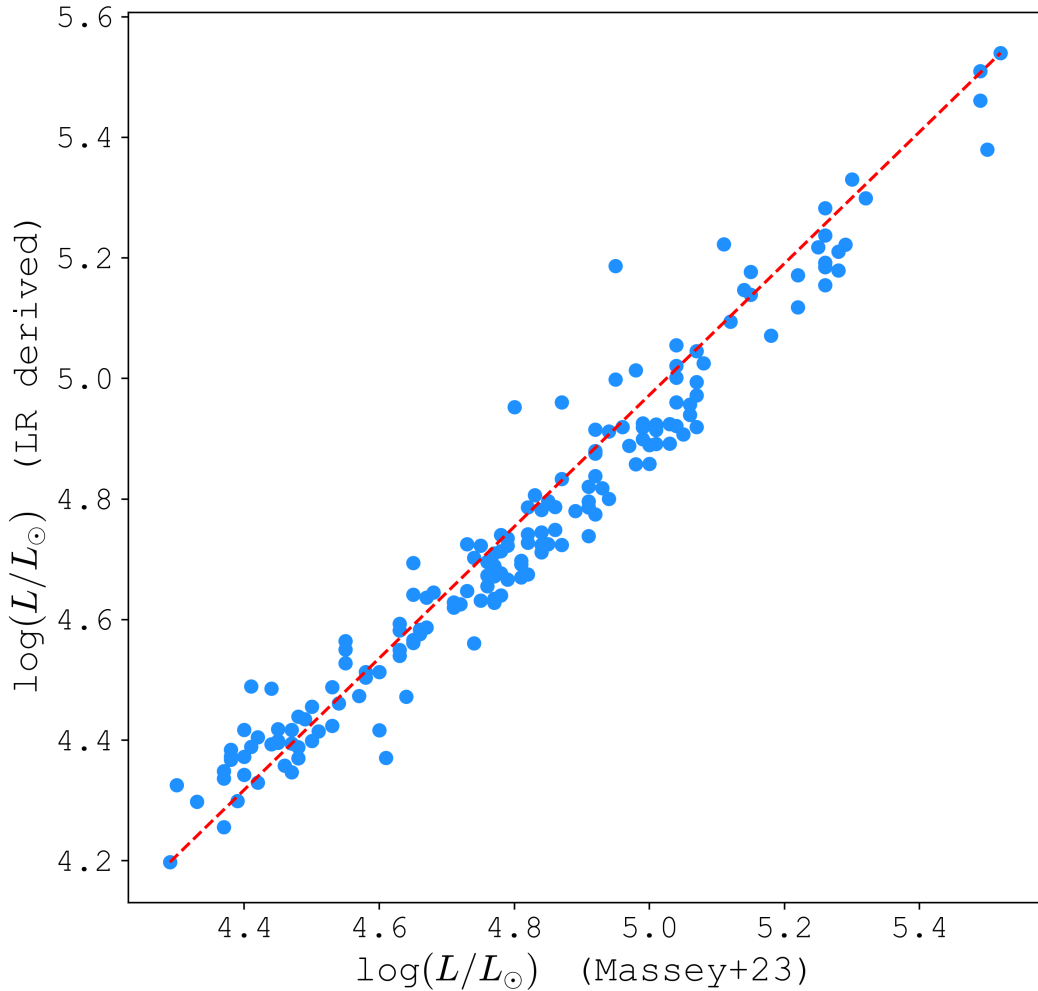


FIGURE 4.8: Comparison of bolometric luminosities of M33 RSGs from the linear regression model and those from Massey et al. (2023) determined using a K-band bolometric correction ( $BC_K$ ).

### 4.3.1 M33 RSG luminosity predictions

#### 4.3.1.1 The Humphreys-Davidson limit for M33 red supergiants

In this section, we explore the results of implementing our model to a sample of M33 RSG photometry to determine their luminosities. Figure 4.9 shows a histogram of the M33 RSG luminosities. It shows a sharp cliff-edge to the distribution, which is expected due to the hard upper limit to RSG luminosity. We have a smaller sample size of M33 RSGs compared to M31 as we include solely spectroscopically confirmed M33 RSGs to

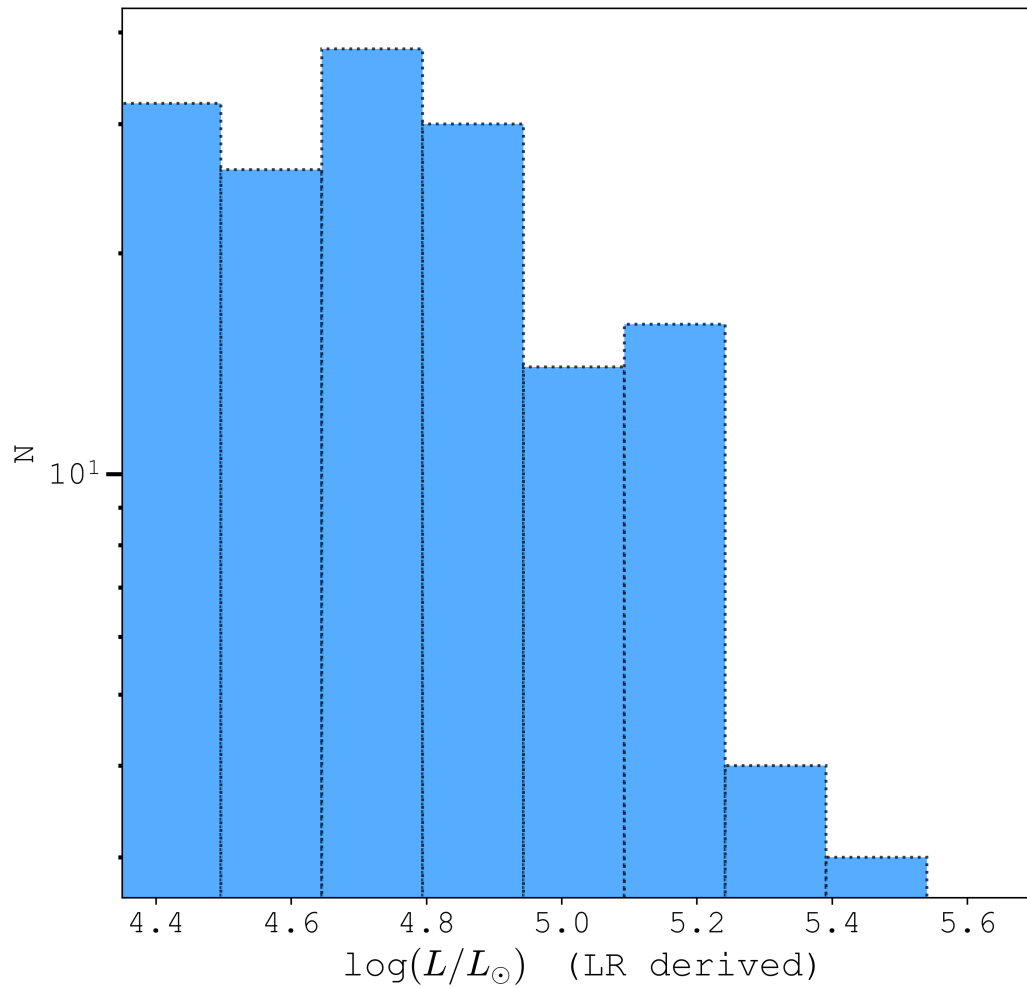


FIGURE 4.9: Luminosity distribution of the 171 M33 RSGs, with luminosities predicted using a linear regression model.

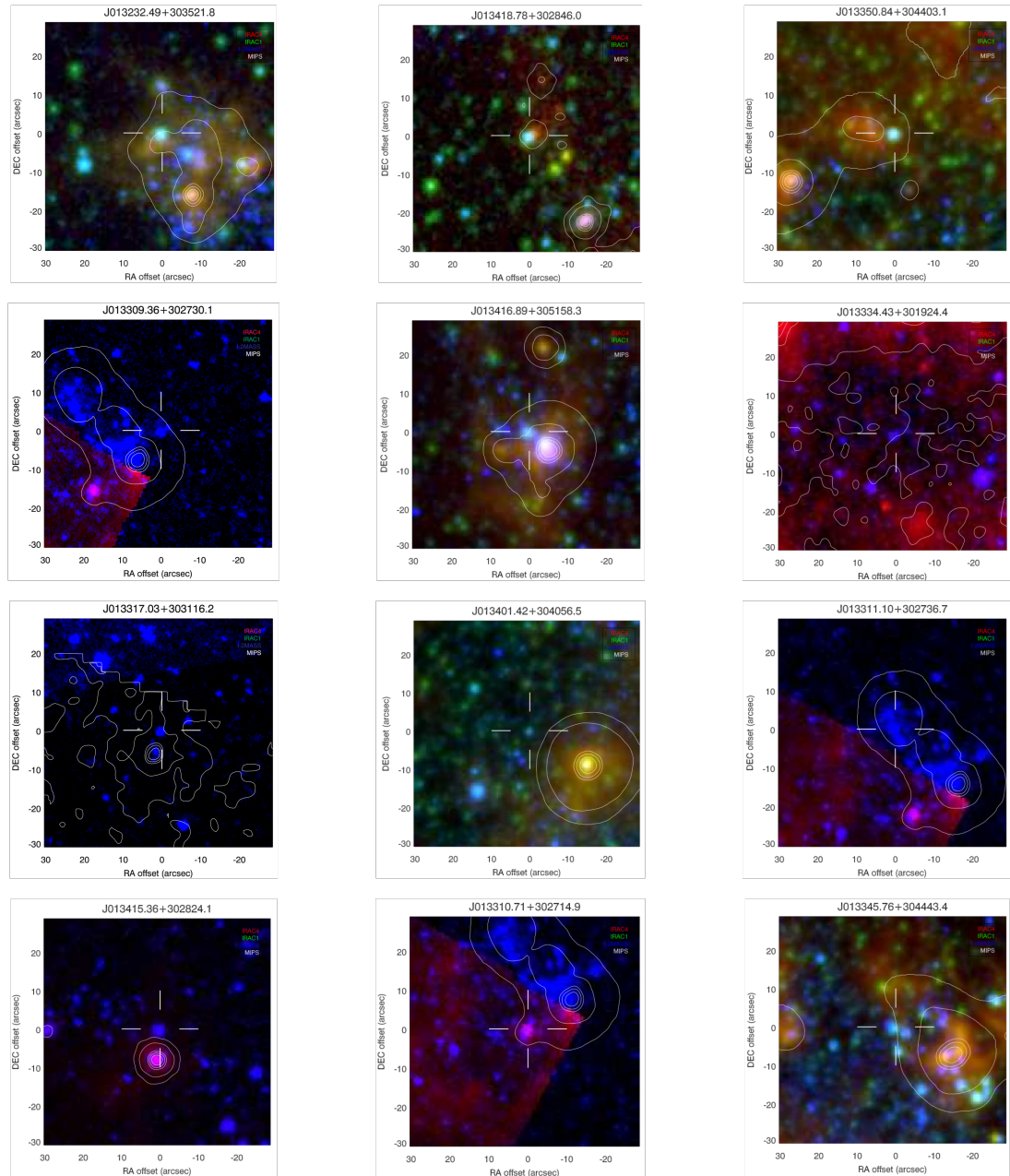


FIGURE 4.10: RGB images of the highest mass loss rate M33 RSGs in the sample, showing the offset between sources.

avoid any contamination of the luminosity function (the RSGs used here also all appear in the sample of M33 RSGs used in [Ren et al. \(2021b\)](#)) which also contributes to this sharp drop off of the number of high luminosity objects higher than  $L_{\text{bol}} \sim 5.2$ . We observe a clear absence of RSGs with a luminosity greater than  $L_{\text{bol}} \sim 5.5$  with our highest luminosity object being  $L_{\text{bol}} = 5.54 \pm 0.09$ . This is consistent with the HD limit found for M31 RSGs in Chapter 2 as well as more recent work into the HD limit by [Massey et al. \(2023\)](#). M33 is known to have a metallicity gradient which decreases with increasing radius ([Searle, 1971](#); [Cioni, 2009](#)), ranging from  $Z \sim 1.0$  in the inner regions of M33, to  $Z \sim 0.3$  in the outer regions ([Neugent et al., 2021](#)). This further solidifies the result in Chapter 2 that the HD limit is independent of metallicity.

### 4.3.2 Comparison to previous M33 RSG luminosities: Massey et al. (2021,2023)

In [Massey et al. \(2021, 2023\)](#), they determine bolometric luminosities of their sample of M33 RSGs using a  $BC_K$ . Figure 4.8 shows a comparison of the luminosities determined previously with our linear regression model to those determined by Massey et al. We see that the model finds slightly higher luminosities for a few stars with luminosities between  $L_{\text{bol}} = 4.9 - 5.2$  compared to the Massey sample, overall they show a strong correlation, with an rms error of 0.09.

### 4.3.3 M33 RSG mass loss predictions

In this section, we look at implementing the model to calculate  $\dot{M}$  of the red supergiants in M33. Figure 4.12 shows the mass loss results plotted as a function of bolometric luminosity, determined previously in Section 4.3.1. We see a number of objects with mass loss rates above the threshold for potentially being superwind objects. These high mass loss rate objects would make our results more consistent with those from [Wang et al. \(2021\)](#), who find some M33 RSGs with mass loss rates as high as  $\sim 10^{-4} M_{\odot} \text{yr}^{-1}$ . However, a closer look at the objects by examining their RGB images, following the same approach as in Chapter 3 for M31 the M31 RSGs, show that the [Khan et al. \(2015\)](#)  $24\mu\text{m}$  source appears to be offset from the optical source in the images, with all 17 objects seen above  $10^{-5} M_{\odot} \text{yr}^{-1}$  displaying this offset. The  $24\mu\text{m}$  flux coming from such a large area is resulting in a large over-prediction of the overall mass loss rate which is why we are getting these objects in the superwind region in  $\dot{M}-L_{\text{bol}}$  space.

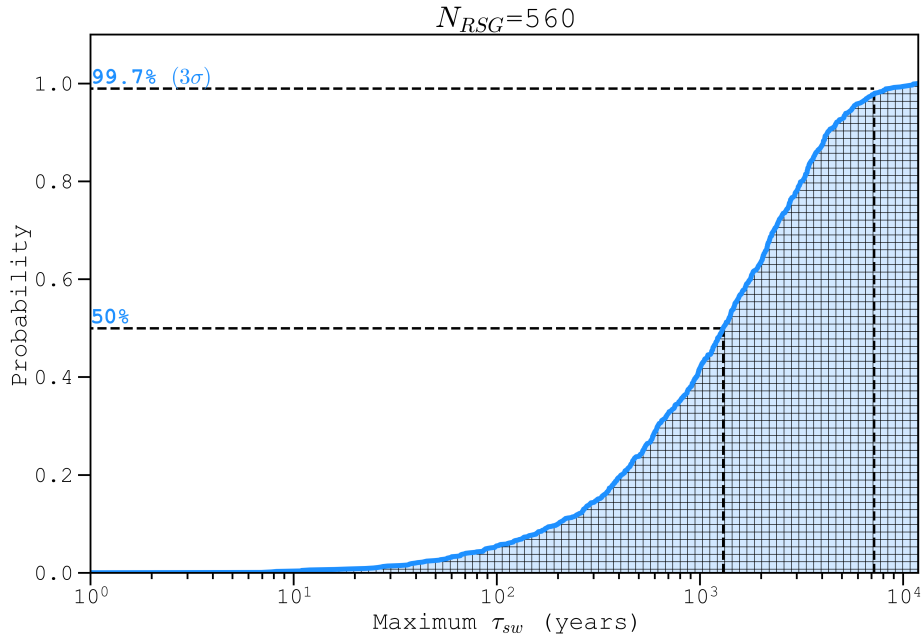


FIGURE 4.11: A cumulative distribution, similar to Figure 3.7, with updated Monte Carlo results, now including the 171 M33 RSGs to the sample, bringing to the total number of RSGs used in the experiment to  $N_{RSG}=560$ .

When considering the M33 RSGs as well as the M31 RSG sample, we now have over 500 objects with none of them showing any evidence of experiencing a super-wind phase. In Chapter 3, we saw in results of the Monte Carlo experiment in Figure 3.7 that we can exclude a superwind phase lasting longer than  $\sim 10,000$  years at the  $3\sigma$  confidence interval. Now with the added M33 RSGs increasing our sample size, that timescale decreases even further to 7000 years, see Figure 4.11, which would require the minimum  $\dot{M}$  to be in excess of  $\sim 10^{-3}M_{\odot}yr^{-1}$  if the objects are spending  $<1\%$  of their lifetime in a super-wind phase, but we again do not observe any RSGs in this work with mass loss rates close as high as this. This is further evidence for the argument that because the only processes known to remove substantial amounts of mass from in short timescales are binary interactions and LBV-type eruptions, in order to form stripped-envelope stars, both main sequence and RSG winds are just not significant enough to form these stars from single-star pathways.

#### 4.4 Summary and future work

In this work, we have successfully deployed a linear regression machine model to predict the mass loss rates and luminosities of RSGs in M33 in a low cost manner. We found that

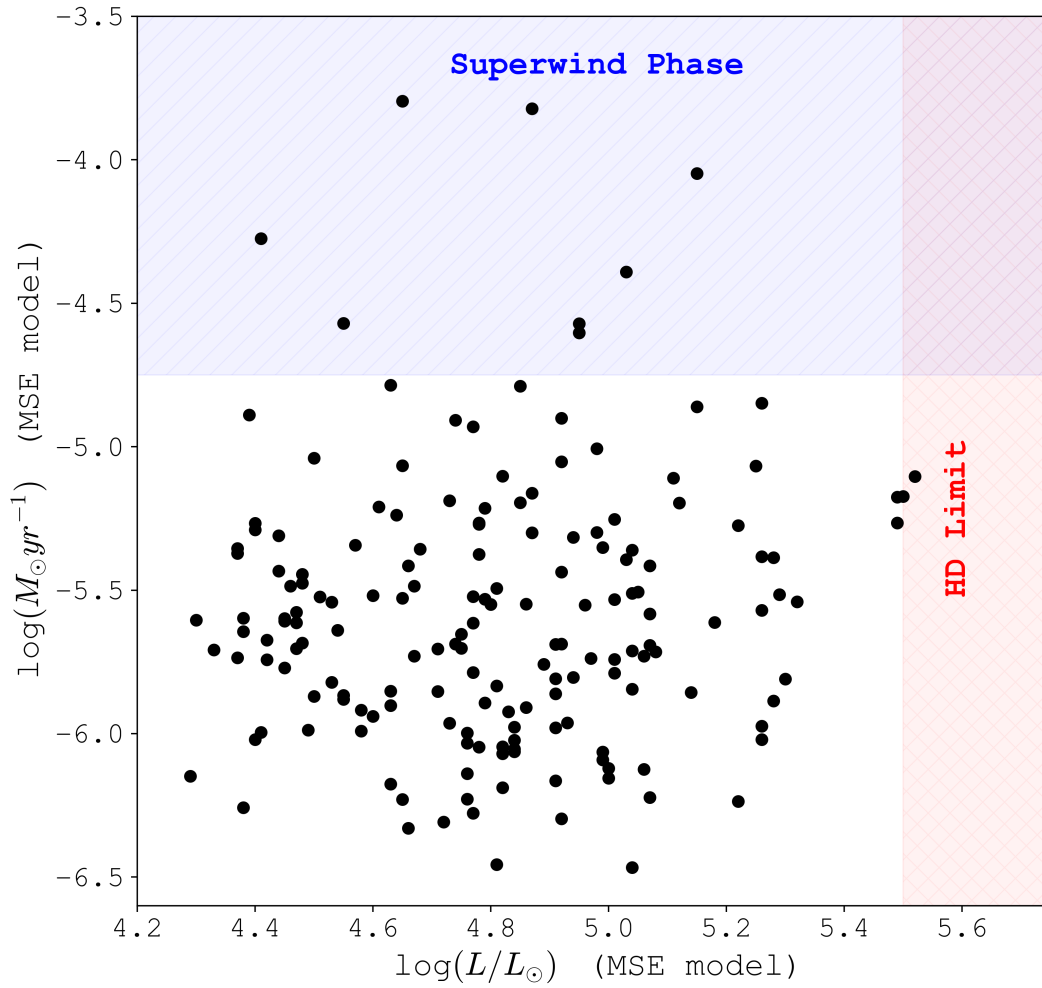


FIGURE 4.12: The model predicted  $\dot{M}$  vs  $L_{\text{bol}}$  for M33 RSGs with the shaded regions indicating the Humphreys-Davidson limit (red) and the region of a possible superwind phase (blue).

our best results came from using a model containing magnitudes from wavelengths from optical, near-IR and mid-IR and reducing the number of features to just optical and/or near-IR greatly increased the RMS error. We found the HD limit to be  $L_{bol}=5.54\pm 0.09$ , consistent with the limit found for M31 RSGs in Chapter 2. This method for determining luminosity could prove to be a useful tool for HD limit studies of large datasets for other Local Group galaxies. Furthermore, the model determined  $\dot{M}$  for 171 confirmed RSGs in M33. Zero superwind candidates were found, despite a few objects with seemingly high mass loss rates at first glance. Their RGB images showed that the  $24\mu\text{m}$  source was offset from the optical sources, like in the M31 study, which resulted in an over-prediction of the mass loss rates of these object. To summarise, in this section we have obtained a way to rapidly scale-up the study from Section 3 by producing a linear regression model which can accurately determine  $\dot{M}$  and  $L_{bol}$  from observational fluxes. This has allowed us to make an estimate of the HD-limit for M33 RSGs as well as and put even tighter constraints on the mass loss rate and timescales of the super-wind phase by increasing our sample size to include M33 RSGs.

## Chapter 5

# Summary & Conclusions

The aim of this thesis is to address some of the unresolved problems in massive stellar evolution and help bridge the gap between the RSG phase and supernova explosion, described in Section 1. Having a better understanding of RSG luminosity and mass loss rates will enhance the accuracy of predictions from stellar evolution models, strengthening our understanding of massive stellar evolution.

The first aim of this thesis is investigate the HD limit of M31 RSGs, which is explored in Chapter 2. The upper luminosity limit for RSGs defines the boundary between evolutionary channels of massive stars that end their lives as either type II SNe, or stripped-envelope type Ib/c SNe. This limit has been commonly explained as being a manifestation of mass loss during the lifetime of the star, caused by strong stellar winds or episodic periods of mass-loss. Under this assumption, the HD limit should be higher at lower metallicity, where weaker mass-loss rates mean that higher initial masses are required for an envelope to be stripped.

There has already been studies of the HD limit in the literature, firstly in [Humphreys & Davidson \(1979\)](#) where the first measurement of the upper limit was found to be  $\log(L/L_{\odot}) = 5.8 \pm 0.1$ , using an optically selected sample of cool supergiants in the Milky Way and the LMC (this was later revised to  $\log(L/L_{\odot}) = 5.66$  in [Humphreys \(1983\)](#)). However, when this was revisited in [Davies, Crowther & Beasor \(2018\)](#), for the Magellanic Clouds, this time with more complete samples and higher precision multi-wavelength photometry, an upper limit of  $\log(L/L_{\odot}) = 5.5$  for both the Small Magellanic Cloud (SMC) and the LMC was determined. The fact the metallicity of the

LMC is roughly twice that of the SMC is important as its the first indication of a possible metallicity independent HD limit. The consequence of a metallicity independent upper limit is that line-driven winds cannot be responsible. We therefore explored this further by measuring the luminosity function of RSGs in M31 and comparing to those in the LMC and SMC. We find that  $\log(L_{\max}/L_{\odot}) = 5.53 \pm 0.03$  in M31 ( $Z \gtrsim Z_{\odot}$ ), consistent with the limit found for both the LMC ( $Z \sim 0.5 Z_{\odot}$ ) and SMC ( $Z \sim 0.25 Z_{\odot}$ ), while the RSG luminosity distributions in these 3 galaxies are consistent to within  $1\sigma$ . Ultimately, we found no evidence to suggest a metallicity dependence on both the HD limit and the RSG luminosity function, and conclude that line-driven winds on the main sequence can not be the cause of the HD limit.

A metallicity independent HD limit means that the spotlight shifts towards binary mass transfer or high mass loss episode known as a 'superwind' phase, being a possible explanation for the stripping of stellar envelopes of massive stars resulting in the upper limit to RSG luminosity. There are recent studies (e.g. [Sana et al., 2012, 2013](#); [Dunstall et al., 2015](#)) which have concluded that the fraction of OB stars in binary systems are in the range of 50-60% or higher and the probability of a star being in a multiple, *and* that the star will interact with this companion, appears to increase with increasing mass (see, [Duchêne & Kraus, 2013](#); [Moe & Di Stefano, 2017](#); [Bodensteiner et al., 2021](#)). This means we would expect binary effects to also be contributing to the mass lost during a star's life and is therefore a possible explanation for the reduced  $L_{\max}$  we see in observations.

In Chapter 3, we had a fresh look at the mass loss rates of M31 RSGs, with the purpose of exploring whether any of these RSGs are experiencing a superwind phase. Mass loss rates of cool massive stars are already being found to be much lower than previously thought (see, [Beasor et al., 2020](#)) and only a very small percentage ( $\sim 3\%$ ) seem to be truly dust enshrouded, so looking at a large sample of M31 RSGs is our best chance at compiling an unbiased sample that catches RSGs in all  $\dot{M}$  phases, even the very brief ones. To do so, we used using DUSTY, the radiative transfer code to model the dust shells of the M31 RSGs in our sample to estimate their mass loss rates. We found none to have a high enough mass loss rate to be experiencing a superwind phase. In order to quantify the absence of superwind stars in terms of an upper limit to the length of any such phase, we employed two complementary numerical experiments. By using the MESA-MIST models to predict how high the superwind mass-loss rate would need to be for RSGs to lose their entire envelope in this phase as well as putting an upper limit on how long this phase would need to last to do so. As a result, we found that

we can exclude a superwind phase lasting longer than  $\sim 10,000$  years at the  $3\sigma$  confidence interval, with the minimum  $\dot{M}$  required to remove the envelope in this time being  $10^{-3}M_{\odot}yr^{-1}$ .

The fact we do not observe any RSGs with  $\dot{M}$  high enough to be in a superwind phase means that if the superwind phase is experienced by all RSGs, it would need to last  $< 1\%$  of the RSGs lifetime and  $\dot{M}$  would need to be  $> 1 \times 10^{-3}$  during that phase. The only processes known to remove mass at this rate are LBV type eruptions (e.g. Eta Carinae) or binary mass transfer. Winds do not appear capable of stripping material at this rate, with RSG winds only removing  $\sim 1 - 2M_{\odot}$  throughout their lifetime suggests that winds are not that important for massive stellar evolution, at least when concerning the evolution to WR stars/Ibc progenitors from single-star pathways.

The aim of Chapter 4 was to find a cheaper, efficient way to obtain luminosity and mass loss rates for large samples of RSGs. This could potentially enable similar studies as seen in Chapters 2 and 3 but on much larger samples across many more galaxies. For this reason, we use machine learning to find correlations between  $L_{bol}$  and  $\dot{M}$  a variety of observables, not limited to those which are used to fit physical models.

The linear regression model we trained on RSG fluxes was able to accurately predict M31 RSG mass loss rates and luminosities as well as be successfully deployed on unseen M33 RSG fluxes where it succeeded in estimating the same two parameters. Firstly, we determined a HD limit of  $L_{bol}=5.54\pm 0.09$ , which is consistent with the HD limit for M31, LMC and SMC. Secondly, we found zero RSGs with a mass loss rate high enough to be experiencing a superwind phase. Also, we increased our sample size of RSGs from Chapters 2 and 3 by including the M33 RSGs, which allowed us to put tighter constraints on the timescale of the super-wind phase, finding that a phase lasting longer than  $\sim 7000$  years could be excluded at the  $3\sigma$  confidence interval, meaning that RSGs would require a mass loss rate in excess of  $> 1 \times 10^{-3}$  to strip the envelope in this time. This machine learning method could prove to be useful for potentially identifying both superwind and high luminosity stars, which could then be the subject of any necessary follow-up observations. This would allow for galaxy-wide studies without galaxy-wide observations.

## 5.1 Future Work

### Red supergiants as distance indicators:

The benefits of using the brightest stars for distance measurements beyond the local group, was first proposed in [Hubble \(1936\)](#). However, a number of 'bright stars' used in this study were later revealed to be other objects such as HII regions or clusters, as discussed in [Sandage \(1958\)](#), skewing any galaxy distance measurements. In [Sandage & Tammann \(1974b\)](#), they showed a dependence of the luminosity of bright blue stars with on the luminosity of its host galaxy, with the most luminous blue stars found in the brightest galaxies. In contrast, they found the most luminous red stars exhibit essentially constant luminosity independent of the galaxy type. In both [Sandage \(1986\)](#) and [Humphreys \(1988\)](#), using luminous late-type supergiants (F to M spectral types) are suggested to make good candidates for distance indicators, with cool supergiants being more easily detectable than blue supergiants due to their extreme brightness in the infrared and minimal extinction. These studies coupled with the results of Chapter 2 which show the upper limit of RSG luminosity is independent of metallicity further supports the use of RSGs as distance indicators. For galaxies with uncertain distances, for example NGC 6946 known as the 'fireworks galaxy', a new method for determining distance could prove useful. Currently, the distance ranges from  $\sim 5.9$  Mpc ([Mould et al., 2000](#)), to further distances such as  $\sim 7.8 - 7.9$  Mpc ([Anand et al., 2018](#)) and  $7.9 \pm 4.0$  [Eldridge & Xiao \(2019\)](#). Methods for determining the distance vary, with [Mould et al. \(2000\)](#) and [Eldridge & Xiao \(2019\)](#) using SNe as well as ([Anand et al., 2018](#)) using the tip of the red giant branch (TRGB). This disparity in the distance has a knock on effect for any luminosity calculations where sources are 70% brighter when using the TRGB distance as well as an effect on the predictions of the progenitor mass estimates.

The IIP SNe in NGC 6946, e.g. SNe2002hh, 2004et and 2017eaw as a result have a range of masses/luminosities estimated for them as a consequence of the unconstrained distance. For both 2002hh and 2004et, an assumed distance of 5.9Mpc was used in both [Smartt \(2015\)](#) and [Davies & Beasor \(2018\)](#). It is shown in [Eldridge & Xiao \(2019\)](#), when using the updated distance of 7.72Mpc from [Anand et al. \(2018\)](#), its luminosity increases from  $L_{\text{bol}} < 5.55$  to  $L_{\text{bol}} < 5.78$  making it greater than the empirical measurements of the HD limit. Both 2004et and 2017eaw also see increases to their luminosities when using this greater distance, which therefore results in a larger initial mass estimate for them too. This could change the current views on the RSG problem, and change the

mass boundaries with respect to upper mass cutoff for RSG SN progenitors.

To use RSGs as a distance indicator for NGC 6946, a machine learning model like the one used in Chapter 4 can be utilised, alongside archival Gaia and/or Hubble Space Telescope photometry which can be converted to fluxes and used as features for the model. Once a sample of RSGs is established, the luminosity distribution can be obtained from the model along with the apparent HD limit. Follow up spectroscopy may likely be required for the stars around the HD limit to confirm where it is, but assuming the HD limit is  $L_{\text{bol}}=5.5$ , a distance can be obtained.

# Bibliography

- Adams S. M., Kochanek C. S., Gerke J. R., Stanek K. Z., Dai X., 2017, [MNRAS](#), **468**, 4968
- Anand G. S., Rizzi L., Tully R. B., 2018, [AJ](#), **156**, 105
- Arroyo-Torres B., et al., 2015, [A&A](#), **575**, A50
- Azimlu M., Marciniak R., Barmby P., 2011, [AJ](#), **142**, 139
- Beasor E. R., Davies B., 2016, [MNRAS](#), **463**, 1269
- Beasor E. R., Smith N., 2022, [ApJ](#), **933**, 41
- Beasor E. R., Davies B., Smith N., van Loon J. T., Gehrz R. D., Figer D. F., 2020, [MNRAS](#), **492**, 5994
- Beasor E. R., Davies B., Smith N., 2021, [ApJ](#), **922**, 55
- Björklund R., Sundqvist J. O., Puls J., Najjarro F., 2021, [A&A](#), **648**, A36
- Boch T., Fernique P., 2014a, in Manset N., Forshay P., eds, *Astronomical Society of the Pacific Conference Series Vol. 485, Astronomical Data Analysis Software and Systems XXIII*. p. 277
- Boch T., Fernique P., 2014b, in Manset N., Forshay P., eds, *Astronomical Society of the Pacific Conference Series Vol. 485, Astronomical Data Analysis Software and Systems XXIII*. p. 277
- Bodensteiner J., et al., 2021, arXiv e-prints, p. [arXiv:2104.13409](#)
- Bowers P. F., Johnston K. J., Spencer J. H., 1983, [ApJ](#), **274**, 733
- Bruch R. J., et al., 2021, [ApJ](#), **912**, 46
- Brunish W. M., Gallagher J. S., Truran J. W., 1986, [AJ](#), **91**, 598

- Buchanan C. L., Kastner J. H., Forrest W. J., Hrivnak B. J., Sahai R., Egan M., Frank A., Barnbaum C., 2006, *AJ*, **132**, 1890
- Caldwell N., Harding P., Morrison H., Rose J. A., Schiavon R., Kriessler J., 2009, *AJ*, **137**, 94
- Cannon E., et al., 2023, *A&A*, **675**, A46
- Cardelli J. A., Clayton G. C., Mathis J. S., 1989, *ApJ*, **345**, 245
- Castor J. I., Abbott D. C., Klein R. I., 1975, *ApJ*, **195**, 157
- Chiosi C., Maeder A., 1986, *ARA&A*, **24**, 329
- Cioni M. R. L., 2009, *A&A*, **506**, 1137
- Conti P., 1976, *PASJ*, **9**, 193
- Conti P. S., McCray R., 1980, *Science*, **208**, 9
- Courteau S., Widrow L. M., McDonald M., Guhathakurta P., Gilbert K. M., Zhu Y., Beaton R. L., Majewski S. R., 2011, *ApJ*, **739**, 20
- Crowther P. A., 2001, in Vanbeveren D., ed., *Astrophysics and Space Science Library* Vol. 264, *The Influence of Binaries on Stellar Population Studies*. p. 215 ([arXiv:astro-ph/0010581](https://arxiv.org/abs/astro-ph/0010581)), doi:10.1007/978-94-015-9723-4\_17
- Cutri R. M., et al., 2003, *VizieR Online Data Catalog*, p. II/246
- Dalcanton J. J., et al., 2012, *ApJS*, **200**, 18
- Dalcanton J. J., et al., 2015, *ApJ*, **814**, 3
- Davies B., Beasor E. R., 2018, *MNRAS*, **474**, 2116
- Davies B., Beasor E. R., 2020, *MNRAS*, **493**, 468
- Davies, Crowther & Beasor 2018, *MNRAS*, **478**, 3138
- Davies B., et al., 2013, *ApJ*, **767**, 3
- De Beck E., Decin L., de Koter A., Justtanont K., Verhoelst T., Kemper F., Menten K. M., 2010, *A&A*, **523**, A18
- Decin L., Hony S., de Koter A., Justtanont K., Tielens A. G. G. M., Waters L. B. F. M., 2006, *A&A*, **456**, 549
- Deutsch A. J., 1956, *ApJ*, **123**, 210

- Draine B. T., Lee H. M., 1984, *ApJ*, 285, 89
- Duchêne G., Kraus A., 2013, *ARA&A*, 51, 269
- Dunstall P. R., et al., 2015, *A&A*, 580, A93
- Ekström S., et al., 2012, *A&A*, 537, A146
- Eldridge J. J., Xiao L., 2019, *MNRAS*, 485, L58
- Farrell E. J., Groh J. H., Meynet G., Eldridge J. J., Ekström S., Georgy C., 2020, *MNRAS*, 495, 4659
- Farrell E., Groh J. H., Meynet G., Eldridge J. J., 2022, *MNRAS*, 512, 4116
- Fazio G. G., et al., 2004, *ApJS*, 154, 10
- Ferrari A., Galeotti P., Silvestro G., Trussoni E., 1970, *Ap&SS*, 9, 181
- Freedman W. L., Wilson C. D., Madore B. F., 1991, *ApJ*, 372, 455
- Fremling C., et al., 2016, *A&A*, 593, A68
- Fryer C. L., 1999, *ApJ*, 522, 413
- Gaia Collaboration 2020, VizieR Online Data Catalog, p. I/350
- Gehrz R. D., Woolf N. J., 1971, *ApJ*, 165, 285
- Georgy C., et al., 2013a, *A&A*, 558, A103
- Georgy C., et al., 2013b, *A&A*, 558, A103
- Gilmozzi R., et al., 1987, *Nature*, 328, 318
- Goldman S. R., et al., 2017, *MNRAS*, 465, 403
- Gordon K. D., et al., 2006, *ApJl*, 638, L87
- Gordon M. S., Humphreys R. M., Jones T. J., 2016, *ApJ*, 825, 50
- Groenewegen M. A. T., 1994, *A&A*, 290, 531
- Groenewegen M. A. T., Sloan G. C., Soszyński I., Petersen E. A., 2009, *A&A*, 506, 1277
- Gustafsson B., Edvardsson B., Eriksson K., Jørgensen U. G., Nordlund Å., Plez B., 2008, *A&A*, 486, 951
- Harper G. M., Brown A., Lim J., 2001, *ApJ*, 551, 1073

- Hayashi C., Hoshi R., 1961, *PASJ*, **13**, 442
- Heger A., Fryer C. L., Woosley S. E., Langer N., Hartmann D. H., 2003, *ApJ*, **591**, 288
- Hoefner S., Dorfi E. A., 1997, *A&A*, **319**, 648
- Höfner S., Olofsson H., 2018, *A&A Rev.*, **26**, 1
- Hubble E., 1936, *ApJ*, **84**, 270
- Humphreys R. M., 1983, *ApJ*, **265**, 176
- Humphreys R. M., 1988, in van den Bergh S., Pritchett C. J., eds, *Astronomical Society of the Pacific Conference Series Vol. 4, The Extragalactic Distance Scale*. pp 103–112
- Humphreys R. M., Davidson K., 1979, *ApJ*, **232**, 409
- Humphreys R. M., Lockwood G. W., 1972, *ApJL*, **172**, L59
- Höfner S., 2008, *Astronomy & Astrophysics - ASTRON ASTROPHYS*, 491
- Ivezic Z., Nenkova M., Elitzur M., 1999, *DUSTY: Radiation transport in a dusty environment*, *Astrophysics Source Code Library*, record ascl:9911.001 (ascl:9911.001)
- Josselin E., Plez B., 2007, *A&A*, **469**, 671
- Kang Y., Rey S.-C., Bianchi L., Lee K., Kim Y., Sohn S. T., 2012, *ApJS*, **199**, 37
- Karachentsev I. D., Karachentseva V. E., Huchtmeier W. K., Makarov D. I., 2004, *AJ*, **127**, 2031
- Kee N. D., Sundqvist J. O., Decin L., de Koter A., Sana H., 2021, *A&A*, **646**, A180
- Kennicutt Robert C. J., Lee J. C., Funes J. G., J. S., Sakai S., Akiyama S., 2008, *ApJS*, **178**, 247
- Khan R., 2017, *ApJS*, **228**, 5
- Khan R., Stanek K. Z., Kochanek C. S., Sonneborn G., 2015, *VizieR Online Data Catalog*, p. [J/ApJS/219/42](#)
- Knapp G. R., Phillips T. G., Leighton R. B., Lo K. Y., Wannier P. G., Wootten H. A., Huggins P. J., 1982, *ApJ*, **252**, 616
- Kobulnicky H. A., et al., 2014, *ApJS*, **213**, 34
- Kochanek C. S., Beacom J. F., Kistler M. D., Prieto J. L., Stanek K. Z., Thompson T. A., Yüksel H., 2008, *ApJ*, **684**, 1336

- Kochanek C. S., Adams S. M., Belczynski K., 2014, *MNRAS*, **443**, 1319
- Kraus M., Oksala M. E., Cidale L. S., Arias M. L., Torres A. F., Borges Fernandes M., 2015, *ApJL*, **800**, L20
- Lamb S. A., Iben I. J., Howard W. M., 1976, *ApJ*, **207**, 209
- Langer N., Heger A., 1999, in Chu Y. H., Suntzeff N., Hesser J., Bohlender D., eds, 1 Vol. 190, *New Views of the Magellanic Clouds*. p. 192
- Li S., Riess A. G., Busch M. P., Casertano S., Macri L. M., Yuan W., 2021, *ApJ*, **920**, 84
- Maeder A., 1981, *A&A*, **102**, 401
- Maeder A., Meynet G., 2000, *A&A*, **361**, 159
- Maeder A., Meynet G., 2003, in van der Hucht K., Herrero A., Esteban C., eds, *IAU Symposium Vol. 212, A Massive Star Odyssey: From Main Sequence to Supernova*. p. 267
- Marshall J. R., van Loon J. T., Matsuura M., Wood P. R., Zijlstra A. A., Whitelock P. A., 2004, *MNRAS*, **355**, 1348
- Massey P., 2013, , **57**, 14
- Massey P., Evans K. A., 2016, *ApJ*, **826**, 224
- Massey P., Olsen K. A., Hodge P. W., Jacoby G. H., McNeill R. T., Smith R. C., Strong S. B., 2006, in *American Astronomical Society Meeting Abstracts*. p. 27.01
- Massey P., Silva D. R., Levesque E. M., Plez B., Olsen K. A. G., Clayton G. C., Meynet G., Maeder A., 2009, *ApJ*, **703**, 420
- Massey P., Neugent K. F., Smart B. M., 2016, *AJ*, **152**, 62
- Massey P., Neugent K. F., Levesque E. M., Drout M. R., Courteau S., 2021, *AJ*, **161**, 79
- Massey P., Neugent K. F., Ekström S., Georgy C., Meynet G., 2023, *ApJ*, **942**, 69
- Matsuura M., et al., 2016, *MNRAS*, **462**, 2995
- Maund J. R., Smartt S. J., 2005, *MNRAS*, **360**, 288
- Mauron N., Josselin E., 2011, *A&A*, **526**, A156

- Meynet G., et al., 2015, *A&A*, **575**, A60
- Moe M., Di Stefano R., 2017, *ApJS*, **230**, 15
- Moriya T. J., Yoon S.-C., Gräfener G., Blinnikov S. I., 2017, *MNRAS*, **469**, L108
- Morozova V., Piro A. L., Renzo M., Ott C. D., Clausen D., Couch S. M., Ellis J., Roberts L. F., 2015, *ApJ*, **814**, 63
- Morozova V., Piro A. L., Valenti S., 2017, *ApJ*, **838**, 28
- Mould J. R., et al., 2000, *ApJ*, **529**, 786
- Mould J., Barmby P., Gordon K., Willner S. P., Ashby M. L. N., Gehrz R. D., Humphreys R., Woodward C. E., 2008, *ApJ*, **687**, 230
- Neugent K. F., Massey P., Georgy C., Drout M. R., Mommert M., Levesque E. M., Meynet G., Ekström S., 2020, *ApJ*, **889**, 44
- Neugent et al. K. F., 2021, *ApJ*, **908**, 87
- Nieuwenhuijzen H., de Jager C., 1990, *A&A*, **231**, 134
- Ochsenbein F., Bauer P., Marcout J., 2000, *A&AS*, **143**, 23
- Patrick L. R., Evans C. J., Davies B., Kudritzki R. P., Hénault-Brunet V., Bastian N., Lapenna E., Bergemann M., 2016, *MNRAS*, **458**, 3968
- Paxton B., Bildsten L., Dotter A., Herwig F., Lesaffre P., Timmes F., 2011a, *ApJS*, **192**, 3
- Paxton B., Bildsten L., Dotter A., Herwig F., Lesaffre P., Timmes F., 2011b, *ApJS*, **192**, 3
- Plez B., 2012, Turbospectrum: Code for spectral synthesis, Astrophysics Source Code Library, record ascl:1205.004 (ascl:1205.004)
- Podsiadlowski P., 1992, *PASP*, **104**, 717
- Podsiadlowski P., Joss P. C., Rappaport S., 1990, *A&A*, **227**, L9
- Rahman M., Ménard B., Scranton R., 2016, *MNRAS*, **457**, 3912
- Rau G., Nielsen K. E., Carpenter K. G., Airapetian V., 2018, *ApJ*, **869**, 1
- Rau G., et al., 2019, *BAAS*, **51**, 241
- Reed B. C., 2003, *AJ*, **125**, 2531

- Reimers D., 1975, *Memoires of the Societe Royale des Sciences de Liege*, **8**, 369
- Ren Y., Jiang B., Yang M., Wang T., Jian M., Ren T., 2021a, *ApJ*, **907**, 18
- Ren Y., Jiang B., Yang M., Wang T., Jian M., Ren T., 2021b, *ApJ*, **907**, 18
- Rieke G. H., Lebofsky M. J., 1985, *ApJ*, **288**, 618
- Rieke G. H., et al., 2004, *ApJS*, **154**, 25
- Rodrigo C., Solano E., 2020, in *Contributions to the XIV.0 Scientific Meeting (virtual) of the Spanish Astronomical Society*. p. 182
- Russell S. C., Dopita M. A., 1990, *ApJS*, **74**, 93
- Saio H., Kato M., Nomoto K., 1988, *ApJ*, **331**, 388
- Salomon J. B., Ibata R., Reylé C., Famaey B., Libeskind N. I., McConnachie A. W., Hoffman Y., 2020, arXiv e-prints, p. [arXiv:2012.09204](https://arxiv.org/abs/2012.09204)
- Sana H., et al., 2012, *Science*, **337**, 444
- Sana H., et al., 2013, *A&A*, **550**, A107
- Sandage A., 1958, *ApJ*, **127**, 513
- Sandage A., 1986, in De Loore C. W. H., Willis A. J., Laskarides P., eds, Vol. 116, *Luminous Stars and Associations in Galaxies*. pp 31–39
- Sandage A., Tammann G. A., 1974a, *ApJ*, **191**, 603
- Sandage A., Tammann G. A., 1974b, *ApJ*, **191**, 603
- Schöier F. L., Olofsson H., 2001, *A&A*, **368**, 969
- Schutte W. A., Tielens A. G. G. M., 1989, *ApJ*, **343**, 369
- Scicluna P., Siebenmorgen R., Wesson R., Blommaert J. A. D. L., Kasper M., Voshchinnikov N. V., Wolf S., 2015, *A&A*, **584**, L10
- Searle L., 1971, *ApJ*, **168**, 327
- Shenoy D., et al., 2016, *AJ*, **151**, 51
- Smartt S. J., 2009, *ARA&A*, **47**, 63
- Smartt S. J., 2015, , **32**, e016

- Smartt S. J., Maund J. R., Gilmore G. F., Tout C. A., Kilkenny D., Benetti S., 2003, [MNRAS](#), **343**, 735
- Smith N., 2006, arXiv e-prints, [pp astro-ph/0607457](#)
- Smith N., 2014, [ARA&A](#), **52**, 487
- Smith N., Owocki S. P., 2006, [ApJL](#), **645**, L45
- Smith N., Humphreys R. M., Davidson K., Gehrz R. D., Schuster M. T., Krautter J., 2001, [AJ](#), **121**, 1111
- Soraisam M. D., et al., 2018, [ApJ](#), **859**, 73
- Soraisam M. D., Bildsten L., Drout M. R., Prince T. A., Kupfer T., Masci F., Laher R. R., Kulkarni S. R., 2020, [ApJ](#), **893**, 11
- Stothers R., 1969, [ApJ](#), **155**, 935
- Stothers R., Chin C.-W., 1968, [ApJ](#), **152**, 225
- Stothers R., Chin C. W., 1978, [ApJ](#), **226**, 231
- Stothers R., Chin C. W., 1979, [ApJ](#), **233**, 267
- Sukhbold T., Adams S., 2020, [MNRAS](#), **492**, 2578
- Sukhbold T., Woosley S. E., Heger A., 2018, [ApJ](#), **860**, 93
- Sundqvist J. O., Björklund R., Puls J., Najarro F., 2019, [A&A](#), **632**, A126
- Sylvester R. J., Skinner C. J., Barlow M. J., 1998, [MNRAS](#), **301**, 1083
- Tempel E., Tamm A., Tenjes P., 2010, [A&A](#), **509**, A91
- Venn K. A., McCarthy J. K., Lennon D. J., Przybilla N., Kudritzki R. P., Lemke M., 2000, [ApJ](#), **541**, 610
- Verhoelst T., van der Zypen N., Hony S., Decin L., Cami J., Eriksson K., 2009, [A&A](#), **498**, 127
- Walborn N. R., Lasker B. M., Laidler V. G., Chu Y.-H., 1987, [ApJL](#), **321**, L41
- Wallerstein G., 1981, [PASP](#), **93**, 453
- Walmswell J. J., Eldridge J. J., 2012, [MNRAS](#), **419**, 2054
- Wang T., Jiang B., Ren Y., Yang M., Li J., 2021, [ApJ](#), **912**, 112

- Wenger M., et al., 2000, [A&AS](#), **143**, 9
- Williams K. A., Bolte M., Koester D., 2009, [ApJ](#), **693**, 355
- Wirth A., Smarr L. L., Bruno T. L., 1985, [ApJ](#), **290**, 140
- Wood P. R., Bessell M. S., Fox M. W., 1983, [ApJ](#), **272**, 99
- Yang M., et al., 2023, [A&A](#), **676**, A84
- Yaron O., et al., 2017, [Nature Physics](#), **13**, 510
- Zurita A., Bresolin F., 2012, [MNRAS](#), **427**, 1463
- de Jager C., Nieuwenhuijzen H., van der Hucht K. A., 1988, [A&AS](#), **72**, 259
- van Loon J. T., 2000, [A&A](#), **354**, 125
- van Loon J. T., Groenewegen M. A. T., de Koter A., Trams N. R., Waters L. B. F. M., Zijlstra A. A., Whitelock P. A., Loup C., 1999, [A&A](#), **351**, 559
- van Loon J. T., Zijlstra A. A., Bujarrabal V., Nyman L. Å., 2001, [A&A](#), **368**, 950
- van Loon J. T., Cioni M. R. L., Zijlstra A. A., Loup C., 2005, [A&A](#), **438**, 273